SPIN DYNAMICS OF FERROMAGNETIC THIN FILMS, HETEROSTRUCTURES AND NANOSTRUCTURES

Thesis submitted for the degree of

Doctor of Philosophy (Science)

in

Physics (Experimental)

by

Sreya Pal

Department of Physics

University of Calcutta

2024

Dedicated to my grandparents,

Late Mr. Manikeswar Pal & Late Smt. Satkari Pal

Abstract

The rapid advancement of charge-based electronics, guided by Moore's law, has reached critical challenges due to transistor miniaturization limits and heat-related inefficiencies. Spintronics, which exploits the electron's spin in addition to its charge, has emerged as a transformative alternative for more efficient information processing. This doctoral thesis, titled *"Spin Dynamics of Ferromagnetic Thin Films, Heterostructures, and Nanostructures,"* investigates both fundamental and technological aspects of spin dynamics and spin-wave behavior in various magnetic systems, offering new insights into the fields of spintronics and magnonics.

The thesis covers experimental investigations using wave vector techniques such as Brillouin light scattering (BLS) and time-domain techniques like time-resolved magneto-optical Kerr effect (TR-MOKE) magnetometry. The research explores key phenomena such as the interfacial Dzyaloshinskii-Moriya interaction (iDMI) in transition-metal dichalcogenides (TMD)/ferromagnet (FM) heterostructures, revealing enhanced iDMI values due to spin-orbit coupling and spin-valley coupling at TMD/FM interfaces. These findings have significant implications for the stabilization of chiral spin textures, such as skyrmions.

A major highlight is the observation of acousto-plasmo-spin wave (APSW) modes in 2D artificial magnonic crystals. These modes arise from non-linear tripartite coupling between plasmons, phonons, and magnons, leading to a remarkable parametric amplification of spin waves. The APSW modes, seen in both plasmonic thin films and nanodot arrays, exhibit a frequency comb pattern driven by hybridized phonon-plasmon interactions.

Additionally, the thesis presents groundbreaking work on spin texture-driven reconfigurable magnonics, demonstrating a novel mechanism for controlling spin-wave dispersion in diatomic nanodot arrays by manipulating spin texture coupling. The study also examines magnetization dynamics in diatomic antidot arrays, showing that variations in collective dynamics are strongly dependent on the orientation of the in-plane bias field and internal field distribution.

Overall, this thesis provides significant contributions to the understanding of spin-wave dynamics, offering new avenues for developing energy-efficient, non-volatile magnetic storage, and reconfigurable spintronic devices. It lays the groundwork for future research in quantum technologies and advanced magnetic systems.

সারমর্ম

ইলেকট্রনিক্সের চার্জ-ভিত্তিক প্রযুক্তির দ্রুত অগ্রগতি, যা মুরের আইনের দ্বারা পরিচালিত, বর্তমানে ট্রানজিস্টরকে আরও ক্ষুদ্র করার সীমা এবং তাপ-সম্পর্কিত অকার্যকারিতার মতো গুরুত্বপূর্ণ চ্যালেঞ্জের সম্মুখীন হয়েছে। ইলেকট্রনের চার্জের পাশাপাশি এর স্পিনের সদ্ব্যবহারকারী স্পিনট্রনিক্স একটি কার্যকর বিকল্প হিসেবে আবির্ভূত হয়েছে, যা তথ্য প্রক্রিয়াকরণের জন্য অধিক কার্যকর সমাধান প্রদান করে।

এই ডক্টরাল থিসিস, "ফেরোম্যাগনেটিক পাতলা স্তর, হেটারোস্ট্রাকচার এবং ন্যানোস্ট্রাকচারের স্পিন গতিশীলতা", বিভিন্ন চৌম্বকীয় সিস্টেমে স্পিন গতিশীলতা ও স্পিন-ওয়েভ আচরণের মৌলিক ও প্রযুক্তিগত দিকগুলিকে বিশ্লেষণ করে, যা স্পিনট্রনিক্স এবং ম্যাগনোনিক্স ক্ষেত্রে নতুন দৃষ্টিভঙ্গি প্রদান করে।

থিসিসে তরঙ্গ ভেক্টর-ভিত্তিক পদ্ধতি যেমন ব্রিলুয়িন আলো বিচ্ছুরণ (BLS) এবং সময়-ডোমেইন পদ্ধতি যেমন সময়-নির্ধারিত ম্যাগনেটো-অপটিকাল কের ইফেক্ট (TR-MOKE) ম্যাগনেটোমেট্রি ব্যবহার করে পরীক্ষামূলক গবেষণার আলোচনা করা হয়েছে। গবেষণায় ট্রানজিশন-মেটাল ডাইক্যালকোজেনাইড (TMD)/ফেরোম্যাগনেট (FM) হেটারোস্ট্রাকচারে ইন্টারফেসিয়াল ডিজিয়ালশিনস্কি-মোরিয়া ইন্টারঅ্যাকশন (iDMI)-এর মতো গুরুত্বপূর্ণ ঘটনা অনুসন্ধান করা হয়েছে, যা স্পিন-অরবিট কাপলিং এবং TMD/FM ইন্টারফেসে স্পিন-ভ্যালি কাপলিং-এর মাধ্যমে iDMI মান উল্লেখযোগ্যভাবে বৃদ্ধি করার বিষয়টি তুলে ধরে। এই ফলাফলগুলি স্কারমিয়নসের মতো কাইরাল স্পিন টেক্সচারের স্থিতিশীলতার জন্য গুরুত্বপূর্ণ।

এই গবেষণার একটি প্রধান অগ্রগতি হলো দুই-মাত্রিক কৃত্রিম ম্যাগনোনিক ক্রিস্টালে আকউস্টো-প্লাজমো-স্পিন ওয়েভ (APSW) মোডের পর্যবেক্ষণ। এই মোডগুলি প্লাজমন, ফোনন এবং ম্যাগননের অরৈখিক ত্রিপক্ষীয় সংযোগ থেকে উদ্ভূত হয়, যা স্পিন-ওয়েভের উল্লেখযোগ্য প্যারামেট্রিক অ্যাম্প্লিফিকেশন ঘটায়। APSW মোডগুলি প্লাজমনিক পাতলা স্তর এবং ন্যানোডট অ্যারে উভয় ক্ষেত্রেই দেখা যায়, এবং এই মোডগুলি হাইব্রিডাইজড ফোনন-প্লাজমন ইন্টারঅ্যাকশনের মাধ্যমে চালিত ফ্রিকোয়েন্সি কম্ব প্যাটার্ন প্রদর্শন করে।

এছাড়াও, থিসিসে স্পিন টেক্সচার-চালিত পুনর্গঠিত ম্যাগনোনিক্স নিয়ে যুগান্তকারী কাজ উপস্থাপন করা হয়েছে। এটি দ্বি-পরমাণু ন্যানোডট অ্যারেতে স্পিন টেক্সচার কাপলিং নিয়ন্ত্রণের মাধ্যমে স্পিন-ওয়েভ ডিসপারশনের জন্য একটি নতুন প্রক্রিয়া প্রদর্শন করে। গবেষণায় দ্বি-পরমাণু অ্যান্টিডট অ্যারেতে

চৌম্বকায়ন গতিশীলতার পরীক্ষা করা হয়েছে, যেখানে সম্মিলিত গতিশীলতার পরিবর্তন প্রধানত অভ্যন্তরীণ ক্ষেত্রের বিতরণ এবং ইন-প্লেন বায়াস ফিল্ডের অভিমুখের উপর নির্ভরশীল।

সামগ্রিকভাবে, এই থিসিস স্পিন-ওয়েভ গতিশীলতা বোঝার ক্ষেত্রে উল্লেখযোগ্য অবদান রাখে এবং শক্তি-সাশ্রয়ী, নন-ভোলাটাইল চৌম্বক স্টোরেজ এবং পুনর্গঠিত স্পিনট্রনিক ডিভাইসগুলির উন্নয়নের জন্য নতুন পথ উন্মুক্ত করে। এটি কোয়ান্টাম প্রযুক্তি এবং উন্নত চৌম্বকীয় সিস্টেমে ভবিষ্যৎ গবেষণার জন্য শক্ত ভিত্তি স্থাপন করে।

List of Publications:

A. Included in the Thesis:

1. S. Husain*, **S. Pal***, X. Chen, P. Kumar, A. Kumar, A. K. Mondal, N. Behera, N. K. Gupta, S. Hait, R. Gupta, R. Brucas, B. Sanyal, A. Barman, S. Chaudhary, and P. Svedlindh, *Large Dzyaloshinskii-Moriya interaction and atomic layer thickness dependence in a ferromagnet- WS_2 heterostructure*, Phys. Rev. B, 105, 064422 (2022) (*contributed equally)
2. **S. Pal**, P.K. Pal, R. Fabiha, S. Bandyopadhyay and A. Barman, *Acousto-Plasmo-Magnonics: Coupling Spin Waves with Hybridized Phonon-Plasmon Waves in a 2D Artificial Magnonic Crystal Deposited on a Plasmonic Material*, Adv. Funct. Mater., 33: 2304127 (2023).
3. **S. Pal**, P.K. Pal, R. Fabiha, S. Bandyopadhyay and A. Barman, *Tripartite Phonon-Magnon-Plasmon Coupling, Parametric Amplification, and Formation of a Phonon-Magnon-Plasmon Polariton in a Two-Dimensional Periodic Array of Magnetostrictive/Plasmonic Bilayered Nanodots*, arXiv:2312.09343, (Accepted for publication in 'Journal of Applied Physics').
4. **S. Pal**, MN Hasan, H. Bangar[3], M. Pereiro, N. Salehi, P. Thunström, P. K. Muduli, D. Karmakar and A. Barman, *Scaling of Interfacial Dzyaloshinskii-Moriya Interaction and Heisenberg Exchange with Spin-Orbit Coupling in Transition-Metal Dichalcogenide/Permalloy Heterostructures* (Manuscript submitted)
5. **S.Pal** et al., *Spin Texture Driven Reconfigurable Magnonics in Diatomic Nanodot Arrays* (Manuscript to be submitted)
6. **S.Pal** et al., *Investigation of magnetization dynamics in diatomic antidot arrays* (Manuscript to be submitted)

B. Not Included in the Thesis:

1. R. Saha, S. Chakraborty, K. Sinha, P. Pyne, **S. Pal**, A. Barman, S. Chakrabarty, R. K. Mitra, *Ion-Pairing Propensity in Guanidinium Salts Dictates Their Protein (De)stabilization Behavior*, The Journal of Physical Chemistry Letters 15 (41), 10341-10348 (2024).

2. C. Kumar*, R. Sharma*, **S. Pal**, G. Datt, T. Sarkar, M. V. Kamalakar and A. Barman, *Observation of Additive Interfacial Dzyaloshinskii–Moriya Interaction in Monolayer-MoS_2 /Co/Pt Asymmetric Trilayer System* (Accepted for publication in 'Physical Review Applied')(*contributed equally)
3. **S.Pal** et al., *Direct Measurement of Interfacial Dzyaloshinskii–Moriya Interaction at ReS_2/CoFeB Interface: Correlation with Spin-Orbit Coupling Strength* (Manuscript under preparation).
4. **S.Pal** et al., Investigation of Magnetization Dynamics in Electrodeposited Co and Co/Cu Nanowires (Manuscript under preparation).

Acknowledgements

As I reach the culmination of my doctoral journey spanning over five years, I find myself reflecting on the myriad of support and encouragement that have accompanied me along this path. I am profoundly grateful to all who have contributed to my growth, both personally and academically.

First and foremost, I want to express my deepest gratitude to Prof. Anjan Barman, for his constant supervision, scholastic guidance, insightful suggestion, unwavering support, continuous inspiration, affectionate treatment, systematic planning of research programme during the entire course of investigation and for giving me the opportunity to work in his world-class laboratory as part of his esteemed research group. His guidance in developing my scientific temperament, from planning and conducting challenging experiments to rigorously analyzing data and discussing findings, has been invaluable. His tireless efforts in maintaining state-of-the-art research facilities and his incredible multitasking ability have profoundly inspired me.

I pay my sincere gratitude to our collaborator Prof. Supriyo Bandhyopadhyay (Virginia, USA) whose knowledge, efficiency, intuition and wisdom mesmerized me while working with him in our lab and preparing manuscripts. I also express my gratitude to Dr. Sajid Husain from Lawrence Berkeley National Lab, UC Berkeley and Prof. P.K. Muduli from IIT Delhi for their contributions and for providing intriguing samples that enriched our research. Engaging in theoretical collaborations with Dr. Debjani Karmakar from BARC was a rewarding experience that broadened my understanding. My appreciation extends to Dr. Jaivardhan Sinha and Prof. Venkata Kamalakar for their valuable insights during the optimization of the electrochemical deposition setup, as well as to Prof. Rajib Kumar Mitra and Prof. Manoranjan Kumar of SNB, who graciously evaluated my progress as members of my thesis committee.

A huge thanks to all our current and past group members. Working alongside Dr. Avinash Kumar Chaurasiya, Dr. Sourav Sahoo, Dr. Amrit Kumar Mondal, Dr. Surya Narayan Panda, and Dr. Koustuv Dutta has been a journey filled with invaluable support and stimulating discussions. I am grateful to Dr. Sucheta Mondal and Dr. Anulekha De for their fruitful suggestions during my research. My heartfelt thanks to Dr. Sumaiya Parveen and Dr. Rubina Ghosh, who have always been my steadfast well-wishers. I am grateful to Dr. Arpan Bhattacharya, Dr. Ajit Sahoo, and Chandan for helping in different ways and by giving ideas in optimizing nanowire

deposition in electrochemical deposition setup. I learned so much from Amrit da, Arundhati di, Sudip da and Pratap da—from rigorous alignment processes and experiments to analyzing data. I am thankful to my labmates cum batchmates, Soma, Payal, and Suranjana, for our engaging discussions that marked the early days of my doctoral journey. Many thanks to Pratap da for his approachable nature with any problem—academic or otherwise—ensuring smooth experiments, engaging in scientific discussions, and keeping up the adventurous, positive vibes during conference days.

I would like to cherish the friendly and homely atmosphere created by our lab members during COVID 19 pandemic times. I relished the time spent with my labmates—Suchetana, Chandan, Bikram, Sayan, Sayanti, Soumava and Susmita—for maintaining a friendly lab environment.

I feel fortunate to have had the opportunity to mentor several students during my PhD, including Smridhi, Mahima, Najrul, Keshav, and Sourav, whose enthusiasm and insights have enriched my experience. Additionally, I like to acknowledge project students during my PhD tenure including Shubham, Gaurav Patel, Rajdwip, Gaurav Kanu, Prapti, Prerak, Adwitiya, Dimple, Meghashree, Roshani, Swapnil and Shuvoshree for maintaining a friendly atmosphere in the lab.

Beyond my lab, I express sincere thanks to Dipika di, Somashree di, Sumana di, Anupam da, Swarnali di, Didhiti di and Debayan da, from whom I learned so much and they helped me in several ways. I cherish the colorful memories shared with my batchmates—Riju, Kanchan, Ardhendu, Ria, Gesessew, Amrita, Krishnendu, and Ramakrishna. Many thanks to Riju for training me on the Arduino kit, which helped me win the 'Magnetic Sensor Challenge' award and also for the 'Magnetism as Art' competition at MMM' 2023 conference, introducing me to some of the clean room facilities, sharing valuable scientific discussions, and supporting me through life's ups and downs.

I would like to acknowledge the staff of the technical cell at SNBNCBS—Urmi di, Debarghya da, Sourav da, Amit da, Joy da, and Subhabrata da—for their assistance with the characterization tools. I am grateful to all staff at SNBNCBS, including those in academic, accounts, library, purchase, engineering, and electrical sections, as well as the doctors of medical unit, for their unwavering support. I am grateful to Ms. Nibedita Konar [DR (Academic)] for always giving a solution towards any academic problem and Mr. Suman Saha [DR (Finance)] for his guidance in navigating the complexities of the CSIR fellowship and grants.

As a fitness enthusiast, I will always cherish my experiences in sports activities like badminton, table tennis, and Kyokushin karate. Serving as the sports coordinator and SNB mess committee member for a year each, as well as participating in the SNB reunion committee, taught me invaluable life lessons through these responsibilities.

Finally, I am indebted to my school teachers—Bordi (Dr. Krishna Mukhopadhyay), Debapriya di, Firdous di and later on Pabitra Sir, Haraprasad Sir and many more—who inspired me to become an avid learner and, moreover, a good human being. I owe much to Dr. Abani Mohan Rudra, whose mentorship cultivated my interest in research, and to my professors at the University of Burdwan— Prof. Tanmoy Banerjee, Prof. Udit Chatterjee, and Prof. Pabitra K. Chakrabarti.

I am grateful to my college and university friends—Shantanu, Shubhadeep, Abhik, and Arif for their unwavering support and friendship throughout the years.

I express my profound love, respect, and gratitude to my grandparents, whose teachings and philosophies continue to guide me, and I cherish the unwavering support of my family—Maa and Baba (Mrs. Archana Pal and Dr. Nityananda Pal), who have been my pillars of strength. Didi (Dr. Riya Pal) and Dada (Dr. Ayan Pal) have always provided me with joy and motivation. My heartfelt thanks also go to my maternal uncle, Mr. Somnath Pal, for his warm hospitality during my first solo trip to the U.S. for the MMM'2023 conference. Also, I express my heartfelt thanks to Dr. Somnath Sarkar, whose medical expertise and care have helped me recover from illness numerous times.

Lastly, I feel immensely blessed to have been a PhD fellow at the S. N. Bose National Centre for Basic Sciences (SNBNCBS), Kolkata, enriched by advanced instrumental facilities and a vibrant research environment. I am deeply thankful to Calcutta University for my PhD registration and to the Council of Scientific and Industrial Research (CSIR), Government of India, for their financial support throughout my research tenure and for granting me the opportunity to attend international conferences.

List of Abbreviations

1D	: One dimensional
2D	: Two dimensional
3D	: Three dimensional
ADL	: Antidot lattice
AFM	: Atomic force microscopy
AOM	: Acousto-optic modulator
BBO	: Barium beta-borate
BLS	: Brillouin light scattering
BMC	: Bicomponent magnonic crystal
BS	: Beam splitter
BV	: Backward volume
BZ	: Brillouin zone
CMOS	: Complementary metal-oxide semiconductor
CPW	: Coplaner waveguide
CVT	: Chemical vapor transport
CW	: Continuous wave
DE	: Damon-Eschback
DOS	: Density of states
DW	: Domain wall
ECD	: Electrochemical deposition
EDX	: Energy dispersive X-ray spectroscopy
EY	: Elliot-Yafet
FFT	: Fast Fourier transform
FMR	: Ferromagnetic resonance
fs	: Femtosecond
FWHM	: Full width half maxima
FWVMS	: Forward volume magnetostatic wave
GHz	: Giga Hertz
GMR	: Giant magnetoresistance

GVD : Group velocity dispersion
HDD : Hard disk drive
HWP : Half wave plate
LBO : Lithium tri-borate iv
LLG : Landau-Lifsitz-Gilbert
M3TM : Microscopic three temperature model
MBG : Magnonic band gap
MC : Magnonic crystal
MFM : Magnetic force microscopy
MHz : Mega Hertz
MO : Microscope objective
MOKE : Magneto optical Kerr effect
MRAM : Magnetic random-access memory
MSSW : Magnetostatic surface wave
MTJ : Magnetic tunnel junction
mW : Milli Watt
NA : Numerical aperture
ns : Nano second
OBD : Optical bridge detector
OOMMF : Object oriented micromagnetic framework
pA : Pico Ampere
PBS : Polarized beam splitter
PEM : Photo elastic modulator
PMA : Perpendicular magnetic anisotropy
ps : Picosecond
PSSW : Perpendicular standing spin-wave
PWM : Plane wave method
RF : Radio frequency
RT : Room temperature
SEM : Scanning electron microscopy
SHG : Second harmonic generator

SOI	: Spin orbit interaction
STT	: Spin transfer torque
SW	: Spin-wave
TFPI	: Tandem Fabry Perot interferometer
THz	: Tera Hertz
TMR	: Tunnel magnetoresistance
TR-MOKE	: Time resolved magneto optical Kerr effect
VNA	: Vector network analyzer
VPUF	: Verdi pumped ultrafast laser
VSM	: Vibrating sample magnetometer
XRD	: X-ray diffraction

List of Figures

Contents

Chapter 1

1. Introduction

Magnetism, a fundamental interaction governing the behavior of certain materials, has fascinated humankind for millennia. From ancient lodestone compasses to modern particle accelerators, magnetism has driven technological advancements. Beyond simple attraction, the intrinsic property of electron spin has emerged as a transformative paradigm for information storage and processing, ushering in the realm of spintronics[1]. Spintronics utilizes the electron's spin, alongside its charge, to encode and manipulate information, offering compelling advantages over conventional electronics[2, 3]. Spin currents can be generated and manipulated with lower energy consumption, paving the way for energy-efficient devices. Additionally, spin information is more resilient to external noise, enabling robust and reliable information processing. The propagation of the exchange coupled spins form the spin waves (SWs) with magnons as their quanta[4]. However, as we approach the physical limits of miniaturization, this exponential growth nears its end, presenting an opportunity for magnonics to emerge as a promising alternative for future information technologies. The pursuit of miniaturized and energy-efficient devices has inspired scientists to delve into innovative approaches for structuring and patterning materials at the nanoscale. [2, 5]. This exploration, which took root in the previous century, has evolved from studying natural nanocomposites to engineering sophisticated artificial nanostructures. The driving ambition has consistently been to curtail energy consumption while amplifying storage capacity, operational speed, and device durability. With Moore's Law nearing its fundamental limits, the need to transcend charge-based semiconductor technologies has become urgent. Magnetic nanostructures emerge as a compelling alternative, offering remarkable potential to address the challenges of contemporary technological demands. The efficiency of these devices is deeply intertwined with the intricate physical mechanisms within nanomagnetic systems, prompting extensive research into their underlying dynamics. Cutting-edge fabrication and characterization methods have shed light on fascinating dynamical behaviors manifesting across diverse spatial and temporal scales.

Magnonics explores the potential of harnessing SWs for information processing and storage, marking a departure from traditional charge-based electronics[6]. Moreover, magnons can be

manipulated at significantly higher frequencies than electrons, enabling the creation of faster devices capable of processing information at unprecedented speeds. This attribute not only enhances the performance of magnonic devices but also contributes to their scalability and integration into diverse technological applications[7]. Magnonics addresses the formidable challenges encountered by conventional electronics as miniaturization reaches its limits. Magnon-based devices hold the promise of being faster, more energy-efficient, and potentially more scalable than charge-based counterparts. This transformative potential extends across various technological sectors, including data storage, logic devices, biomedicine, and magnon-based neuromorphic computing architectures. The versatility and efficiency of magnonic devices position them as key players in shaping the future of information technology, offering novel solutions to the challenges faced by the rapidly evolving digital landscape.

1.1. Overview of Magnonics

"Magnonics" has emerged as a fascinating offshoot of "nanomagnetism," dedicated to exploring SWs and their manipulation within magnetic materials featuring periodic variations in magnetic properties. These periodic variations create modulated potentials for propagating magnons, giving rise to engineered magnetic architectures known as magnonic crystals (MCs). Drawing parallels with photonic and phononic crystals [8, 9] , magnonic crystals represent their magnetic counterparts. The term itself was independently introduced in 2001 by Puszkarski et al. [10] and Nikitov et al.[11] This periodic modulation, in alignment with Bragg's law and Bloch's theorem, results in the emergence of a spin-wave band structure, showcasing the interplay between periodicity and wave dynamics in these intricate systems.

Numerous studies on the quasistatic and dynamic properties of one-dimensional (1D) and two-dimensional (2D) MCs—including nanodots, antidots, nanorings, bi-component, and binary nanostructures—have revealed their fundamental SW properties and potential applications in SW logic, resonators, filters, phase shifters, splitters, directional couplers, and other magnonic devices[3, 9, 12-14]. Significant efforts have focused on reprogrammable MCs, where static and dynamic responses can be modified on demand[15]. Reprogrammable 1D MCs typically feature periodic nanowire arrays with complex unit cells, allowing independent switching of subunits[16]. This reprogrammability has paved the way for magnetic field-controlled reconfigurable MCs with multimodal frequency transmission characteristics[17]. Extending

these structures to the third dimension (3D) could lead to complex magnetic configurations with unprecedented properties[18]. Despite these advancements, nanomagnetism still faces significant challenges, and fully harnessing the potential of magnetic nanostructures requires further experimental and theoretical research.

1.1.1. Magnetic Material Selection for Magnonic Applications

The selection of magnetic materials is pivotal in shaping the progress of both foundational and practical aspects of magnonics. Key attributes include a low Gilbert damping parameter (α) to support prolonged spin-wave (SW) lifetimes, a high saturation magnetization (M_S) to facilitate elevated SW frequencies and velocities, and robust Curie temperatures (T_C) to ensure thermal stability. Equally vital is the ease of fabricating and patterning magnetic films, enabling efficient realization of desired structures. Among the critical factors for magnonic applications is the ratio of the mean free path to the wavelength, a parameter that significantly influences performance. Enhancing this ratio continues to pose a major challenge, driving innovation and research in the field.[19].

The ferrimagnet monocrystalline $Y_3Fe_5O_{12}$ (YIG: Yttrium Iron Garnet), grown by high-temperature liquid-phase epitaxy (LPE) on gadolinium gallium garnet (GGG) substrates[20, 21], is distinct in this field for its remarkably low damping properties, facilitating efficient SW propagation over extended distances with minimal energy dissipation. However, the complex patterning demands associated with MCs using YIG present challenges, prompting researchers to explore alternative materials and structures[3]. Among these alternatives, metallic ferromagnets like $Ni_{80}Fe_{20}$ (permalloy), cobalt iron boron (CoFeB) and cobalt (Co), and have emerged as promising candidates for micro- and nanostructured magnonic devices. Permalloy (Py hereafter)[22-26], a polycrystalline alloy composed of 80% nickel and 20% iron, is a widely used material in magnonics. As a soft magnetic material, it exhibits low coercivity and anisotropies. One significant advantage of Py is its relatively low SW damping considering it is a metal, coupled with its ease of deposition and nanostructuring. Considerable attention is currently also focused on CoFeB[27-30] and half-metallic Heusler compounds[31, 32] due to their lower Gilbert damping parameters and higher M_S values, making them highly suitable for magnonic applications. For instance, Heusler compounds have demonstrated SW mean free

paths up to 16.7 μm[33]. Furthermore, cobalt (Co)[34] is extensively utilized in magnonics due to its high spin polarization, elevated T_C, and substantial magnetic anisotropy.

1.1.2. Dynamics of 2D arrays of magnetic nanostructures

Patterning magnetic thin films in 2D at the nanoscale, enabled by advancements in fabrication technologies, results in connected and disconnected structures. These can be classified as nanodots[35, 36], interconnected dots[14, 37], antidots[36, 38], bi-component[39, 40] and binary nanostructures. This subsection will briefly discuss their high-frequency dynamics.

1.1.2.1. Magnetic nanodots

Theoretical investigations into the high-frequency dynamics of ferromagnetic nanodot arrays first gained momentum in the late 1990s. These pioneering studies delved into the influence of inter-dot dipolar interactions, exploring how variations in array geometry and the orientation of the applied magnetic field shaped their behavior.[41, 42].

Arrays of nanodots exhibit quasi-uniform magnetization configurations due to inevitable edge defects, leading to various states such as "S," "C," flower, and leaf states[43]. Initial experimental studies of ferromagnetic resonance (FMR) spectra showed multimodal oscillations, dependent on external magnetic field orientation and interparticle interactions[44]. Subsequent experiments, including Brillouin light scattering (BLS) studies[45], revealed different SW branches and modes in nanodots. Studies on time-resolved magnetization dynamics in bilayer nanodot arrays demonstrated non-monotonic precession frequency variation with dot size, highlighting a crossover from collective modes (CM) to edge modes (EM)[46]. Further research uncovered dynamical configurational anisotropy[47], SW modes in non-ellipsoidal elements, and significant findings on Gilbert damping unaffected by nanopatterning despite size-dependent linewidth variations. The focus then shifted to collective magnonic modes in strongly coupled nanoelement arrays, revealing anisotropic dynamic coupling and transitions from uniform collective modes[48] to isolated nanodot dynamics with varying areal density[49]. Lattice symmetry[50] effects were explored, showing variations in collective SW modes with different lattice geometries. The impact of dot shape[51] was also significant, with different shapes exhibiting varied SW spectra due to internal field profiles and mode quantization.

Extensive research has revealed phenomena such as mode softening, crossover, splitting, and the merging of spin-wave frequency branches in response to variations in the bias field. [52].

Recent advancements have uncovered remarkable effects, including strong magnon-magnon coupling and nonlinear ferromagnetic resonance (FMR) behavior. Notably, patterned magnetic systems exhibit power-dependent nonlinear FMR shifts under microwave excitation, shedding light on the intricate dynamics within these structures.[53, 54].

1.1.2.2. Magnetic antidots

Magnetic antidot lattices (ADLs), crafted from ferromagnetic thin films with periodic perforations, have emerged as promising contenders for developing reconfigurable MCs. Unlike isolated nanomagnet arrays, ADLs offer higher SW propagation velocity and longer propagation distance due to the absence of isolated magnetic entities and the presence of exchange-coupled films[14]. ADLs also avoid the superparamagnetic limit, providing advantages in SW dynamics. Extensive experimental and numerical studies have explored SW localization and quantization, as well as anisotropic propagation in ADLs, revealing phenomena like Bragg diffraction[55], high-symmetry modes[56], and complete magnonic band gaps (MBGs). Key advancements included damping, and velocities of SWs with respect to the orientation of the bias field[57]. Additionally, the ability to tune the transmission coefficient of SWs through the orientation of an external magnetic field suggested a tunable metamaterial response[58]. Control of SW modes in ADLs progressed through variations in lattice constant, shape of antidot, base material, lattice symmetry, bias field strength and orientation[34, 59]. Defects in MCs[60], whether inadvertent or tailored, play crucial roles in tuning magnonic bands and creating defect states. Numerical studies show that hexagonal antidot arrays are robust against random defects, while line defects can elevate the fundamental mode frequency and generate new extended modes. Detailed studies of defects in ADLs have demonstrated mode softening, amplification of extended modes, and new SW modes at low fields due to non-synchronous magnetization rotation. Unconventional structures, such as magnonic quasicrystals (MQCs)[34], binary ADLs, and defective lattices[61], offer enhanced tunability of SW spectra and anisotropy. New measurement techniques, such as all-electrical measurement exploiting the inverse spin Hall effect (iSHE)[62], have further advanced this field. ADLs hold great promise for applications such as highly adaptable magnetic arrays and customizable magnonic filters, seamlessly integrated into magnonic acoustic wave (MAW)[63] devices.

1.1.3. Nanoscale ferromagnetic spin texture

Magnetic spin textures are nonuniform, stable, and flexible spin configurations that exhibit remarkable tunability and scalability[64]. The interactions between various spin textures—such as vortices, skyrmions, magnetic bubbles, merons, hopfions, domain walls, monopole defects in artificial spin ice (ASI), and different quasi-uniform states (e.g., S state, leaf state, flower state, C state, onion state)— are crucial for reconfiguring SW dynamics[65]. Quasi-uniform magnetization configurations arise primarily due to the unavoidable edge effects inherent to the elements, even when subjected to a strong magnetic field. As the quantity of information continues to grow, data processing and storage face significant challenges. Spin texture-driven magnonics offer an efficient solution by enabling the creation of on-demand MCs. Additionally, these spin textures facilitate low-power operation due to their low SW impedance, making them ideal for low-power applications such as mobile devices.

1.2. Hybrid magnonics

Hybrid dynamical systems have recently emerged as a focal point of research due to their transformative applications in quantum information, communication technologies, and advanced sensing[66]. These systems represent a novel framework for integrating platforms and devices capable of performing diverse tasks, including the storage, processing, and transmission of coherent states. Notably, hybrid systems can be analyzed, implemented, and measured within the classical regime, where their dynamics are governed by well-defined formulas and exhibit phase coherence[67]. This classical approach provides a powerful foundation for studying the fundamental physics of strong coupling between various excitations, as well as for the coherent manipulation and engineering of hybrid systems[68]. These insights gained from the classical regime serve as a stepping stone to the quantum domain, enabling seamless integration with quantum modules such as qubits. Magnons, as a key component in hybrid systems, present several advantages over conventional charge-based electronics[1]. They can propagate efficiently across long distances with minimal energy dissipation due to their weak interaction with the lattice and offer potential for manipulation at higher frequencies. However, challenges remain, particularly in the direct manipulation of individual magnons and their sustained confinement. These challenges drive ongoing research into novel hybrid systems that leverage the strengths of magnons while addressing their limitations[69-71].

A defining characteristic of hybrid dynamic systems is their ability to preserve coherence while transferring information between modules[66]. Coherence, which ensures the retention of phase in excitations during this process, is constrained by the decoherence rate (κ), measurable through the frequency linewidth. In contrast, the efficiency of transduction hinges on the coupling strength (g) in the frequency domain. To maintain coherence during transduction, g must be greater than the κ. The principle governing this coupling strength is elegantly described by Dicke's size-scaling law [72, 73], denoted as $g \propto \sqrt{N}$, where N represents the total number of spins within the system.

For two coupled systems, as shown in Figure 1.1.(a), with decoherence rates κ_p and κ_m (κ_p and κ_m: dissipation rate of microwave cavity mode and magnon mode respectively, suffixes are same for g), the cooperativity of the system is defined as $C = \frac{g^2}{\kappa_m \kappa_p}$ [74].

The coupling regime of a system [72] depends on the interplay between the coupling strength and the dissipation rates, as illustrated in Figure 1.1(b). When magnon decay dominates ($\kappa_p < g < \kappa_m$), the system enters the Purcell regime, where the decay of the microwave cavity photon is accelerated by its interaction with the lossy magnon. Alternatively, in the regime where $\kappa_m < g < \kappa_p$, the system displays magnetically induced transparency (MIT), akin to electromagnetically induced transparency (EIT), leading to reduced absorption through the interplay of the magnon and cavity photon. As the coupling strength surpasses both $g > \kappa_p, \kappa_m$, and C > 1, the system transitions to the strong coupling regime This regime, essential for coherent information processing, showcases phenomena such as Rabi oscillations between photons and magnons. In contrast, the weak coupling regime where $g < \kappa_p, \kappa_m$, and C < 1, interactions between the photon and magnon are less pronounced, posing challenges for coherent information transfer.[72].

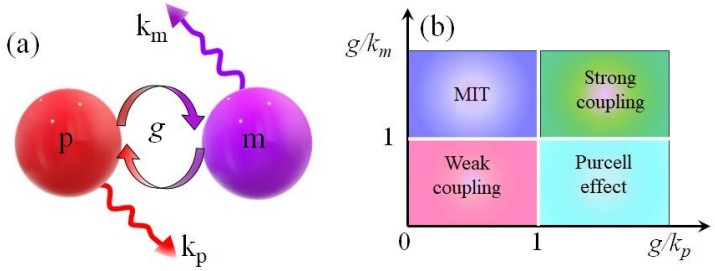

Figure 1.1: (a) A schematic representation showcasing the dynamic interaction between magnons (m) and photons (p) within the system. Symbols g, k_m, k_p denote the coupling strength, magnon dissipation rate, and the dissipation rate of the microwave cavity mode, respectively. (b) Various coupling regimes are delineated, determined by the relative magnitudes of these rates within the photon and magnon subsystems.

Hybrid magnonics, an evolving field at the intersection of magnonics and diverse physical platforms, offers a pioneering strategy to overcome hurdles and unlock magnons' full potential for quantum information processing. This approach involves integrating magnons with other quantum systems, fostering synergistic interactions that enhance the functionalities of both components. Captivating avenue in hybrid magnonics is expedited by integrating experimental advancements and simulations with theoretical insights, incorporating computational methods like quantum simulations and machine learning[75, 76]. These methods enhance the ability to predict and design interactions among quasi-particles such as magnon-phonon[77], magnon-plasmon[78], magnon-fluxon[79], magnon-polaron-phonon[80], magnon-exciton[81], magnon-superconducting transmon couplings[82] and so on. Each hybrid configuration offers unique advantages and paves the way for novel functionalities in quantum technologies.

In a nutshell, hybrid magnonics represents a paradigm shift in magnonics, unlocking unparalleled capabilities for quantum information processing. By strategically integrating magnons with other quantum systems, researchers are paving the way for robust quantum devices and revolutionizing information processing. Potential applications include scalable quantum computers, secure quantum communication, and ultra-sensitive magnetic sensors, heralding a new era of technological advancements.

1.3. Plasmonics

In metals, plasma oscillation represents the collective longitudinal motion of the conduction electron gas, with its quantized manifestation known as a plasmon. Plasmons can be excited by electron or photon interactions with a thin metallic film, where the electron's charge couples to the electrostatic field fluctuations of the plasma. This coupling induces discrete energy losses in the reflected or transmitted electron, corresponding to integral multiples of the plasmon energy. Surface plasmons (SPs) are electromagnetic waves coupled to the collective oscillations of surface free charges at the interface between a dielectric and a metal, as schematically shown in figure 1.2.(a) and (b). These modes exhibit strong localization at interfaces and can manifest across diverse metallic structures, including single surfaces, thin films, and nanoparticles. Surface plasmons (SPs) are broadly categorized into two types: localized surface plasmons (LSPs), which arise in structures smaller than the wavelength of the incident radiation, and surface plasmon polaritons (SPPs), which propagate along planar interfaces.

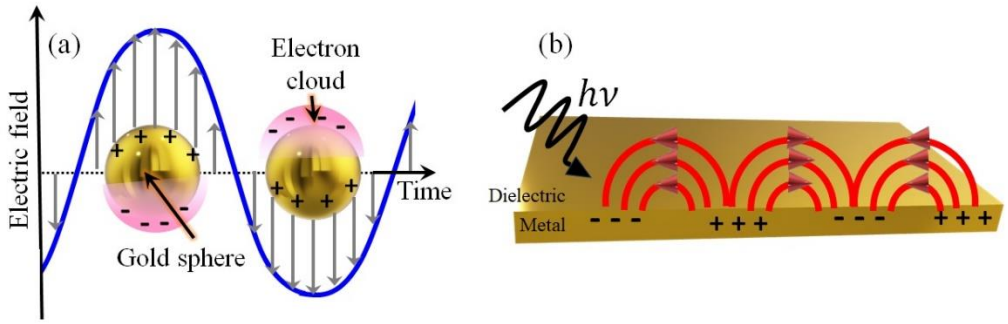

Figure 1.2: Schematics of (a) localized surface plasmons on the surface of a metal nanoparticles, (b) propagating surface plasmon polaritons along the metal-dielectric interface; and bottom.

SPs possess the remarkable ability to confine electromagnetic fields within nanoscopic volumes, surpassing the diffraction limit, which makes them exceptionally suited for applications in nanophotonic devices. This confinement leads to significant local field enhancements, increasing the interaction of light with nearby molecules or emitters. Recent advances have enabled active plasmonic configurations controlled by temperature, voltage, or photons. A promising alternative for active plasmonics is using magnetic fields, which can modify optical properties based on magnitude and direction. Given that magnetism is inherently ultrafast, switching speeds at femtosecond levels could be achievable.

1.3.1. Background: Polarization

Polarization defines how a material interacts with electromagnetic waves, encompassing both electrical and magnetic aspects. However, at frequencies exceeding several hundred THz[84], the magnetic polarization of naturally occurring materials becomes negligible. As described by the generalized Drude theory, the permittivity of a material can be represented as:

$$\varepsilon(\omega)' + i\varepsilon(\omega)'' = \varepsilon(\omega) = \varepsilon_{int} - \frac{\omega_p^2}{\omega(\omega + i\Gamma)} \quad \ldots\ldots(1.1.a)$$

$$\omega_p^2 = \frac{ne^2}{\varepsilon_0 m^*} \quad \ldots\ldots(1.1.b)$$

In Eq. (1a), $\Gamma = \frac{1}{\tau}$, where τ is the mean relaxation time of conduction electrons, and ε_{int} accounts for interband transitions, equating to unity for a perfectly free-electron gas. The plasma frequency ω_p is defined in Eq. (1.1.b), where n is the conduction electron density, and m^* is the effective optical mass of conduction electrons. Electrical polarization is described by the material's complex electrical permittivity, $\varepsilon(\omega)$. The real part, $\varepsilon(\omega)'$), represents the strength

of polarization induced by an external electric field, while the imaginary part, $\varepsilon(\omega)''$), represents the losses encountered during polarization. Hence, low-loss materials exhibit small values of $\varepsilon(\omega)''$.[84]

1.3.2. Searching for Plasmonic Materials

Plasmonic phenomena stem from free charge oscillations in response to electromagnetic fields, necessitating metals for their negative $\varepsilon(\omega)'$), achieved when the plasma frequency exceeds the application frequency. Metals, particularly silver and gold, are preferred due to their high plasma frequencies and electrical conductivity. Silver has the smallest Γ, while gold, stable and effective in the NIR range, suffers high interband losses below 500 nm. Copper also has significant interband losses in the visible spectrum. However, metals experience high losses, especially in the visible and UV ranges, due to interband transitions. Thus, alternative low-loss plasmonic materials are needed to enhance device robustness and efficiency[84].

Unlike silver, gold, or copper, aluminum (Al) stands out for its unique material properties that support robust plasmon resonances across a broad spectrum, extending from the visible region into the ultraviolet. Furthermore, Al excels in efficiently generating hot carriers over the widest frequency range while minimizing resistive losses. For Al, the bulk plasmon frequency (ω_p≈15eV) is comparatively higher than Au and Ag[86]. Within the framework of the basic Drude model for metals and a straightforward metal/air interface, surface plasmons are anticipated to exist within the frequency range $0 \leq \omega \leq \omega_s$, where $\omega_s = \frac{\omega_p}{\sqrt{2}}$ is the quasi-static surface plasmon frequency. Al emerges as a highly promising candidate for a versatile plasmonic hot carrier generator. It efficiently produces hot carriers over an extensive frequency range, generating high-energy electrons and holes with equal likelihood, all while exhibiting superior transport properties[87].

1.3.3. Acousto-plasmo-magnonics

The influence of magnetic fields on plasmonic properties has captivated the magneto-plasmonic research community, sparking significant interest and inquiry [88, 89]. An equally intriguing, yet underexplored, counterpart is the reciprocal effect—where surface plasmons, potentially hybridized with other quanta, impact the dynamic magnetic properties of materials, such as the behavior of SWs. This emerging field pushes beyond the established bipartite magnetoelastic

coupling, where interactions between phonons and magnons in magnetostrictive nanomagnets give rise to magnon-polarons[77, 90-93]. The next frontier is tripartite coupling, wherein phonons, magnons, and plasmons converge to unveil novel physics and applications. Traditional understanding has suggested that coupling phonons, magnons, and plasmons is challenging due to a phase mismatch, as plasma frequencies vastly exceed those of SWs. However, SPs, which exhibit lower frequencies than bulk plasmons, can hybridize with acoustic phonons to form hybrid phonon-plasmon modes. These hybrid modes possess frequencies closer to those of SWs in ferromagnetic media, facilitating coupling. This new phenomenon has been observed in coupling between SWs and hybridized phonon-plasmon waves in a 2D periodic array of magnetostrictive nanomagnets on a silicon substrate with an aluminum thin film acting as a SP source[78], and in bilayered (Co/Al) nanodot arrays[94]. Hybridized phonon-plasmon waves naturally form in this composite material when exposed to ultrashort laser pulses and they non-linearly couple with SWs to produce a new breed of waves – acousto-plasmo-spin waves. This phenomenon, that can be called acousto-plasmo-magnonics resulting from tripartite coupling of magnons, phonons and plasmons. This phenomenon has been observed in systems such as two-dimensional periodic arrays of magnetostrictive nanomagnets on silicon substrates, where an aluminum thin film acts as an SP source [78, 94]. This discovery opens doors to the design of innovative active metamaterials with customized and amplified responses. Such materials could enable efficient magneto-mechanical-plasmonic frequency mixing across the GHz–THz range, offering unique opportunities to explore non-linear coupling, parametric amplification, and frequency comb physics.

1.4. Thin films for information technology and surface effects

The magnetic characteristics intrinsic to a material—such as magnetization, Curie temperature, anisotropy, and magnetostriction—often display remarkable differences between thin films and their bulk counterparts. These disparities emerge predominantly from the distinct microenvironments experienced by surface and interface atoms, as well as the strain imposed by the underlying substrate. In a perfectly relaxed thin film, the lattice parameters deviate from those in bulk, with the separation of surface planes in 3*d* metal films being slightly greater[95]. Surface atoms, missing some neighbors, exhibit enhanced vibrational amplitude and weakened exchange interactions, leading to narrower bands, increased local density of states, and

enhanced local magnetic moments. These effects are typically confined to the first one or two monolayers (MLs). Moreover, substrates have the potential to modify the electronic configuration and magnetic moments of the interfacial atomic layers, leading to notable changes in their properties. The structure and lattice parameters of solids in thin film form can be extensively manipulated through careful selection of substrates and preparation conditions.

Advancements in high-quality thin film heterostructure growth and nanostructure fabrication have unveiled new physics in recent years. The discovery of giant magnetoresistance (GMR) and tunnelling magnetoresistance (TMR)[96-98] revolutionized the magnetic recording industry, enabling high-density magnetic storage and controlled fast magnetization switching. Subsequently, longitudinal recording media[99] emerged, treating grains of granular films as individual domains with in-plane magnetization. However, these media faced thermal instability and limited storage capacity due to the superparamagnetic effect and increased cross-talk between magnetic bits. Solutions involved magnetic alloys (CoPt[100], CoCrPt[101]) and multilayers (Co/Pt, Co/Pd, Fe/Pt, Co/Ni) with high perpendicular magnetic anisotropy (PMA)[99, 102, 103], achieving higher areal densities and improved thermal and magnetic stability at room temperature. Research continues to focus on tailoring PMA through defect adatoms, FM layer thickness adjustments, and doping with highly electronegative elements like nitrogen. Despite improved thermal stability, PMA systems still require high magnetic fields for magnetization switching. Heat-assisted magnetic recording (HAMR) addresses this by locally tuning magnetic anisotropy using heat from focused laser sources. Consequently, the search for thin film heterostructures with tunable magnetic anisotropy, RKKY-mediated interlayer interactions, chiral spin textures, and topologically protected skyrmions due to interfacial Dzyaloshinskii–Moriya interaction (iDMI)[104, 105] has intensified.

1.4.1. Systems with Structural Inversion Asymmetry

Thin film heterostructures of ferromagnets (FMs) with heavy metals (HMs) exhibiting large spin-orbit coupling (SOC) give rise to fascinating phenomena[106] such as PMA[107], the spin Hall effect (SHE)[108], spin pumping[109], the Rashba-Edelstein effect[110] etc. Magnetic materials lacking inversion symmetry can support the Dzyaloshinskii-Moriya interaction (DMI), a form of indirect exchange interaction first proposed by Levy and Fert [111], which arises in the presence of pronounced SOC. This interaction causes adjacent spins to tilt relative to each other, resulting in spatially modulated spin orientations. When the DMI vector becomes sufficiently

strong, the interplay between the 'winding' influence of DMI and the 'aligning' tendency of exchange interactions can produce non-collinear ground states. Such chiral spin configurations were initially observed in non-centrosymmetric single crystals. The discovery of SOC-driven phenomena and the effects of inversion-symmetry breaking at surfaces and interfaces has unveiled a vast landscape of possibilities, where the incorporation of topological properties could revolutionize spintronics technology.

2D-Material/FM Interface

2D materials like graphene and transition metal dichalcogenides (TMDs) exhibit unique spintronic properties due to their crystalline structure and large SOC[112]. Graphene, with its high electron mobility and tunable carrier concentration, is well-studied for spin transport, SOC enhancement, and defect-induced magnetism[113, 114]. Several key differences between TMDs and graphene are notable. First, monolayer TMDs inherently lack inversion symmetry [115-118], a property that gives rise to fascinating phenomena such as the valley Hall effect. Second, this inversion symmetry breaking results in valley-dependent optical selection rules for interband transitions at the K points. Third, TMDs exhibit strong SOC due to the *d*-orbitals of the heavy metal atoms. ML TMDs, such as MoS_2, WS_2, $MoSe_2$, and WSe_2, are notable for their robust SOC originating from the *d* orbitals of heavy metals like Mo and W. These MX_2 structures feature strong in-plane bonds and weak van der Waals forces between layers, enabling stable monolayers and few-layer structures without lattice matching[119]. The lack of inversion symmetry in ML TMDs leads to spin-valley coupling[120] and valley-dependent electronic band splitting, facilitating efficient spin-charge interconversion, unconventional spin-orbit torque, and field-free magnetization switching.

When interfaced with FMs, TMDs exhibit the DMI, which may stabilize chiral spin textures such as skyrmions, torons[121], merons[122], hopfions[123] and magnetic cocoons[124]. The magnetic proximity effects from FM substrates can induce significant valley exciton splitting in TMDs, crucial for manipulating spin and valley degrees of freedom in spintronic devices. Advancements in the fabrication of high-quality TMD/FM heterostructures have enabled the exploration of these phenomena at the atomic scale, paving the way for next-generation magnetic memory devices and spintronic technologies. The study of variation of TMD thicknesses and their interfacial properties with ferromagnets continues to provide valuable

insights into the fundamental physics and potential applications of these materials in advanced spintronic architectures.

1.4.2. Spin-valley coupling

In 2D TMDs, the spin and valley indices of charge carriers are intrinsically coupled. The term "valley" denotes energetically degenerate energy bands characterized by distinct local maxima in the valence bands (VBs) or minima in the conduction bands (CBs)[125]. In ML TMDs, these CB and VB edges are localized at the K and K′ points within the hexagonal Brillouin zone, forming a binary index for low-energy carriers. Due to the significant separation of valleys in momentum space, the valley index demonstrates resilience against scattering induced by smooth deformations and long-wavelength phonons.

While the spin of electrons, associated with their magnetic moments, underpins the field of spintronics, TMDs introduce an additional binary quantum degree of freedom: the valley pseudospin. This pseudospin, linked to the inequivalent yet degenerate valleys in momentum space, lays the foundation for valleytronics[126], a field that seeks to exploit the valley index of carriers for information storage and processing. An intriguing feature of TMDs is the non-trivial geometry of their band structure, which produces equal and opposite Berry curvatures—an effective magnetic field in momentum space. Coupled with strong spin-orbit interactions and pronounced light-matter coupling, this property makes TMDs ideal candidates for exploring spin-valley physics. Distinguishing the ±K valleys require measurable physical quantities sensitive to the valley index. For instance, spin-up and spin-down states, being time-reversed images of one another, exhibit opposing magnetic moments. These magnetic moments, as pseudovectors with odd parity under time reversal, facilitate spin coupling with magnetic fields, enabling the detection of spin polarization as magnetization. Consequently, physical quantities with odd parity under time reversal are effective in discerning valley pseudospin states, paving the way for advanced manipulation and application of the valley degree of freedom.

1.5. Objective of the Thesis

The objective of this thesis is to explore both fundamental and technological aspects of spin dynamics and SW dynamics in magnetic thin film heterostructures and patterned magnetic nanostructures. This exploration is conducted in two domains: the wave vector domain using

conventional BLS spectroscopy and the time domain using time-resolved magneto-optical Kerr effect (TR-MOKE) magnetometry. The studied systems are categorized as follows:

[1] *Spin-configuration driven reconfigurable magnonics:* This investigation examines SW dispersion in diatomic dot arrays made of permalloy, both experimentally and theoretically, in two quasi-spin configuration coupling regions: leaf state - leaf state coupling (at 1 kOe) and leaf state – 'S' state coupling (at 300 Oe). The reconfigurability of the magnonic band structure and band gap is demonstrated by manipulating spin texture through bias-field adjustments.

[2] *Magnetization Dynamics in Diatomic Antidot Arrays:* This study links variations in collective magnetization dynamics to the orientation of the in-plane bias magnetic field and internal magnetic field distribution changes between diatomic antidots in arrays made of permalloy.

[3] *Coupling of spin waves with hybridized phonon-plasmon waves in a 2D artificial magnonic crystal deposited on a plasmonic thin film:* This study reports the observation of acousto-plasmo-spin wave modes resulting from tripartite coupling between plasmons, phonons, and magnons in a 2D artificial magnonic crystal fabricated on a plasmonic aluminium thin film. These modes form a SW frequency comb due to the non-linear coupling phenomenon between hybridized phonon-plasmon modes and spin wave modes, also leading to significant parametric amplification.

[4] *Tripartite phonon-magnon-plasmon coupling, parametric amplification, and formation of a phonon-magnon-plasmon polariton in a 2D periodic array of magnetostrictive/plasmonic bilayered nanodots:* This work reports tripartite coupling among phonons, plasmons, and magnons in periodic arrays of bilayered nanodots; generating a high-frequency magnetic field-independent acousto-plasmo SW mode; parametric amplification of SW modes by hybrid phonon-plasmon modes, and strong coupling between two SW modes mediated by the hybrid phonon-plasmon wave, leading to the formation of the magnon-plasmon-phonon polariton.

[5] *Large interfacial Dzyaloshinskii-Moriya interaction and its atomic layer thickness dependence in a WS_2/Co_3FeB heterostructure:* This work demonstrates the use of a noncontact spin dynamics approach to investigate spin-valley splitting effects in WS_2, with potential applicability to other TMDs. Notably, spin-valley splitting is absent at the conduction band

minima in monolayer WS_2, despite significant splitting at the K (K') symmetry points at the valence band maxima, differing from the behavior observed in higher-order odd-numbered layers in interfacial Dzyaloshinskii-Moriya interaction (iDMI) constant.

[6] *Anatomy of interfacial Dzyaloshinskii-Moriya interaction and Heisenberg exchange with the scaling of spin-orbit coupling (SOC) strength at the interface of transition-metal dichalcogenides (TMDs) and permalloy:* This work independently determines the iDMI constant and the symmetric exchange constant, 'A', in monolayer TMD/Py heterostructures. It confirms that the linear proportionality between symmetric and antisymmetric exchange applies to 2D systems at the ferromagnetic/TMD interface, correlating with the SOC strength at the TMD surface.

References

[1] A. Barman et al., *Journal of Physics: Condensed Matter* **2021**, 33, 413001.
[2] A. Hirohata, K. Yamada, Y. Nakatani, I.-L. Prejbeanu, B. Diény, P. Pirro, B. Hillebrands, *Journal of Magnetism and Magnetic Materials* **2020**, 509, 166711.
[3] A. V. Chumak, V. I. Vasyuchka, A. A. Serga, B. Hillebrands, *Nature Physics* **2015**, 11, 453.
[4] J. Van Kranendonk, J. H. Van Vleck, *Reviews of Modern Physics* **1959**, 31, 839.
[5] B. Dieny, I. L. Prejbeanu, K. Garello, P. Gambardella, P. Freitas, R. Lehndorff, W. Raberg, U. Ebels, S. O. Demokritov, J. Akerman, A. Deac, P. Pirro, C. Adelmann, A. Anane, A. V. Chumak, A. Hirohata, S. Mangin, S. O. Valenzuela, M. C. Onbaşlı, M. d'Aquino, G. Prenat, G. Finocchio, L. Lopez-Diaz, R. Chantrell, O. Chubykalo-Fesenko, P. Bortolotti, *Nature Electronics* **2020**, 3, 446.
[6] Q. Wang, A. V. Chumak, P. Pirro, *Nature Communications* **2021**, 12, 2636.
[7] M. Zahedinejad, A. A. Awad, S. Muralidhar, R. Khymyn, H. Fulara, H. Mazraati, M. Dvornik, J. Åkerman, *Nature Nanotechnology* **2020**, 15, 47.
[8] M. Krawczyk, D. Grundler, *Journal of Physics: Condensed Matter* **2014**, 26, 123202.
[9] B. Lenk, H. Ulrichs, F. Garbs, M. Münzenberg, *Physics Reports* **2011**, 507, 107.
[10] H. Puszkarski, M. Krawczyk, *SSP 94, 125–134,* **2023**.
[11] Y. V. Gulyaev, A. A. Nikitov, *Doklady Physics* **2001**, 46, 687.
[12] H. Yu, G. Duerr, R. Huber, M. Bahr, T. Schwarze, F. Brandl, D. Grundler, *Nature Communications* **2013**, 4, 2702.
[13] S. D. Bader, *Reviews of Modern Physics* **2006**, 78, 1.
[14] A. Barman, S. Mondal, S. Sahoo, A. De, *Journal of Applied Physics* **2020**, 128, 170901.
[15] A. V. Chumak, T. Neumann, A. A. Serga, B. Hillebrands, M. P. Kostylev, *Journal of Physics D: Applied Physics* **2009**, 42, 205005.
[16] J. Topp, S. Mendach, D. Heitmann, M. Kostylev, D. Grundler, *Physical Review B* **2011**, 84, 214413.
[17] G. Gubbiotti, X. Zhou, Z. Haghshenasfard, M. G. Cottam, A. O. Adeyeye, *Physical Review B* **2018**, 97, 134428.
[18] A. Fernández-Pacheco, R. Streubel, O. Fruchart, R. Hertel, P. Fischer, R. P. Cowburn, *Nature Communications* **2017**, 8, 15756.

[19] A. V. Chumak, A. A. Serga, B. Hillebrands, *Journal of Physics D: Applied Physics* **2017**, 50, 244001.
[20] H. L. Glass, M. T. Elliot, *Journal of Crystal Growth* **1976**, 34, 285.
[21] V. Cherepanov, I. Kolokolov, V. L'Vov, *Physics Reports* **1993**, 229, 81.
[22] S. Tomita, *Journal of the Physical Society of Japan* **1961**, 16, 393.
[23] S. S. Kalarickal, P. Krivosik, M. Wu, C. E. Patton, M. L. Schneider, P. Kabos, T. J. Silva, J. P. Nibarger, *Journal of Applied Physics* **2006**, 99, 093909.
[24] V. E. Demidov, M. P. Kostylev, K. Rott, P. Krzysteczko, G. Reiss, S. O. Demokritov, *Applied Physics Letters* **2009**, 95, 112509.
[25] T. Schwarze, R. Huber, G. Duerr, D. Grundler, *Physical Review B* **2012**, 85, 134448.
[26] K. Vogt, F. Y. Fradin, J. E. Pearson, T. Sebastian, S. D. Bader, B. Hillebrands, A. Hoffmann, H. Schultheiss, *Nature Communications* **2014**, 5, 3727.
[27] A. Brunsch, *Journal of Applied Physics* **1979**, 50, 7603.
[28] X. Liu, W. Zhang, M. J. Carter, G. Xiao, *Journal of Applied Physics* **2011**, 110, 033910.
[29] S. Nayak, S. Mohanty, B. Bhusan Singh, S. Bedanta, *Journal of Physics: Condensed Matter* **2022**, 34, 385801.
[30] A. Conca, J. Greser, T. Sebastian, S. Klingler, B. Obry, B. Leven, B. Hillebrands, *Journal of Applied Physics* **2013**, 113, 213909.
[31] T. Graf, C. Felser, S. S. P. Parkin, in *Handbook of Spintronics*, (Eds: Y. Xu, D. D. Awschalom, J. Nitta), Springer Netherlands, Dordrecht 2016.
[32] P. Pirro, T. Sebastian, T. Brächer, A. A. Serga, T. Kubota, H. Naganuma, M. Oogane, Y. Ando, B. Hillebrands, *Physical Review Letters* **2014**, 113, 227601.
[33] T. Sebastian, Y. Ohdaira, T. Kubota, P. Pirro, T. Brächer, K. Vogt, A. A. Serga, H. Naganuma, M. Oogane, Y. Ando, B. Hillebrands, *Applied Physics Letters* **2012**, 100, 112402.
[34] R. Mandal, S. Saha, D. Kumar, S. Barman, S. Pal, K. Das, A. K. Raychaudhuri, Y. Fukuma, Y. Otani, A. Barman, *ACS Nano* **2012**, 6, 3397.
[35] B. Rana, D. Kumar, S. Barman, S. Pal, Y. Fukuma, Y. Otani, A. Barman, *ACS Nano* **2011**, 5, 9559.
[36] B. Rana, D. Kumar, S. Barman, S. Pal, R. Mandal, Y. Fukuma, Y. Otani, S. Sugimoto, A. Barman, *Journal of Applied Physics* **2012**, 111, 07D503.
[37] S. Sahoo, S. N. Panda, S. Barman, Y. Otani, A. Barman, *Journal of Magnetism and Magnetic Materials* **2021**, 522, 167550.
[38] K. Dutta, A. De, S. Mondal, S. Barman, Y. Otani, A. Barman, *Journal of Alloys and Compounds* **2021**, 884, 161105.
[39] S. Choudhury, S. Saha, R. Mandal, S. Barman, Y. Otani, A. Barman, *ACS Applied Materials & Interfaces* **2016**, 8, 18339.
[40] C. Kumar, P. K. Pal, A. Barman, *Physical Review B* **2024**, 109, 075407.
[41] C. Xu, P. M. Hui, L. F. Zhang, Y. Q. Ma, J. H. Zhou, Z. Y. Li, *The European Physical Journal B - Condensed Matter and Complex Systems* **2005**, 46, 475.
[42] R. L. Stamps, R. E. Camley, *Physical Review B* **1999**, 60, 12264.
[43] G. Gubbiotti, L. Albini, G. Carlotti, M. De Crescenzi, E. Di Fabrizio, A. Gerardino, O. Donzelli, F. Nizzoli, H. Koo, R. D. Gomez, *Journal of Applied Physics* **2000**, 87, 5633.
[44] S. Jung, B. Watkins, L. DeLong, J. B. Ketterson, V. Chandrasekhar, *Physical Review B* **2002**, 66, 132401.
[45] G. Gubbiotti, G. Carlotti, T. Okuno, T. Shinjo, F. Nizzoli, R. Zivieri, *Physical Review B* **2003**, 68, 184409.
[46] V. V. Kruglyak, A. Barman, R. J. Hicken, J. R. Childress, J. A. Katine, *Journal of Applied Physics* **2005**, 97, 10A706.
[47] V. V. Kruglyak, P. S. Keatley, R. J. Hicken, J. R. Childress, J. A. Katine, *Physical Review B* **2007**, 75, 024407.

[48] V. V. Kruglyak, P. S. Keatley, A. Neudert, R. J. Hicken, J. R. Childress, J. A. Katine, *Physical Review Letters* **2010**, 104, 027201.
[49] B. Rana, S. Pal, S. Barman, Y. Fukuma, Y. Otani, A. Barman, *Applied Physics Express* **2011**, 4, 113003.
[50] S. Saha, R. Mandal, S. Barman, D. Kumar, B. Rana, Y. Fukuma, S. Sugimoto, Y. Otani, A. Barman, *Advanced Functional Materials* **2013**, 23, 2378.
[51] B. K. Mahato, B. Rana, R. Mandal, D. Kumar, S. Barman, Y. Fukuma, Y. Otani, A. Barman, *Applied Physics Letters* **2013**, 102, 192402.
[52] K. Adhikari, S. Barman, R. Mandal, Y. Otani, A. Barman, *Physical Review Applied* **2018**, 10, 044010.
[53] K. Adhikari, S. Sahoo, A. K. Mondal, Y. Otani, A. Barman, *Physical Review B* **2020**, 101, 054406.
[54] P. Kumar Pal, A. Barman, *Journal of Magnetism and Magnetic Materials* **2023**, 588, 171431.
[55] R. Zivieri, S. Tacchi, F. Montoncello, L. Giovannini, F. Nizzoli, M. Madami, G. Gubbiotti, G. Carlotti, S. Neusser, G. Duerr, D. Grundler, *Physical Review B* **2012**, 85, 012403.
[56] R. Bali, M. Kostylev, D. Tripathy, A. O. Adeyeye, S. Samarin, *Physical Review B* **2012**, 85, 104414.
[57] S. Neusser, G. Duerr, H. G. Bauer, S. Tacchi, M. Madami, G. Woltersdorf, G. Gubbiotti, C. H. Back, D. Grundler, *Physical Review Letters* **2010**, 105, 067208.
[58] S. Neusser, H. G. Bauer, G. Duerr, R. Huber, S. Mamica, G. Woltersdorf, M. Krawczyk, C. H. Back, D. Grundler, *Physical Review B* **2011**, 84, 184411.
[59] R. Mandal, P. Laha, K. Das, S. Saha, S. Barman, A. K. Raychaudhuri, A. Barman, *Applied Physics Letters* **2013**, 103, 262410.
[60] D. Kumar, O. Dmytriiev, S. Ponraj, A. Barman, *Journal of Physics D: Applied Physics* **2012**, 45, 015001.
[61] S. Choudhury, S. Barman, Y. Otani, A. Barman, *Journal of Magnetism and Magnetic Materials* **2019**, 489, 165408.
[62] M. B. Jungfleisch, W. Zhang, J. Ding, W. Jiang, J. Sklenar, J. E. Pearson, J. B. Ketterson, A. Hoffmann, *Applied Physics Letters* **2016**, 108, 052403.
[63] J. W. Kłos, D. Kumar, M. Krawczyk, A. Barman, *Physical Review B* **2014**, 89, 014406.
[64] H. Yu, J. Xiao, H. Schultheiss, *Physics Reports* **2021**, 905, 1.
[65] D. Petti, S. Tacchi, E. Albisetti, *Journal of Physics D: Applied Physics* **2022**, 55, 293003.
[66] Y. Li, W. Zhang, V. Tyberkevych, W.-K. Kwok, A. Hoffmann, V. Novosad, *Journal of Applied Physics* **2020**, 128, 130902.
[67] C. L. Degen, F. Reinhard, P. Cappellaro, *Reviews of Modern Physics* **2017**, 89, 035002.
[68] P. K. Pal, A.K.Mondal, A.Barman, *J. Phys.: Condens. Matter (in press)* **2024**.
[69] H. J. Kimble, *Nature* **2008**, 453, 1023.
[70] Y. Tabuchi, S. Ishino, A. Noguchi, T. Ishikawa, R. Yamazaki, K. Usami, Y. Nakamura.
[71] H. Y. Yuan, Y. Cao, A. Kamra, R. A. Duine, P. Yan, *Physics Reports* **2022**, 965, 1.
[72] X. Zhang, C.-L. Zou, L. Jiang, H. X. Tang, *Physical Review Letters* **2014**, 113, 156401.
[73] J. Chen, C. Liu, T. Liu, Y. Xiao, K. Xia, G. E. W. Bauer, M. Wu, H. Yu, *Physical Review Letters* **2018**, 120, 217202.
[74] C. Dai, K. Xie, Z. Pan, F. Ma, *Journal of Applied Physics* **2020**, 127, 203902.
[75] Y. Makhlin, G. Schön, A. Shnirman, *Reviews of Modern Physics* **2001**, 73, 357.
[76] J. M. Martinis, S. Nam, J. Aumentado, C. Urbina, *Physical Review Letters* **2002**, 89, 117901.
[77] C. Berk, M. Jaris, W. Yang, S. Dhuey, S. Cabrini, H. Schmidt, *Nature Communications* **2019**, 10, 2652.
[78] S. Pal, P. K. Pal, R. Fabiha, S. Bandyopadhyay, A. Barman, *Advanced Functional Materials* **2023**, 33, 2304127.
[79] B. Niedzielski, C. L. Jia, J. Berakdar, *Physical Review Applied* **2023**, 19, 024073.
[80] S. Majumder, J. L. Drobitch, S. Bandyopadhyay, A. Barman, *NPG Asia Materials* **2023**, 15, 51.

[81] S. Freeman, J. J. Hopfield, *Physical Review Letters* **1968**, 21, 910.
[82] Z.-y. Jin, J. Jing, *Physical Review A* **2023**, 108, 053702.
[83] N. Maccaferri, A. Berger, S. Bonetti, V. Bonanni, M. Kataja, Q. H. Qin, S. van Dijken, Z. Pirzadeh, A. Dmitriev, J. Nogués, J. Åkerman, P. Vavassori, *Physical Review Letters* **2013**, 111.
[84] P. R. West, S. Ishii, G. V. Naik, N. K. Emani, V. M. Shalaev, A. Boltasseva, *Laser & Photonics Reviews* **2010**, 4, 795.
[85] N. W. A. a. N. D. Mermin, *Solid State Physics, 1. ed.*

(Harcourt College Publisher, Philadelphia) **1976**.
[86] M. W. Knight, N. S. King, L. Liu, H. O. Everitt, P. Nordlander, N. J. Halas, *ACS Nano* **2014**, 8, 834.
[87] M. L. Brongersma, N. J. Halas, P. Nordlander, *Nat Nanotechnol* **2015**, 10, 25.
[88] J. B. González-Díaz, A. García-Martín, J. M. García-Martín, A. Cebollada, G. Armelles, B. Sepúlveda, Y. Alaverdyan, M. Käll, *Small* **2008**, 4, 202.
[89] L. Wang, C. Clavero, Z. Huba, K. J. Carroll, E. E. Carpenter, D. Gu, R. A. Lukaszew, *Nano Letters* **2011**, 11, 1237.
[90] N. K. P. Babu, A. Trzaskowska, P. Graczyk, G. Centała, S. Mieszczak, H. Głowiński, M. Zdunek, S. Mielcarek, J. W. Kłos, *Nano Letters* **2021**, 21, 946.
[91] Y. Yahagi, B. Harteneck, S. Cabrini, H. Schmidt, *Physical Review B* **2014**, 90, 140405.
[92] R. Fabiha, J. Lundquist, S. Majumder, E. Topsakal, A. Barman, S. Bandyopadhyay, *Advanced Science* **2022**, 9, 2104644.
[93] A. De, J. L. Drobitch, S. Majumder, S. Barman, S. Bandyopadhyay, A. Barman, *Nanoscale* **2021**, 13, 10016.
[94] S. Pal, P. K. Pal, R. Fabiha, S. Bandyopadhyay, A. Barman, *arXiv:2312.09343* **2023**.
[95] J. M. D. Coey, *Magnetism and Magnetic Materials* **2009**.
[96] M. Julliere, *Physics Letters A* **1975**, 54, 225.
[97] J. S. Moodera, L. R. Kinder, T. M. Wong, R. Meservey, *Physical Review Letters* **1995**, 74, 3273.
[98] S. S. P. Parkin, C. Kaiser, A. Panchula, P. M. Rice, B. Hughes, M. Samant, S.-H. Yang, *Nature Materials* **2004**, 3, 862.
[99] M. Andreas, T. Kentaro, T. M. David, A. Manfred, S. Yoshiaki, I. Yoshihiro, S. Shouheng, E. F. Eric, *Journal of Physics D: Applied Physics* **2002**, 35, R157.
[100] D. Makarov, E. Bermúdez-Ureña, O. G. Schmidt, F. Liscio, M. Maret, C. Brombacher, S. Schulze, M. Hietschold, M. Albrecht, *Applied Physics Letters* **2008**, 93, 153112.
[101] J. M. Beaujour, C. Tran, D. Weller, B. York, B. Gurney, *IEEE Transactions on Magnetics* **2016**, 52, 1.
[102] D. Weller, A. Moser, *IEEE Transactions on Magnetics* **1999**, 35, 4423.
[103] M. Asbahi, J. Moritz, B. Dieny, C. Gourgon, C. Perret, R. J. M. van de Veerdonk, *Journal of Physics D: Applied Physics* **2010**, 43, 385003.
[104] I. Dzyaloshinsky, *Journal of Physics and Chemistry of Solids* **1958**, 4, 241.
[105] T. Moriya, *Physical Review* **1960**, 120, 91.
[106] A. Soumyanarayanan, N. Reyren, A. Fert, C. Panagopoulos, *Nature* **2016**, 539, 509.
[107] P. F. Carcia, A. D. Meinhaldt, A. Suna, *Applied Physics Letters* **1985**, 47, 178.
[108] J. E. Hirsch, *Physical Review Letters* **1999**, 83, 1834.
[109] Y. Tserkovnyak, A. Brataas, G. E. W. Bauer, *Physical Review B* **2002**, 66, 224403.
[110] M. Belmeguenai, J.-P. Adam, Y. Roussigné, S. Eimer, T. Devolder, J.-V. Kim, S. M. Cherif, A. Stashkevich, A. Thiaville, *Physical Review B* **2015**, 91, 180405.
[111] A. Fert, P. M. Levy, *Physical Review Letters* **1980**, 44, 1538.
[112] Z. Y. Zhu, Y. C. Cheng, U. Schwingenschlögl, *Physical Review B* **2011**, 84, 153402.
[113] A. K. Chaurasiya, A. Kumar, R. Gupta, S. Chaudhary, P. K. Muduli, A. Barman, *Physical Review B* **2019**, 99, 035402.

[114] A. K. Mondal, S. Majumder, S. Sahoo, S. N. Panda, S. Sinha, A. Barman, *ACS Applied Nano Materials* **2022**, 5, 5056.
[115] H. Yuan, M. S. Bahramy, K. Morimoto, S. Wu, K. Nomura, B.-J. Yang, H. Shimotani, R. Suzuki, M. Toh, C. Kloc, X. Xu, R. Arita, N. Nagaosa, Y. Iwasa, *Nature Physics* **2013**, 9, 563.
[116] A. Manchon, H. C. Koo, J. Nitta, S. M. Frolov, R. A. Duine, *Nature Materials* **2015**, 14, 871.
[117] H. Zeng, J. Dai, W. Yao, D. Xiao, X. Cui, *Nature Nanotechnology* **2012**, 7, 490.
[118] T. Cao, G. Wang, W. Han, H. Ye, C. Zhu, J. Shi, Q. Niu, P. Tan, E. Wang, B. Liu, J. Feng, *Nature Communications* **2012**, 3, 887.
[119] A. Ayari, E. Cobas, O. Ogundadegbe, M. S. Fuhrer, *Journal of Applied Physics* **2007**, 101, 014507.
[120] S. Husain, S. Pal, X. Chen, P. Kumar, A. Kumar, A. K. Mondal, N. Behera, N. K. Gupta, S. Hait, R. Gupta, R. Brucas, B. Sanyal, A. Barman, S. Chaudhary, P. Svedlindh, *Physical Review B* **2022**, 105, 064422.
[121] G. Posnjak, S. Čopar, I. Muševič, *Scientific Reports* **2016**, 6, 26361.
[122] S.-Z. Lin, A. Saxena, C. D. Batista, *Physical Review B* **2015**, 91, 224407.
[123] N. Kent, N. Reynolds, D. Raftrey, I. T. G. Campbell, S. Virasawmy, S. Dhuey, R. V. Chopdekar, A. Hierro-Rodriguez, A. Sorrentino, E. Pereiro, S. Ferrer, F. Hellman, P. Sutcliffe, P. Fischer, *Nature Communications* **2021**, 12, 1562.
[124] M. Grelier, F. Godel, A. Vecchiola, S. Collin, K. Bouzehouane, A. Fert, V. Cros, N. Reyren, *Nature Communications* **2022**, 13, 6843.
[125] A. V. Kolobov, J. Tominaga, *Two-Dimensional Transition-Metal Dichalcogenides* **2016**.
[126] W. Yao, D. Xiao, Q. Niu, *Physical Review B* **2008**, 77, 235406.

Chapter 2

2. Theoretical Background

Magnetism, an enduring fascination in science, has captivated human curiosity for millennia. The ability of magnets to attract ferrous objects from a distance, recognized as early as ancient civilizations like Sumer, Greece, China, and pre-Columbian America, has persisted through history. The study of magnetism has evolved through continuous theoretical and experimental advancements, spanning centuries of scientific inquiry. P. Peregrinus' discovery of lodestone poles in 1269 A.D. marked the formal beginning of magnetism research[1]. Initial theories centered on electron orbital angular momentum, and later, the exploration of magnetism in s-band electrons of silver atoms by Stern-Gerlach heralded a new era[2] . Modern understanding of magnetization is rooted in the behavior of unpaired electrons, their spin dynamics, and interactions with orbital angular momenta. Materials are classified into diamagnetic, paramagnetic, ferromagnetic, ferrimagnetic, and antiferromagnetic categories based on their response to magnetic fields. Notably, only ferro- and ferrimagnets exhibit spontaneous magnetization in the absence of an external magnetic field. The Heisenberg exchange interaction, elucidated through quantum mechanics, describes spontaneous magnetization arising from neighboring spin-spin interactions[3]. Weiss introduced the concept of magnetic domains in 1906, explaining their formation through the interplay of exchange and dipolar interactions, crucial in minimizing energy within ferromagnets[4]. The advent of nanomagnetism has added complexity, where geometric factors—such as shape and dimensions—significantly influence magnetization reversal dynamics alongside exchange and dipolar interactions. This thesis explores these principles within ferromagnetic thin films and nanostructures, highlighting their fundamental roles in modern magnetism research.

2.1. Different magnetic energies

2.1.1. Zeeman energy

The Zeeman energy represents the interaction between magnetization $\boldsymbol{M}$ and an external magnetic field $\boldsymbol{H_0}$. The energy is expressed as[5]:

$$E_{Zeeman} = -\mu_0 \int_V \boldsymbol{M} \cdot \boldsymbol{H_0}\, d\tau \quad \ldots\ldots \quad (2.1)$$

where V is the volume of the magnetic structure and dτ is the volume element. This equation indicates that, in the presence of a magnetic field, ***M*** tends to align with $\boldsymbol{H_0}$ to minimize the energy.

2.1.2. Magnetic dipolar interaction

The dipolar interaction between two magnetic dipoles is a fundamental aspect of any magnetic dipole, regardless of whether it is part of a ferromagnetic system. The energy associated with this interaction is given by[1]:

$$E_{dipole} = \frac{\mu_0}{4\pi r^3}\left[\mu_1 \cdot \mu_2 - \frac{3}{r^2}(\mu_1 \cdot r)(\mu_2 \cdot r)\right] \quad \ldots\ldots (2.2)$$

Here, μ_0 represents the permeability of free space, while μ_1 and μ_2 denote the magnetic moments of the interacting dipoles, and ***r*** is the vector separating them. The relationship reveals that the interaction energy diminishes proportionally to the cube of the distance between the dipoles. In ferromagnetic materials, although this long-range interaction does not directly drive magnetic ordering, it plays a pivotal role in shaping key phenomena. These include the formation of magnetic domains, the behavior of the demagnetizing field, and the propagation of spin waves in the long-wavelength regime, underlining its significance in the broader landscape of magnetism.

2.1.3. Exchange energy

The exchange interaction, rooted in quantum mechanics, is a short-range magnetic interaction energy that adheres to the Pauli exclusion principle and Coulomb interaction. Heisenberg developed the theory of exchange interaction based on the Heitler-London model for the hydrogen atom, and hence it is known as the ‘Heisenberg exchange’ or ‘isotropic exchange’ interaction. This interaction explains the magnetic ordering in ferromagnets, ferrimagnets, and antiferromagnets.

The Heisenberg exchange Hamiltonian between two neighboring spins S_i and S_{i+1} is given by[6]:

$$H_{ex} = -2 \sum_i J_{i,i+1} S_i S_{i+1} \quad \ldots\ldots (2.7)$$

where *J* is the exchange integral. *J* is positive for parallel spin configuration (ferromagnet) and negative for antiparallel spin configuration (antiferromagnet). In the continuum limit, this can be expressed as:

$$E_{ex} = A \int_0^V (\nabla m)^2 \, dV \quad \ldots\ldots (2.8)$$

where *m* is the normalized magnetization and *A* is the exchange stiffness constant, given by (for bcc lattice) with lattice constant *a*:

$$A = \frac{2JS^2}{a} \quad \ldots\ldots (2.9)$$

The direct exchange interaction involves magnetic atoms interacting with their nearest neighbors' electrons. There are also indirect exchange interactions, where itinerant electrons mediate the coupling of magnetic atoms over larger distances. Some notable indirect exchange interactions are listed below:

2.1.3.1. RKKY Exchange

The RKKY (Ruderman-Kittel-Kasuya-Yosida) interaction[7, 8] is an indirect exchange mechanism where itinerant conducting electrons mediate the coupling between magnetic moments with little or no direct overlap between neighboring electrons.

2.1.3.2. Superexchange

In superexchange[9], magnetic cations are exchange-coupled via non-magnetic anions. This interaction is common in antiferromagnetic insulators like transition metal oxides, where large oxygen anions separate the transition metal cations. The coupling occurs through hopping via the intermediate p-orbitals of oxygen.

2.1.3.3. Antisymmetric exchange

This describes a three-site exchange mechanism primarily attributed to spin-orbit coupling and broken inversion symmetry, resulting in superexchange interaction and spin canting at a slight angle[10]. In this scenario, two adjacent ferromagnetic atoms are interconnected through a three-site exchange pathway involving a non-magnetic atom.

2.1.3.3.1. Dzyaloshinskii-Moriya interaction (DMI)

This three-site exchange mechanism involves coupling between two neighboring ferromagnetic atoms via an intermediate non-magnetic atom[11-13].

The Dzyaloshinskii-Moriya interaction (DMI) is a form of anisotropic exchange interaction that energetically favors non-collinear or canted spin alignments. This unique interaction manifests only in systems where inversion symmetry is inherently broken. Originating from the influence of spin-orbit coupling (SOC), it serves as a perturbative effect on the localized spin states. When examining two adjacent spins, $\boldsymbol{S_i}$ and $\boldsymbol{S_j}$, the DMI introduces a bilinear term to the Hamiltonian, represented by the energy contribution: $H_{DMI} = -\boldsymbol{D_{ij}} \cdot \left(\boldsymbol{S_i} \times \boldsymbol{S_j}\right)$ … … (2.10)

Here, $\boldsymbol{D_{ij}} = D_{ij}\boldsymbol{n} \times \boldsymbol{e_{ij}}$ is the DMI vector, which lies in the symmetry-breaking plane and is perpendicular to the unit vector that connects sites *i* and *j*, $\boldsymbol{e_{ij}} = \frac{\boldsymbol{r_{ij}}}{|\boldsymbol{r_{ij}}|}$, as shown in Fig. 2.1 (a). In this context, $\boldsymbol{D_{ij}}$ is related to the isotropic exchange interaction characterized by the Heisenberg exchange term $J_{ij}(\boldsymbol{S_i} \cdot \boldsymbol{S_j})$ where J_{ij} is the Heisenberg exchange constant[10]. The Heisenberg exchange interaction promotes collinear alignment of spins, while the DMI encourages an orthogonal arrangement between $\boldsymbol{S_i}$ and $\boldsymbol{S_j}$, with the chirality determined by the direction of $\boldsymbol{D_{ij}}$.

DMI was first proposed in the 1950s to explain weak ferromagnetism in antiferromagnets like α-Fe_2O_3 over the following decades[11, 12], DMI's role in noncollinear and helical magnetism was studied in materials such as spin glasses, orthoferrites, manganites, and superconducting cuprates[14-17]. The development of advanced imaging techniques like spin-polarized scanning tunnelling microscopy (SPSTM) and spin-polarized low-energy electron microscopy (SPLEEM) revitalized interest in DMI in the early 21st century[18-20]. In non-centrosymmetric single crystals with FeSi structures, such as MnSi and FeGe, DMI was shown to produce skyrmion lattices and other exotic spin textures at low temperatures, which were directly visualized[21].

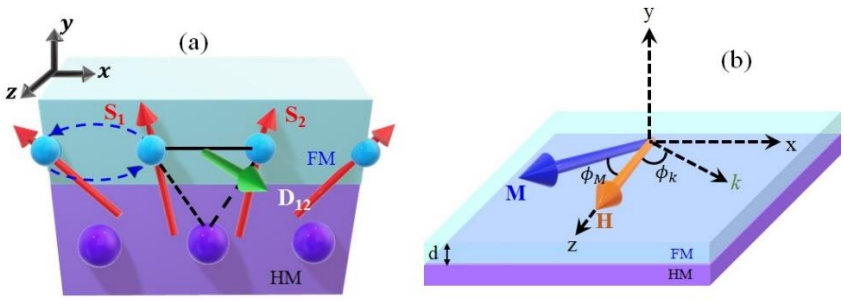

Figure 2.1: Schematic of interfacial Dzyaloshinskii-Moriya interaction at HM/FM interface

Techniques for experimentally quantifying the DMI in HM/FM systems can be broadly categorized into three distinct approaches [22]:

- *Domain-wall methods*: These methods derive *D*, by analyzing various domain-wall properties. This includes measuring domain-wall velocity and energy under the influence of an in-plane magnetic field, evaluating domain-wall spacing within stripe domain phases, or directly probing the internal structure of the domain walls.

- *Spin-wave methods*: In these techniques, *D* is determined by examining the nonreciprocity of propagating SWs in films magnetized in-plane. The asymmetry in wave propagation offers insights into the strength of the DMI.

- *Spin-Orbit Torque Methods*: This approach involves extracting DDD by observing the shift in the out-of-plane hysteresis loop when an in-plane magnetic field is applied, revealing the interplay between spin-orbit effects and DMI.

In the literature, two theoretical approaches are primarily used to describe SW spectra in thin film samples with DMI. The quantum SW theory[23], which is more suitable for high wavevector measurements in ultrathin films, is particularly relevant for techniques like spin-polarized electron energy loss spectroscopy (SPEELS), where exchange interactions dominate the SW dispersion. On the other hand, the classical theory[24] of magnetostatic SW assumes a continuum medium, making it appropriate for experiments where the detected SW wavelengths range from a few microns to a few hundred nm, as in Brillouin light scattering (BLS). In such cases, the discrete nature of spins can be ignored.

According to the classical model, DMI energy density is given by[25, 26],

$$E_{DM} = \frac{D}{M_S^2}\left(M_y \frac{\partial M_x}{\partial x} - M_x \frac{\partial M_y}{\partial x} + M_y \frac{\partial M_z}{\partial y} - M_z \frac{\partial M_y}{\partial z}\right) \quad \ldots (2.11)$$

Where D is the DMI constant and M_i is the i-th component of the magnetization. The magnetization of a linear SW can be expressed as $M(x,t) = M_S m(x,t)$. … … (2.12)

The unit vector in the direction of the magnetization can be expressed as:

$$m(x,t) = m_{xo} e^{i(\omega t - kx)} \hat{e}_x + m_{yo} e^{i(\omega t - ky)} \hat{e}_y - \hat{e}_z \quad \ldots (2.13)$$

Where m_{xo}, m_{yo} are much less than 1, $\hat{e}_x, \hat{e}_y \; and \; \hat{e}_z$ are the unit vectors along the coordinate axis. For SW travelling in the x direction, the expression of DMI field is given by[27],

$$H_{DM} = -\frac{1}{\mu_0}\frac{\delta E_{DM}}{\delta M} = \frac{2D}{\mu_0 M_S}\left(\frac{\partial m_y}{\partial x}\hat{e}_x - \frac{\partial m_x}{\partial x}\hat{e}_y\right) \quad \ldots (2.14)$$

The total effective field is:

$$H_{eff} = -H\hat{e}_z + J\nabla^2 M + H_{dip} + H_{ani} + H_{DM} \quad \ldots (2.15)$$

Where $J = \frac{2A}{\mu_0 M_S}$, L is the thickness of the magnetic film, $\xi(kL) = 1 - \frac{1-e^{|-kL|}}{|kL|}$ and the dipolar field is expressed as: : $H_{dip} = -M_S \xi(kL) m_x \hat{e}_x - M_S[1 - \xi(kL)] m_y \hat{e}_y$ … … (2.16)

The perpendicular magnetic anisotropy field, $H_{ani} = \frac{2k}{\mu_0 M_s} m_y \hat{e}_y$ where K is the anisotropy constant. Substituting the equation into the well-known LLG equation, we obtain the following SW dispersion relation: $\omega = \omega_0 + \omega_{DM}$

$$= \mu_0 \gamma \sqrt{[H + Jk^2 + \xi(kL) M_S \sin^2 \varphi_k][H - H_U + Jk^2 + M_S - \xi(kL) M_S]} - 2\frac{\gamma}{M_S} Dk \quad \ldots (2.17)$$

This is also valid for ϕ_k values other than π/2, as illustrated in Fig. 2.1(b). The general expression for ω_{DMI} is given by[24]: $\omega_{DMI} = \frac{2\gamma D}{M_s} k \sin \phi_k \cos \phi_M$ … … (2.18)

where the angles are defined in Fig. 2.1(b). The defined angular relationships reveal that, consistent with quantum theoretical predictions, the DMI introduces a linear shift in the dispersion relation proportional to k and contingent on the wave vector's sign. This shift manifests as frequency nonreciprocity driven by DMI, with its magnitude influenced by both the magnetization direction and the propagation of SWs. Importantly, this nonreciprocity vanishes at k = 0, which corresponds to the condition for ferromagnetic resonance (FMR).

Cortés-Ortuño and Landeros (2013) proposed employing BLS to extract the DMI constant, emphasizing that the most pronounced effects emerge when a sufficiently strong external field aligns the magnetization in-plane ($\phi_M = 0$) under Damon-Eshbach geometry ($\phi_k = \pi/2$).

The DMI induced frequency difference of counter propagating SWs is given by:

$$\Delta f = \frac{\omega(-k)-\omega(+k)}{2\pi} = \frac{2\gamma}{\pi M_s} Dk \quad \ldots\ldots (2.19)$$

The equation clearly illustrates that the frequency disparity exhibits a linear dependence on both the SW wave vector and the iDMI constant. Notably, this relationship remains unaffected by variations in the applied in-plane (IP) magnetic field.

2.1.4. Magnetic anisotropy

While Heisenberg exchange energy is isotropic, ferromagnetic materials typically have spins aligned along specific crystallographic axes. These axes that favor magnetization alignment are termed easy axes, whereas those that resist magnetization saturation are called hard axes. Deviating from these preferred directions imposes an additional energy penalty on the system, known as anisotropy energy[28]. The primary sources of magnetic anisotropy include SOC, symmetry axes, and long-range dipolar interactions. Below are some of the prominent types of magnetic anisotropies:

2.1.5. Magnetocrystalline anisotropy

Magnetocrystalline anisotropy originates predominantly from the interplay between spin-orbit coupling (SOC) and the symmetry axes of the crystal lattice [29]. The orientation of electronic orbits is governed by the crystallographic axes, and SOC compels the electronic spins to preferentially align along distinct crystallographic directions. The intricacy of magnetic anisotropy is inherently tied to the lattice symmetry. In cubic systems, the anisotropy energy is described in terms of the direction cosines, α_x, α_y, α_z, which represent the orientation of magnetization relative to the cube edges. For such systems, the energy density is mathematically expressed as: $E_{ani} = K_0 + K_1\left(\alpha_x^2\alpha_y^2 + \alpha_y^2\alpha_z^2 + \alpha_x^2\alpha_z^2\right) + \alpha_x^2\alpha_y^2\alpha_z^2$ … … (2.3)

For crystals with uniaxial anisotropy, the energy density is given by: $E_{an_i} = K_u\alpha_x^2$ … (2.4)

where K_u is the uniaxial anisotropy constant.

2.1.6. Magnetic dipolar (shape) anisotropy and demagnetizing energy

The size of the magnetic element leads to shape anisotropy when the element size is reduced to the μm and nm range[30]. This arises from anisotropic dipolar interactions involving unsaturated magnetic surface charges (stray and demagnetization fields) due to the lack of geometric symmetry in magnetic elements. The energy corresponding to the stray field can be expressed as:

$$E_{dem} = -\frac{\mu_0}{2}\int_V M \cdot H_{dem}\, d\tau \quad \ldots\ldots (2.5)$$

For an irregularly shaped magnetic element, E_{dem} is significantly influenced by the structure and geometry, making it a complex function of position. The magnetization direction of the element will align with the direction that minimizes $E_{dem.}$

2.1.7. Volume, surface, and perpendicular magnetic anisotropy

In thin films and multilayers with broken inversion symmetry, an additional effective anisotropy term arises, incorporating both surface anisotropy (K_S) and volume anisotropy (K_V). The effective anisotropy of a system with thickness t can be expressed as:

$$K_{eff} = K_V + \frac{2K_S}{t} \quad \ldots\ldots (2.6)$$

The second term becomes significant as the film thickness decreases due to its "twice" multiplication factor and inverse dependency on thickness. Below a critical thickness, $t_c = -\frac{2K_S}{K_V}$, the film magnetization favors perpendicular orientation, leading to perpendicular magnetic anisotropy (PMA)[31-33]. PMA emerges from the interplay of reduced spatial symmetry, localized epitaxial strain at interfaces, and the electronic band structure. This property is vital for ensuring the thermal stability of nanomagnets at ambient temperatures, rendering it highly advantageous for data storage technologies. When a FM layer is adjacent to a non-magnetic material, the interfacial hybridization modifies the energies and wavefunctions of the out-of-plane (OOP) states. Such hybridizations, which are highly sensitive to the local structural attributes of the interface, influence the SOC perturbations, thereby reshaping the anisotropy energy landscape. As a result, the strength of PMA is closely tied to the degree of hybridization, with stronger hybridization leading to enhanced anisotropy.

2.1.8. Configurational anisotropy

The interplay between exchange and dipolar interactions is particularly critical in nanostructures. In such cases, magnetic structures can be artificially configured into various non-ellipsoidal shapes. For non-ellipsoidal elements, the transition of magnetization from a uniform to a non-uniform state incurs significant energy, known as configurational anisotropy[34, 35]. This anisotropy depends on the shape and lattice symmetry of the nanoelements and can be further classified as follows[36]:

2.1.8.1. Intrinsic configurational anisotropy

This anisotropy[34] arises due to the shift from a single domain state to various magnetic spin textures, such as leaf, flower, C-, or S-states within a single magnetic element at the micro- or nanoscale when subjected to different orientations of a bias magnetic field.

2.1.8.2. Extrinsic configurational anisotropy

Regions near the edges of an element that are magnetostatically unsaturated vary with the azimuthal (in-plane) direction of the bias magnetic field (φ). Consequently, the magnetostatic interaction between elements changes significantly, affecting the distribution of the magnetic stray field (or demagnetizing field) and the configurational magnetic anisotropy[36, 37], depending on the configuration of the magnetic elements.

2.2. Importance of length scale and time scales: From nature to magnetization dynamics

The spin configurations of magnetic materials undergo significant variations when scaled down from the micro- to the nanoscale. This scaling dramatically alters the energy landscapes, leading to substantial changes in both static and dynamic properties. For instance, μm-sized soft-magnetic disks exhibit a magnetic vortex state characterized by an in-plane spin configuration and an out-of-plane core. As the size is gradually reduced to the nanoscale, the system transitions through a quasi-single-domain state to a single-domain structure[38].

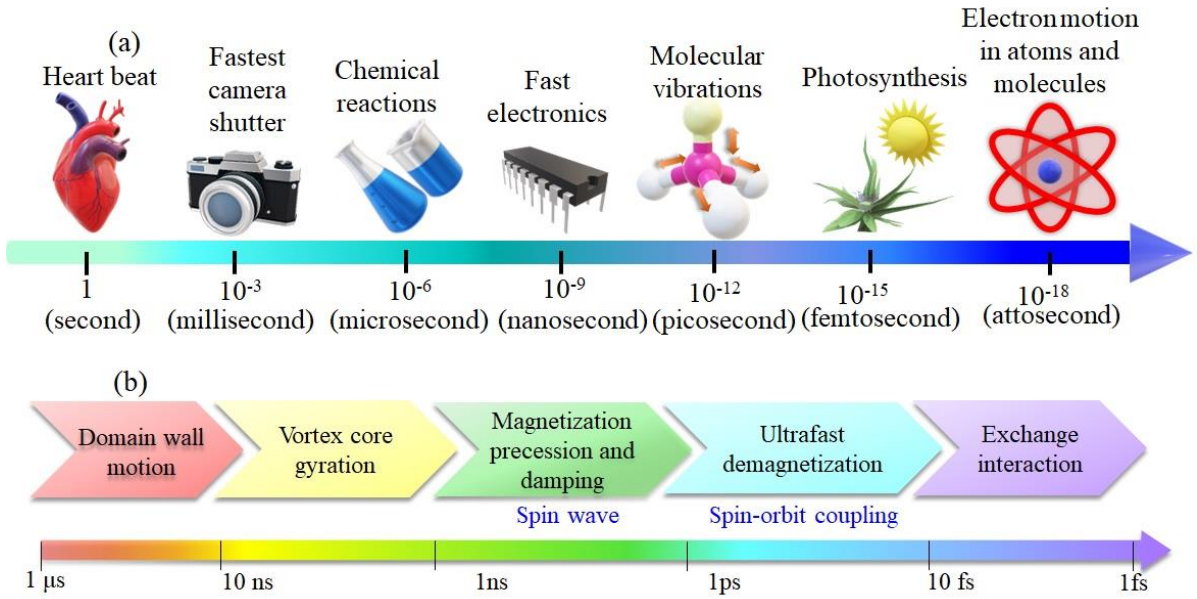

Figure 2.2: Time scales of (a) natural processes (b) various dynamical magnetic processes

Time scales in physical phenomena vary widely, reflecting the diversity of processes in nature. A heartbeat occurs on the order of 1 second, a relatively slow process in biological terms. In contrast, a camera shutter can open and close in about 1 millisecond (1 ms), capturing fleeting moments with high precision. At an even faster scale, molecular vibrations occur in the picosecond range (1 ps), revealing the rapid dynamics within molecules. These examples highlight the broad spectrum of time scales, from the perceptible rhythms of life to the ultrafast movements at the molecular level.

Femtosecond laser pulses offer an intriguing opportunity to probe magnetic systems on a timescale corresponding to the equilibrium exchange interaction, which is responsible for the existence of magnetic order. Magnetization dynamics can be classified based on characteristic timescales: the fastest process is the fundamental exchange interaction, occurring within approximately 10 fs. SOC and related phenomena also occur on the fs timescale. The timescale of precessional magnetization dynamics ranges from a few ps to several hundred ps. The magnetization damping associated with these precessional motions occurs on a sub-ns to tens of ns timescale. In ferromagnetic materials SWs propagate over a period of a few hundred ps to tens of ns before being damped. The relatively slower processes include vortex core gyration and core switching (hundreds of ps to several ns), and domain wall (DW) motion, which occurs over a range from a few ns to several μs[39]. Time scales of natural processes and magnetic dynamical processes are depicted in Fig. 2.2.

2.3. Spin waves

When a magnetic system encounters an external disturbance, the energy required to reverse an individual spin diminishes by distributing the perturbation across a long wavelength. This process gives rise to spin waves (SWs), a phenomenon first conceptualized by Bloch in 1930[40]. These waves represent low-energy excitations within magnetic materials, emerging when the direction of local magnetic order varies spatially in a smooth and continuous manner, as illustrated in Fig. 2.3(a). Notably, the energy associated with these excitations decreases progressively as the wavelength extends, reflecting the system's preference for minimizing energetic costs.The quanta of SWs, known as magnons, are quantized similarly to photons and phonons[38]. Recent developments in "magnonics," a subset of nanomagnetism, focus on generating and manipulating SWs in magnetic media with periodically modulated properties, creating structures termed magnonic crystals (MCs)[41, 42]. Analogous to photonic and phononic crystals, MCs allow modulation of magnetic interactions and SW dynamics, including band structure and bandgap, through artificial geometrical variations.

SWs are increasingly valued in scientific and industrial circles due to their unique properties: they enable information encoding in amplitude and phase, support non-Boolean logic operations, can operate at room temperature, offer tunable dispersion, integrate easily on chips, achieve high frequencies up to terahertz ranges, and exhibit nanoscale wavelengths ideal for miniaturized devices. The resurgence of interest in SWs is driven by their potential in advancing computing technologies, including hybrid quantum systems and applications[43] in 'magnon-spintronics'.

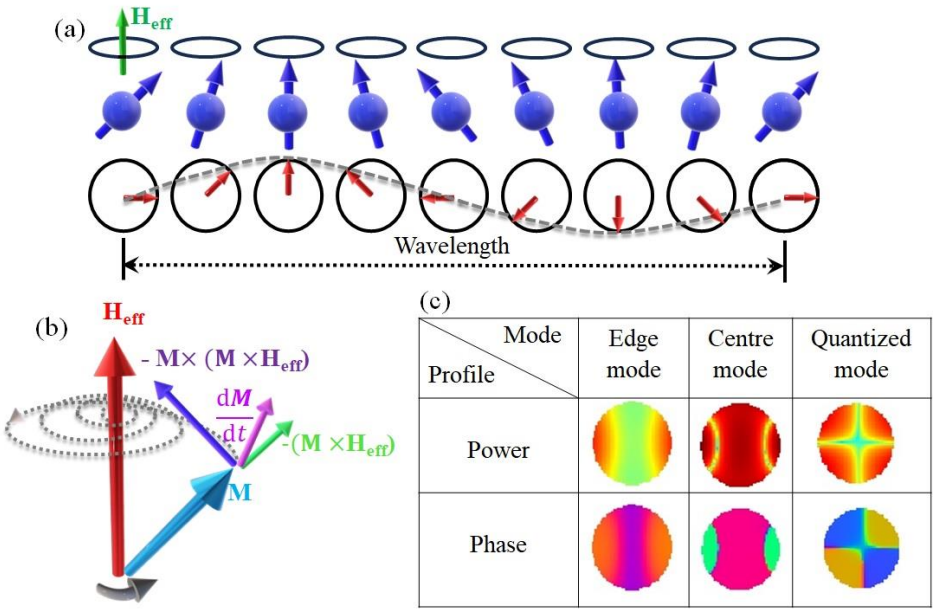

Figure 2.3: (a) Semiclassical representation of SWs in a ferromagnet (incoherent dynamics), (b) The schematic representation of magnetization precession and damping around the effective magnetic field direction.

2.3.1. Precessional magnetization dynamics

In the presence of an external magnetic field and external perturbations, magnetic moments in a material experience torque, inducing precession around an effective magnetic field. This field comprises an external field (H_0), exchange field (H_{ex}), dipolar field (H_{dip}), anisotropic field (H_{ani}), and a time-varying magnetic field $h(t)$. The precessional motion of magnetization is governed by the torque equation proposed by Lev Landau and Evgeny Lifshitz (LL) in 1935, given by:

$$\frac{d\boldsymbol{M}}{dt} = -\gamma\left(\boldsymbol{M} \times H_{eff}\right) \quad \ldots\ldots (2.20)$$

where γ is the gyromagnetic ratio, given by $\gamma = g\mu_B/\hbar$. Here, g is the Landé g factor, μ_B is the Bohr magneton, $\hbar$ is the Planck's constant.

Due to the inherent damping in any ferromagnetic (FM) system, this motion manifests as a damped spiral around the effective field direction. Landau and Lifshitz (LL) addressed this by adjusting the torque equation to incorporate both the precessional torque and a damping term, in Fig. 2.3.(b), expressed as[44]:

$$\frac{d\boldsymbol{M}}{dt} = -\gamma\left(\boldsymbol{M} \times H_{eff}\right) + \frac{\lambda}{M_S^2}\boldsymbol{M} \times \left(\boldsymbol{M} \times H_{eff}\right) \quad \ldots\ldots (2.21)$$

where λ is LL damping term with a dimension of sec^{-1}. In 1955, Gilbert[45] modified this equation by introducing a phenomenological dimensionless damping term, α (Gilbert damping constant). Therefore, the precessional motion is now described by the LLG equation, formulated as follows:

$$\frac{d\boldsymbol{M}}{dt} = -\gamma\left(\boldsymbol{M} \times H_{eff}\right) + \frac{\alpha}{M_S}\boldsymbol{M} \times \frac{d\boldsymbol{M}}{dt} \qquad \ldots\ldots (2.22)$$

The Gilbert damping parameter is related to LL parameter by the relation, $\alpha = \frac{\lambda}{\gamma M_s}$ and the effective field can be expressed as: $H_{eff}=H_0+H_{ex}+H_{dip}+H_{ani}+h(t)$ ... ... (2.23)

Uniform precession (k = 0)

The uniform precessional motion in a FM system is a phase-coherent collective movement of neighboring spins. In this scenario, all the magnetic moments precess together at the same frequency and in the same direction during time evolution. This in-phase motion (i.e., $\lambda \to \infty$) is known as the uniform precessional motion. This collective precession can be detected using an oscillating magnetic field. When the frequency of the oscillating field matches the natural precession frequency of the spins, it results in resonant energy absorption, a phenomenon known as ferromagnetic resonance (FMR). In 1948, C. Kittel derived the resonance condition near wave vector $k \approx 0$ after solving the LLG equation by considering the demagnetizing field and hence this FMR mode is also known as the Kittel mode[6]. It is expressed as:

$$f = \frac{\gamma}{2\pi}\sqrt{\left[H + H_k + \left(N_y - N_z\right)M_s\right][H + H_k + (N_x - N_z)M_s]} \qquad \ldots\ldots (2.24)$$

This solution applies to a general ellipsoid with the applied field along the z-axis, where N_i's are the demagnetizing factors. For a thin magnetic film with $N_x = N_z = 0$and $N_y = 4\pi$, the solution simplifies to:

$$f = \frac{\gamma}{2\pi}\sqrt{[H + H_k][H + H_k + 4\pi M_s]} \qquad \ldots\ldots (2.25)$$

Uniform precession (k ≠ 0)

In contrast, dipolar SWs are anisotropic and are classified based on the relative orientation between ***M*** and *k*.

Magnetostatic backward volume mode (MSBVM): Both the quantities ***M*** and *k* are coplanar and parallel to each other within the sample plane and it shows negative dispersion as the waves travel ‘‘backward’’ in phase, as per the expression[46]:

$$\omega_{BV} = 2\pi f_{BV} = \gamma \sqrt{H\left(H + 4\pi M_S \frac{1-e^{-2dk_{||}}}{kd}\right)} \qquad \ldots\ldots (2.26)$$

The dispersion relation is presented for a continuous film of thickness *d* that possesses a saturation magnetization M_S, under the influence of a magnetic field ***H***.

Magnetostatic surface SW mode (MSSW) or Damon-Eshbach (DE) mode: In this geometry, ***M*** and *k* are perpendicular to each other and coplanar. The dispersion relation is given by[47, 48]:

$$\omega_{DE} = 2\pi f_{DE} = \gamma \sqrt{H(H + 4\pi M_S) + (2\pi M_s)^2\left(1 - e^{-2dk_{||}}\right)} \qquad \ldots\ldots (2.27)$$

Magnetostatic forward volume mode (MSFVM): In this geometry, ***M*** is in out-of-plane direction and *k* is in the film plane. The SW dispersion relation is given by[49]:

$$\omega_{FV} = 2\pi f_{FV} = \gamma \sqrt{(H - 4\pi M_S)\left(H - 4\pi M_S \frac{1-e^{-2dk_{||}}}{kd}\right)} \qquad \ldots\ldots (2.28)$$

When the SW energy is predominantly governed by the exchange interaction at short wavelengths rather than dipolar interactions, they are referred to as exchange SWs[6]. These modes are isotropic and are described by:

$$f = \frac{4Js}{\hbar}[1 - cos(ka)] \qquad \ldots\ldots (2.29)$$

Here, *J* is the exchange integral and *a* is interspinal separation.

Disregarding the anisotropic dipolar effects, the dispersion in the exchange-dominated regime becomes invariant to the magnetization's orientation. Instead, it is governed exclusively by the nearest-neighbor separation ***r*** and the strength of the exchange interaction. This dependence can be determined through the "frozen magnon" approach, derived directly from the electronic structure calculations. For small *k*, the dispersion approximates a quadratic form, with energy

increasing quadratically with momentum $\hbar k$, akin to free electron behavior, enabling the conceptualization of "free electron-like" magnonic materials[50].

The exchange length (l_{ex}) characterizes the competition between the exchange energy and the dipolar energy. This represents the smallest scale at which the magnetization can be twisted to minimize dipolar interactions which can be written as: $l_{ex} = \sqrt{\frac{2A}{\mu_0 M_s^2}}$. … … (2.30)

Also, it is possible to stimulate SWs that propagate perpendicular to the plane of the film, leading to the formation of perpendicular standing SW (PSSW) modes. For a given thickness of d, the dispersion relation for PSSW can be expressed as[51]:

$$f_{PSSW} = \sqrt{(H + \frac{2A}{M_S}\left(\frac{p\pi}{d}\right)^2)(H + \frac{2A}{M_S}\left(\frac{p\pi}{d}\right)^2 + 4\pi M_{e_{ff}}} \quad \ldots\ldots (2.31)$$

where quantization number, p = 1, 2, 3,… and exchange stiffness constant is A.

Additionally, the characteristic dispersion relation considering both dipole and exchange interactions is given by[52]:

$$f_D = \frac{\gamma}{2\pi}[\left(H + 4\pi M_S k_{||}\, d\, sin^2\, \varphi_{k_{||}} + \frac{2A}{M_S}k_{||}^2\right)\left(H + 4\pi M_S - \, 2\pi M_S k_{||}\, d + \frac{2A}{M_S}k_{||}^2\right)]^{1/2} \ldots (2.32)$$

Where $\varphi_{k_{||}}$ is the angle between the applied field H and $k_{||}$.

2.3.2. Magnetic damping

Magnetic damping refers to the energy dissipation mechanisms that causes the gradual loss of magnetization within a magnetic system, leading to equilibrium. This phenomenon is crucial in various technologies, particularly magnetic recording, as it affects how quickly a magnet stabilizes after changes in its magnetic field. For example, in MRAM, increased damping in memory pixels enables faster data writing.

Damping can be intrinsic or extrinsic[53]. It occurs due to the coupling of magnetic modes (electron spins) with non-magnetic modes (electron orbits and lattice vibrations)[54]. Intrinsic damping is fundamental and inevitable, arising from interactions like eddy currents and SOC, as well as magnon–phonon scattering[55, 56]. Extrinsic damping, avoidable in perfect samples, is mainly due to sample inhomogeneities, causing linewidth broadening in FMR experiments.

Researchers can fine-tune the damping properties of magnetic materials for specific technological applications by using advanced techniques like optical heating and precise interface engineering. In spintronics, low-damping materials are ideal for applications requiring long spin coherence times, while high-damping materials are suited for memory and storage applications needing rapid magnetization switching[57, 58]. By choosing materials with the right damping properties, optimal performance in spintronic and magnonic devices can be achieved.

2.3.3. Spin waves in confined magnetic nanostructures

In magnetic thin films, the demagnetization field is negligible due to widely spaced magnetic charges at the boundaries. However, in confined magnetic structures[59] at the sub-micron to nanometer scale, the demagnetization field becomes significant due to the close proximity of magnetic poles at the edges. This effect, influenced by boundary conditions, impacts SW modes in systems like magnetic dots[60, 61], interconnected dots[62, 63], antidots[61, 64], rings, and bi-component structures[65, 66]. The number of SW modes changes, influenced by shape[67], size[38], structure arrangement[68, 69] as well as the magnitude and orientation of external bias magnetic fields[67, 70]. The following section discusses several types of observed SW modes[38].

Centre Mode: This SW mode predominantly distributed over an extended region around the centre of the patterned structures. Its intensity (mostly with highest intensity in FFT spectra) and frequencies exhibit a Kittel-like variation, with a slight decrease in effective magnetization relative to saturation magnetization[71].

Edge Mode: Edge modes (or end modes) are localized SW modes found in regions with reduced effective fields, i.e., localized in the edge demagnetized regions. Consequently, the frequency associated with edge modes is significantly lower compared to centre modes[71].

Quantized Mode: Within laterally confined magnetic structures, standing SW modes form due to the reflection of SWs at boundaries and subsequent superposition. Each mode is characterized by a quantization number similar to a resonator, indicating the number of nodal planes present within the structure along a specific direction[72].

Fig. 2.3(c) illustrates the power and phase distribution of three discrete SW modes within a 2D elliptical dot structure at H = 1 kOe along the x-axis.

2.4. Magneto-optical Kerr Effect (MOKE)

The revelation of the magneto-optic effect uncovered a profound interplay between a material's magnetic moment and the polarization of light waves. Initially identified in transmitted light, researchers observed that linearly polarized light undergoes a rotation in its polarization plane when traversing a magnetized medium[73]. Later, a comparable phenomenon was detected in reflected light, where plane-polarized light transforms into elliptically polarized light—a phenomenon now known as the Kerr effect. This rotation, termed Kerr rotation, is directly proportional to the sample's magnetization $\boldsymbol{M}$[74].

Since its discovery, the Kerr effect has been widely utilized to investigate both static and dynamic responses of magnetic systems. Kerr demonstrated that the polarization axis of a linearly polarized light undergoes a distinctive rotation (Kerr rotation, θ_k) adding an adequate amount of ellipticity (Kerr ellipticity, ε_k) in the electric field vector, which correlate directly with the $\boldsymbol{M}$ of the sample[75]. In the context of reflected light, denoting the parallel and perpendicular components of the electric field vector relative to the incident light as r and k respectively, a relationship is satisfied, given as:

$$\theta_k + i\varepsilon_k = \frac{k}{r} \qquad \ldots\ldots (2.33)$$

Where $k \ll r$.

2.4.1. Origin of MOKE

The origin of MOKE can be understood from both macroscopic and microscopic perspectives[75-78]. Macroscopically, it arises from the antisymmetric, off-diagonal elements in the dielectric tensor, crucial for determining optical properties influenced by the motion of itinerant electrons in a medium. When linearly polarized light propagates through a material, electrons respond with a combination of left and right circular motions of equal magnitude, resulting in no Faraday rotation. However, in the presence of a magnetic field, the additional Lorentz force acts oppositely on these motions, altering their radii differently for left and right circularly polarized light. This difference in radii causes a disparity in dielectric constants, leading to MOKE. This disparity also affects refractive indices for circularly polarized light, inducing a phase difference in reflected light components.

Geometry	Polar	Longitudinal	Transverse
Schematic	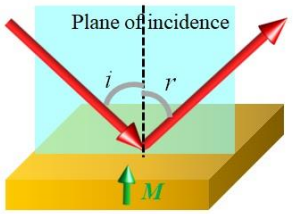	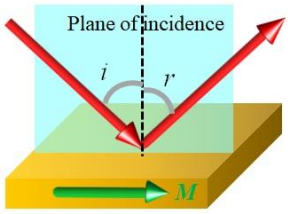	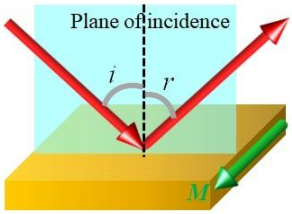
Detection	Out-of-plane	In-plane	In-plane
Variation of polarization	Kerr rotation Kerr ellipticity	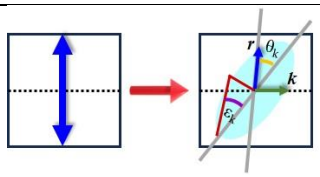	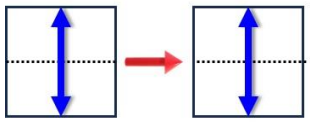
Measurement	Polarization analysis		Intensity measurement

Figure 2.4: Tabular form of the schematic of MOKE measurement geometry, detection geometry, the variation of polarization and the measurement for p-polarized incident light

Quantum mechanically, the Kerr effect in FM materials is attributed to spin-orbit interaction (SOI), coupling electron spin to its motion. This interaction resembles an effective magnetic vector potential ($\boldsymbol{A}$), described by:

$$\boldsymbol{A} \sim \boldsymbol{s} \times \nabla V \quad \ldots\ldots (2.34)$$

where $\boldsymbol{s}$ and ∇V denote electron spin and electric field ($E = -\nabla V$, with V as electric potential), respectively. While this effect exists in all materials, it is more pronounced in FM materials due to the imbalance in electron spin populations within their band structures, unlike non-magnetic (NM) materials where spin cancellation diminishes its prominence.

2.4.2. MOKE geometries

The magneto-optic Kerr effect (MOKE) can be classified into three distinct geometries: polar, longitudinal, and transverse. These classifications are based on the orientation of the sample's magnetization (MMM) relative to the reflecting surface and the incident light beam, as depicted in Fig. 2.4 [74, 79, 80].

In the polar MOKE configuration, $\boldsymbol{M}$ is aligned perpendicular to the reflecting surface and parallel to the plane of incidence. This geometry exhibits the strongest effect among the three and remains observable even under normal light incidence, distinguishing it from the other geometries.

For longitudinal (or meridional) MOKE, ***M*** lies within the plane of the sample and aligns parallel to the plane of incidence. In contrast, transverse (or equatorial) MOKE features ***M*** oriented parallel to the surface and perpendicular to the plane of incidence.

In both polar and longitudinal configurations, the Kerr effect manifests as a subtle rotation of the reflected light's polarization plane, directly proportional to ***M*** and varying in sign with the magnetization's direction. The transverse effect, however, results in a slight alteration of the reflectance for light polarized in the plane of incidence, also proportional to ***M***. Notably, all three geometries are wavelength-dependent, with the magnitude of the effect varying across the light spectrum.

References

[1] J.M.D.Coey, *Magnetism and Magnetic Materials* **2009**.
[2] W. Gerlach, O. Stern, *Zeitschrift für Physik* **1922**, 9, 353.
[3] W. Heisenberg, *Zeitschrift für Physik* **1926**, 38, 411.
[4] P. Weiss, **1907**, 6, 661.
[5] D. J. Griffiths, *Introduction to Electrodynamics, 5th ed. , Cambridge University Press, Cambridge* **2023**.
[6] C. Kittel, *Physical Review* **1948**, 73, 155.
[7] T. Kasuya, *Progress of Theoretical Physics* **1956**, 16, 58.
[8] M. A. Ruderman, C. Kittel, *Physical Review* **1954**, 96, 99.
[9] P. W. Anderson, *Physical Review* **1950**, 79, 705.
[10] H. T. Nembach, J. M. Shaw, M. Weiler, E. Jué, T. J. Silva, *Nature Physics* **2015**, 11, 825.
[11] I. Dzyaloshinsky, *Journal of Physics and Chemistry of Solids* **1958**, 4, 241.
[12] T. Moriya, *Physical Review* **1960**, 120, 91.
[13] A. Soumyanarayanan, N. Reyren, A. Fert, C. Panagopoulos, *Nature* **2016**, 539, 509.
[14] A. N. Bogdanov, U. K. Rößler, M. Wolf, K. H. Müller, *Physical Review B* **2002**, 66, 214410.
[15] D. Coffey, T. M. Rice, F. C. Zhang, *Physical Review B* **1991**, 44, 10112.
[16] A. Fernández-Pacheco, E. Vedmedenko, F. Ummelen, R. Mansell, D. Petit, R. P. Cowburn, *Nature Materials* **2019**, 18, 679.
[17] A. Fert, P. M. Levy, *Physical Review Letters* **1980**, 44, 1538.
[18] M. Bode, M. Heide, K. von Bergmann, P. Ferriani, S. Heinze, G. Bihlmayer, A. Kubetzka, O. Pietzsch, S. Blügel, R. Wiesendanger, *Nature* **2007**, 447, 190.
[19] S. Heinze, K. von Bergmann, M. Menzel, J. Brede, A. Kubetzka, R. Wiesendanger, G. Bihlmayer, S. Blügel, *Nature Physics* **2011**, 7, 713.
[20] S. Heinze, M. Bode, A. Kubetzka, O. Pietzsch, X. Nie, S. Blügel, R. Wiesendanger, *Science* **2000**, 288, 1805.
[21] P. Bak, M. H. Jensen, *Journal of Physics C: Solid State Physics* **1980**, 13, L881.
[22] M. Kuepferling, A. Casiraghi, G. Soares, G. Durin, F. Garcia-Sanchez, L. Chen, C. H. Back, C. H. Marrows, S. Tacchi, G. Carlotti, *Reviews of Modern Physics* **2023**, 95, 015003.

[23] L. Udvardi, L. Szunyogh, *Physical Review Letters* **2009**, 102, 207204.
[24] R. A. Gallardo, D. Cort´es-Ortuño, R. E. Troncoso, and P. Landeros, *Three-Dimensional Magnonics: Layered, Micro- and Nanostructures, edited by G. Gubbiotti* **2019**.
[25] A. N. Bogdanov, U. K. Rößler, *Physical Review Letters* **2001**, 87, 037203.
[26] S. Rohart, A. Thiaville, *Physical Review B* **2013**, 88, 184422.
[27] J.-H. Moon, S.-M. Seo, K.-J. Lee, K.-W. Kim, J. Ryu, H.-W. Lee, R. D. McMichael, M. D. Stiles, *Physical Review B* **2013**, 88, 184404.
[28] P. Bruno, J. P. Renard, *Applied Physics A* **1989**, 49, 499.
[29] W. Palmer, *Physical Review* **1963**, 131, 1057.
[30] D. X. Chen, J. A. Brug, R. B. Goldfarb, *IEEE Transactions on Magnetics* **1991**, 27, 3601.
[31] N. Nakajima, T. Koide, T. Shidara, H. Miyauchi, H. Fukutani, A. Fujimori, K. Iio, T. Katayama, M. Nývlt, Y. Suzuki, *Physical Review Letters* **1998**, 81, 5229.
[32] S. Pal, B. Rana, O. Hellwig, T. Thomson, A. Barman, *Applied Physics Letters* **2011**, 98, 082501.
[33] A. D. Kent, *Nature Materials* **2010**, 9, 699.
[34] R. P. Cowburn, A. O. Adeyeye, M. E. Welland, *Physical Review Letters* **1998**, 81, 5414.
[35] M. E. Schabes, H. N. Bertram, *Journal of Applied Physics* **1988**, 64, 1347.
[36] S. Jain, Y. Ren, A. O. Adeyeye, N. Singh, *Physical Review B* **2009**, 80, 132401.
[37] V. V. Kruglyak, P. S. Keatley, R. J. Hicken, J. R. Childress, J. A. Katine, *Physical Review B* **2007**, 75, 024407.
[38] A. Barman, S. Mondal, S. Sahoo, A. De, *Journal of Applied Physics* **2020**, 128, 170901.
[39] A. Kirilyuk, A. V. Kimel, T. Rasing, *Reviews of Modern Physics* **2010**, 82, 2731.
[40] F. Bloch, *Zeitschrift für Physik* **1930**, 61, 206.
[41] M. Krawczyk, D. Grundler, *Journal of Physics: Condensed Matter* **2014**, 26, 123202.
[42] B. Lenk, H. Ulrichs, F. Garbs, M. Münzenberg, *Physics Reports* **2011**, 507, 107.
[43] A. V. Chumak, V. I. Vasyuchka, A. A. Serga, B. Hillebrands, *Nature Physics* **2015**, 11, 453.
[44] L. D. Landau, E. M. Lifshitz, **1935**.
[45] T. L. J. I. T. o. M. Gilbert, **2004**, 40, 3443.
[46] B. A. Kalinikos, A. N. Slavin, *Journal of Physics C: Solid State Physics* **1986**, 19, 7013.
[47] J. R. Eshbach, R. W. Damon, *Physical Review* **1960**, 118, 1208.
[48] R. W. Damon, J. R. Eshbach, *Journal of Applied Physics* **1960**, 31, S104.
[49] V. E. Demidov, M. P. Kostylev, K. Rott, P. Krzysteczko, G. Reiss, S. O. Demokritov, *Applied Physics Letters* **2009**, 95, 112509.
[50] R. W. Damon, J. R. Eshbach, *Journal of Physics and Chemistry of Solids* **1961**, 19, 308.
[51] M. G. C. a. D. J. Lockwood, *Light Scattering in Magnetic Solids, Wiley* **1986**.
[52] R. Arias, D. L. Mills, *Physical Review B* **1999**, 60, 7395.
[53] A. Barman, J. Sinha, Springer International Publishing, 2018.
[54] V. Kamberský, *Czechoslovak Journal of Physics B* **1976**, 26, 1366.
[55] B. Heinrich, J. F. Cochran, R. Hasegawa, *Journal of Applied Physics* **1985**, 57, 3690.

[56] J. Lindner, K. Lenz, E. Kosubek, K. Baberschke, D. Spoddig, R. Meckenstock, J. Pelzl, Z. Frait, D. L. Mills, *Physical Review B* **2003**, 68, 060102.
[57] S. Manipatruni, D. E. Nikonov, I. A. Young, *Physical Review Applied* **2016**, 5, 014002.
[58] W. Yu, J. Lan, J. Xiao, *Physical Review Applied* **2020**, 13, 024055.
[59] B. H. e. al., *Spin Dynamics in Confined Magnetic Structures I, Springer* **2002**.
[60] B. Rana, D. Kumar, S. Barman, S. Pal, Y. Fukuma, Y. Otani, A. Barman, *ACS Nano* **2011**, 5, 9559.
[61] B. Rana, D. Kumar, S. Barman, S. Pal, R. Mandal, Y. Fukuma, Y. Otani, S. Sugimoto, A. Barman, *Journal of Applied Physics* **2012**, 111, 07D503.
[62] S. Sahoo, S. N. Panda, S. Barman, Y. Otani, A. Barman, *Journal of Magnetism and Magnetic Materials* **2021**, 522, 167550.
[63] A. K. Mondal, C. Banerjee, A. Adhikari, A. K. Chaurasiya, S. Choudhury, J. Sinha, S. Barman, A. Barman, *Physical Review B* **2020**, 101, 224426.
[64] K. Dutta, A. De, S. Mondal, S. Barman, Y. Otani, A. Barman, *Journal of Alloys and Compounds* **2021**, 884, 161105.
[65] S. Choudhury, S. Saha, R. Mandal, S. Barman, Y. Otani, A. Barman, *ACS Applied Materials & Interfaces* **2016**, 8, 18339.
[66] C. Kumar, P. K. Pal, A. Barman, *Physical Review B* **2024**, 109, 075407.
[67] B. K. Mahato, S. Choudhury, R. Mandal, S. Barman, Y. Otani, A. Barman, *Journal of Applied Physics* **2015**, 117, 213909.
[68] S. Choudhury, S. Barman, Y. Otani, A. Barman, *ACS Nano* **2017**, 11, 8814.
[69] S. Mondal, S. Barman, S. Choudhury, Y. Otani, A. Barman, *Journal of Magnetism and Magnetic Materials* **2018**, 458, 95.
[70] K. Adhikari, S. Barman, R. Mandal, Y. Otani, A. Barman, *Physical Review Applied* **2018**, 10, 044010.
[71] A. Barman, S. Barman, *Physical Review B* **2009**, 79, 144415.
[72] P. K. Pal, S. Majumder, Y. Otani, A. Barman, *Advanced Quantum Technologies* **2023**, 6, 2300003.
[73] T. M. M. Faraday, R. I. o. G. Britain, Faraday's Diary: Nov. 24, 1855-Mar. 12, 1862 (G. Bell and sons, ltd.), **1936**

[74] J. Kerr, *The London, Edinburgh, and Dublin Philosophical Magazine and Journal of Science* **1878**, 5, 161.
[75] C.-Y. You, S.-C. Shin, *Journal of Applied Physics* **1998**, 84, 541.
[76] P. N. Argyres, *Physical Review* **1955**, 97, 334.
[77] Z. Q. Qiu, S. D. Bader, *Journal of Magnetism and Magnetic Materials* **1999**, 200, 664.
[78] P. Bruno, Y. Suzuki, C. Chappert, *Physical Review B* **1996**, 53, 9214.
[79] C. A. Fowler, E. M. Fryer, *Physical Review* **1954**, 94, 52.
[80] M. R. Parker, *Physica B+C* **1977**, 86-88, 1171.

Chapter 3

3. Methods

3.1. Sample Fabrication

3.1.1. Sputtering

Sputtering deposition is a type of physical vapor deposition (PVD) method used to create high-quality continuous films and multilayers within a highly controlled vacuum environment, typically at pressures of approximately 10^{-7} Torr or better, as illustrated in Fig. 3.1. The core components of a sputtering unit include an anode, which houses the substrate and its holder, a high-vacuum chamber, and a cathode, comprising the target material. To initiate the process, a high-voltage power supply generates and maintains a neutral gas plasma within the vacuum chamber, where atoms, ions, and electrons coexist in a balanced state.

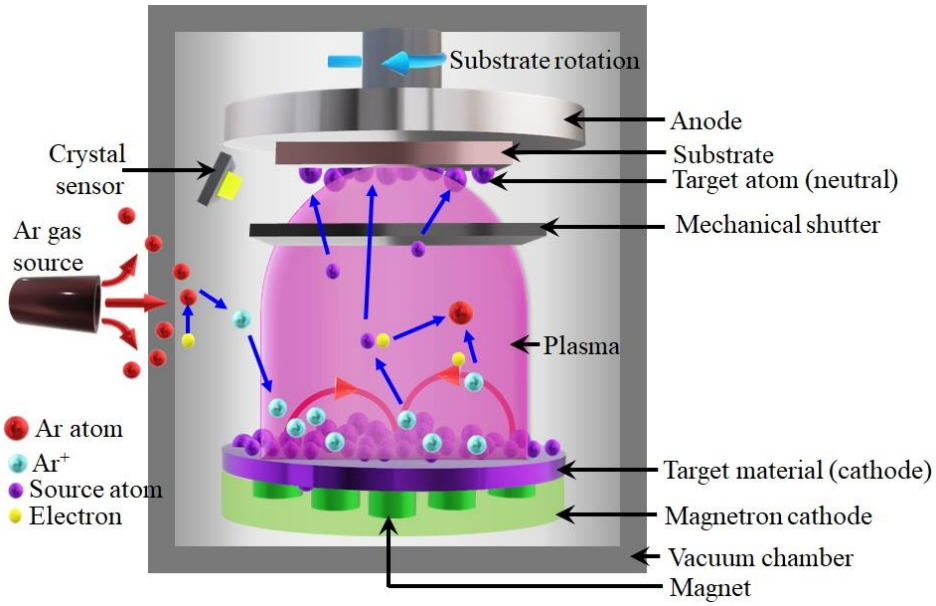

Figure 3.1. Schematic diagram of RF-DC magnetron sputtering

When activated, free electrons within the plasma swiftly disperse from the negatively charged cathode, initiating a cascade of interactions. These high-energy electrons collide with neutral argon atoms, resulting in the formation of positively charged ions like Ar^+ [1]. Drawn to the negatively charged target, these ions bombard its surface, ejecting neutral atoms in the process.

The liberated atoms travel toward the substrate (anode), where they condense to form a thin, uniform film. Despite its utility, conventional sputtering faces limitations such as low deposition rates and excessive heating of the target caused by prolonged electron bombardment [2]. Magnetron sputtering addresses these challenges by employing a strong magnetic field near the target, which forces electrons to spiral along the magnetic flux lines. This not only enhances the ionization efficiency but also minimizes electron movement toward the substrate, mitigating overheating while improving film quality.

This increases the likelihood of ionizing Ar atoms within the chamber, leading to more atoms being ejected from the target. Consequently, magnetron sputtering enhances the efficiency of the sputtering process while minimizing impurity formation in the resulting thin film.

3.1.2. Electron-beam evaporation

Electron-beam evaporation (EBE)[3] represents an additional variant of PVD processes, characterized by the generation of a concentrated electron beam through the thermionic emission of a heated tungsten filament. The emitted electrons are guided towards the source material via the manipulation of electric and magnetic fields. The source material is contained within a crucible and exposed to the electron beam emitted from the electron gun[4], which is accelerated by a high-voltage electrode and focused onto the material using magnetic fields. Upon exposure to the electron beam, the source material undergoes melting and subsequent evaporation. The evaporated material then impinges upon the substrate surface, where it condenses to form a thin layer of the source material. An advantage of EBE lies in its capability to deposit multiple materials without the need to break the vacuum or vent the chamber. This is achieved by housing different source materials within separate crucibles, which can be arranged in a linear or circular configuration. Consequently, the versatility of EBE facilitates the deposition of complex multilayer structures with precise control over material composition and thickness.

3.1.3. Electron-beam lithography

Electron beam lithography (EBL)[5] is a widely utilized technique for the fabrication of one- and two-dimensional nanostructures. It enables the creation of feature sizes ranging from submicrometers to a few nanometers. During this process, an electron-sensitive resist is exposed

to electron beams, allowing for the patterning of a clean substrate (bottom-to-top approach) or a thin film (top-to-bottom approach). The patterning is guided by a computer-aided design (CAD) system, enabling maskless pattern generation. Upon exposure, the resist undergoes a transformation, becoming either soluble (positive resist) or insoluble (negative resist) to the developer solvent, depending on the type of resist used. Typically, a bilayer resist (e.g., PMMA/MMA) or a monolayer resist (e.g., PMMA) is spin-coated onto a pre-cleaned substrate before EBL patterning. Following exposure, the resist is immersed in a developer solution compatible with the resist to develop the desired pattern.

3.1.4. Electrodeposition

Electrodeposition[6, 7] of metals and alloys entails the reduction of metal ions from various electrolytes via the application of an electric current. When the electrode potential exceeds the energy level of an empty molecular orbital in the electrolyte, electrons move from the electrode to the solution, causing reduction, and vice versa. These reactions halt upon reaching equilibrium. Hence, an external potential difference is required to disrupt equilibrium, enabling metal deposition or dissolution, known as electrodeposition. It is mainly governed by the Nernst equation:

$$E = E_0 + \frac{RT}{nF} ln(a_{ion}) \quad \text{... .... (3.1)}$$

where, E_0 represents the standard electrode potential, denoting the potential difference between the electrode and the solution when the ion activity (a_{ion}) is one. F stands for Faraday's constant, R represents the gas constant, and T is the temperature[8].

A standard electrode maintains a constant electrode potential due to the consistent activity of ions. Examples of standard electrodes utilized in our laboratory include Ag/AgCl, Hg/Hg_2Cl_2 (saturated calomel electrode), and $Cu/CuSO_4$.

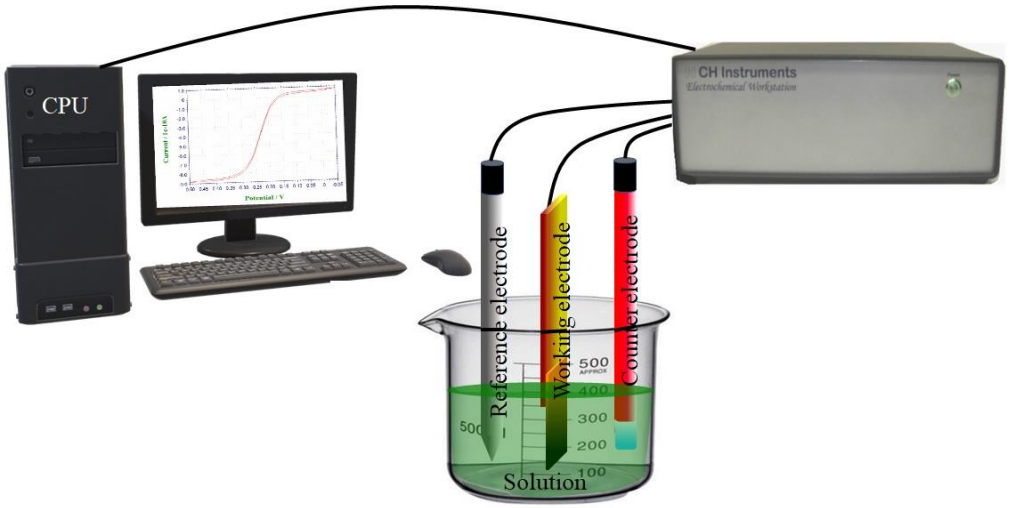

Figure 3.2. Schematic diagram of electrodeposition setup

Different techniques of electrodeposition include: galvanostatic electrodeposition, potentiostatic electrodeposition, DC electrodeposition, pulsed electrodeposition etc. Potentiostatic electrodeposition involves an electrolytic cell with a reference electrode alongside the working (cathode) and counter electrodes. Deposition occurs at a constant potential between the working and reference electrodes. Optimizing deposition quality relies on finding the ideal potential where the rate of deposition is optimum without compromising quality of the electrodeposits. This optimum potential (V_T) is determined via cyclic voltammetry (CV) or linear sweep voltammetry (LSV) technique. In CV, the potential of the working electrode is varied linearly and at a constant rate relative to the reference electrode, enabling the precise identification of the threshold voltage (V_T). Once determined, this deposition potential is maintained at the working electrode to facilitate electrodeposition. For our experiments, the CH Instruments 600E electrochemical workstation was utilized for both CV and electrodeposition, as depicted in Fig. 3.2. Pulsed electrodeposition involves alternating the potential of the working electrode between two levels (V_1 and V_2) in pulses, with specific duty cycles and time periods tailored to the desired outcome. This method often enhances deposit quality, especially for multilayer metal deposition, where one metal is deposited at V_1 and another preferentially at V_2.

Template-assisted synthesis of nanowires begins with cleaning porous templates like porous anodic alumina (AAO)/polycarbonate template (Whatman/Synkera Technologies) with sodium lauryl sulfate (SLS) to remove any contaminants. One side of the template is then coated with

a thick layer (~200nm) of gold/silver using thermal evaporation/sputtering, creating a working electrode (WE). The coated template is attached to a copper base plate with insulating tape, and electrolyte wets only the exposed portion of the AAO template. The potential of the WE relative to a standard reference electrode (RE) is varied to find the optimal deposition potential via cyclic voltammetry (CV). Deposition occurs at this optimum potential. During deposition, ions deposit onto the 200 nm thick silver coating, eventually filling the pores and forming nanowire arrays. The current between the WE and a platinum counter electrode is recorded over time, monitoring deposition progress with a current versus time plot. Deposition continues until current saturation is reached, ensuring complete pore filling. Excess growth is then removed by mechanical polishing or 'inductive coupled plasma reactive ion etching' (ICP-RIE) once the templates are fully filled.

3.2. Sample Characterization

3.2.1. Scanning electron microscopy (SEM)

SEM imaging is employed to verify the completion of lift-off processes and to examine the morphology and topography of sample surfaces. In this technique, an electron beam is generated by a cathode, either through thermionic emission or electric field [9, 10] (field emission SEM: FESEM), and then focused onto the sample using electromagnetic lenses as shown in Fig. 3.3. The electron beam's short wavelength allows it to detect features ranging from ~1-2 nm to 1-2 mm.

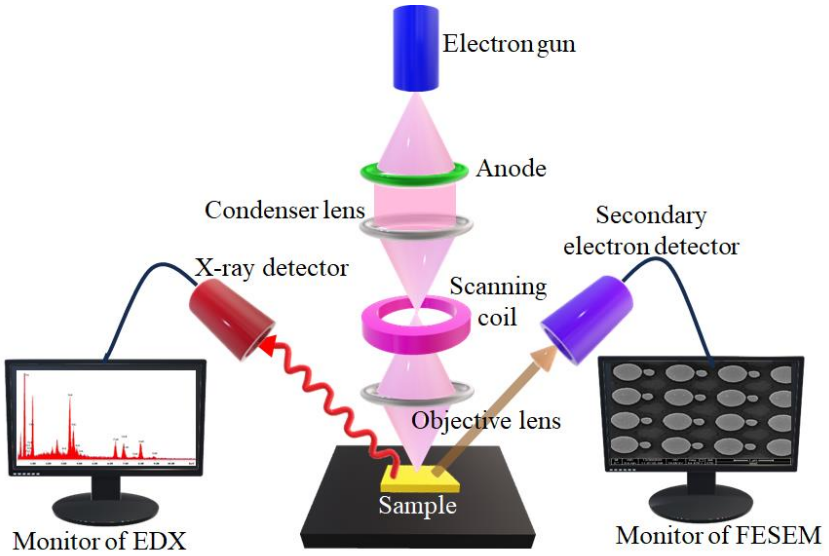

Figure 3.3. Schematic diagram of SEM and EDS. Monitor at left and right captures the images of EDS and SEM, respectively.

Upon interaction with the sample, the electron beam manifests various behaviors, including the emission of secondary electrons, backscattering, transmission, absorption (generating heat), production of characteristic X-rays, and elastic and inelastic scattering. Any discrepancy between the numbers of incoming and outgoing electrons results in sample charging, which can compromise image quality. To mitigate this effect, samples, often insulators, are coated with a thin layer of metallic film (mainly gold). In most instances, electron-sensitive detectors capture secondary electrons to produce SEM images, enabling exploration of surface features and providing three-dimensional insights. In this study, the FEI Quanta 200 (at SNBNCBS) SEM was utilized to image two-dimensional nanostructures and thin films.

3.2.2. Energy dispersive Spectroscopy (EDS)

EDS serves as a powerful, non-invasive technique for identifying elemental composition and conducting chemical analysis of materials within a given sample. [10]. Typically, in SEM, utilizing a specialized EDS detector in conjunction with spectrum analyzer software for detection. The fundamental principle underlying EDS lies in the unique atomic structure of each element, which corresponds to its distinct characteristic X-ray emission. When high-energy charged particles, such as electrons or protons, impinge upon the sample, they excite and displace electrons from inner atomic shells, resulting in electron vacancies. Subsequently, electrons from outer shells transition to fill these vacancies, emitting characteristic X-rays in

the process. The emitted X-rays possess energy that directly reflects the difference between the energy levels of the electron shells involved in the transition. These emitted X-rays are then captured by the EDS detector (schematically shown in Fig. 3.3.) to generate EDS spectra, facilitating the identification and quantification of elemental constituents present within the sample.

3.2.3. X-ray diffraction (XRD)

XRD[11] technique is invaluable for probing the crystalline structure of materials, encompassing atomic arrangement, crystallite size, and imperfections. In XRD, a beam of X-rays, typically copper K_α radiation with a wavelength of approximately 1.5418 Å, is directed onto the sample, where it interacts with the electron clouds surrounding atoms in the crystal lattice. Upon interaction, the X-rays are diffracted by the atoms' electron clouds, forming secondary spherical waves. Constructive interference occurs according to Bragg's law:

$$2d\ sin\ \theta = n\lambda \qquad \text{... ... (3.2)}$$

where d represents the distance between atomic planes, θ denotes the incident angle, n is any integer, and λ signifies the X-ray wavelength.

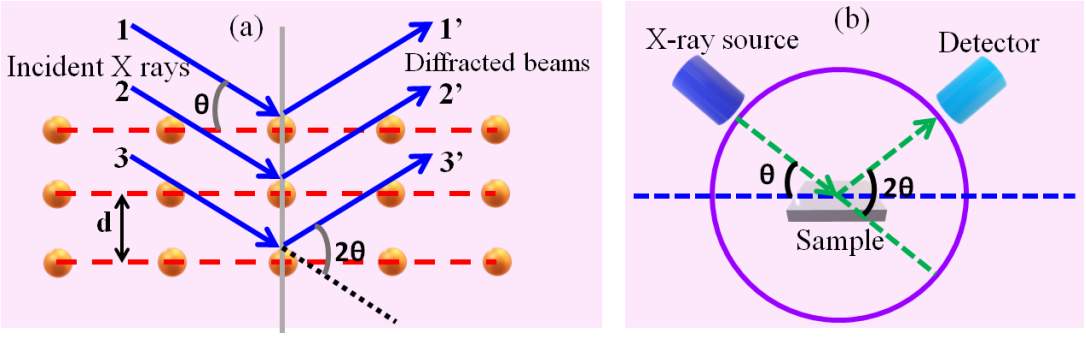

Figure 3.4. Schematic diagram of (a) X-ray diffraction, (b) X-ray diffractometer

The Scherrer equation provides a direct formula for estimating crystallite size, given as:

$$D = \frac{k\lambda}{\beta\ cos\ \theta} \qquad \text{... ... (3.3)}$$

In XRD analysis, the angle of incidence of the X-ray beam is methodically altered, and the reflected intensities are recorded as a function of the reflection angle (2θ) relative to the incident

beam. These diffraction patterns are subsequently examined to calculate interplanar spacings, which are compared against standard reference data from repositories such as the Inorganic Crystal Structure Database (ICSD) or the International Centre for Diffraction Data (ICDD).

3.2.4. Atomic force microscopy (AFM)

The AFM [12] is a cornerstone instrument in materials science, including the investigation of soft biological specimens, for probing local properties such as morphology, thickness and roughness. Typically, the AFM probe comprises a cantilever with a sharp tip, enabling surface scanning with resolutions exceeding 100 times the optical diffraction limit. Information regarding the specimen is extracted through the measurement of force interactions between the tip and the specimen.

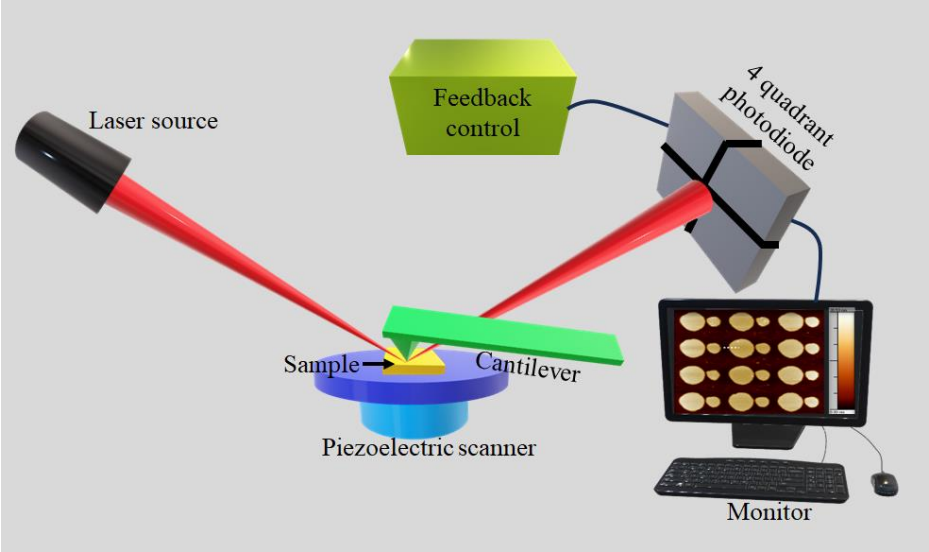

Figure 3.5. Schematic diagram of AFM

During scanning, the tip undergoes lateral and vertical deflections owing to various forces, encompassing van der Waals, capillary, chemical bonding, electrostatic, and magnetic forces. A laser beam, precisely directed onto the tip, detects its deflection, subsequently captured by a four-quadrant photodiode. This arrangement facilitates the acquisition of a two-dimensional image detailing local properties via raster scanning. The sample is positioned on top of a piezo-electric (PZ) controller, crucial in orchestrating the raster scan, contributing to the precise manipulation of the specimen during imaging, as schematically depicted in Fig. 3.5.

AFM operates across mainly three modes: i) *Contact mode*, also termed static mode AFM, involves maintaining a constant repulsive force between the tip and the sample surface using a feedback amplifier, thereby safeguarding the sample from potential damage. ii) *Non-contact mode*, or dynamic mode AFM, sees the tip oscillating in close proximity to the sample surface with minimal amplitude, detecting weak forces like van der Waals. Alterations in oscillation parameters yield topographic insights. iii) *Tapping mode*, employs a vertically oscillating cantilever interacting with the sample at or near its resonant frequency via a piezoelectric crystal. This mode reduces lateral force interactions between the tip and sample, with fluctuations in oscillation amplitude utilized to discern and quantify surface features.

As previously mentioned, AFM possesses the capability to detect various forces, including magnetic interactions, with magnetic force microscopy (MFM)[13] being a prominent variation utilized for revealing the magnetic configuration of a sample's surface. MFM employs a cantilever tip coated with a thin magnetic layer featuring high coercivity, such as cobalt (Co), ensuring the preservation of its magnetization state during imaging. Upon approaching the sample, the tip discerns atomic, electrostatic, and magnetic forces. However, to extract the magnetic signal contrast, a dual scan approach is necessary. Following the acquisition of an AFM image, the tip undergoes a secondary scan over the sample at an increased height. The MFM operation can vary between static and dynamic modes, contingent upon the strength of the stray field emanating from the sample.

3.2.5. Transmission electron microscopy

TEM employs electron diffraction to characterize materials' internal structure. A beam of electrons, with wavelengths typically below 1 Å, passes through a thin specimen, typically an ultrathin section or a suspension on a grid, generating diffracted and non-diffracted electrons. Diffracted electrons contribute to image contrast according to Bragg's law. The diffraction pattern is subjected to an inverse Fourier transformation, creating a highly magnified image. To enhance intensity contrast in amplitude or diffraction contrast imaging, an objective aperture is employed to filter out specific electrons. With its superior resolution, TEM surpasses light microscopes, leveraging the shorter de Broglie wavelength of electrons to reveal intricate details at atomic scales. In TEM, fundamental imaging modes such as phase contrast imaging or high-

resolution TEM (HRTEM) are employed to visualize atomic-scale structures, including lattice fringes. This

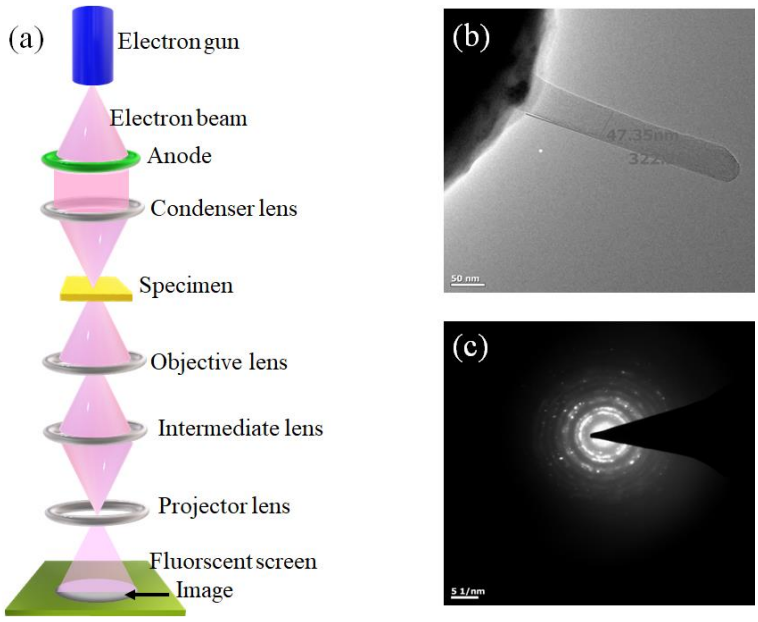

Figure 3.6. (a) Schematic diagram of TEM, (b) HRTEM image of an electrodeposited cobalt nanowire (Co NW), (c) SAED pattern showing polycrystalline nature of the Co NW

capability enables the examination of atomic arrangements within crystals. Additionally, selected area electron diffraction (SAED) serves as a crystallographic experimental technique within TEM. SAED patterns are generated when a focused electron beam interacts with a selected area of the specimen. Each spot within the resulting pattern corresponds to a diffraction condition satisfied by the crystal lattice, providing valuable insights into its structural properties[14].

In sample preparation for HRTEM, the nanowire-deposited in an anodic aluminium oxide (AAO) template undergoes complete etching using a 6M NaOH solution, followed by thorough rinsing with distilled water. Subsequently, the prepared sample is sprayed onto a carbon-coated copper grid for imaging.

3.2.6. Raman spectroscopy

Raman spectroscopy, named after physicist C. V. Raman[15], is a spectroscopic method primarily employed to analyze vibrational modes of molecules, with the potential to detect rotational and other low-frequency modes. It offers a structural fingerprint enabling the identification of

molecules, with micro-Raman spectroscopy being particularly informative[16]. Scattering mechanism involves the inelastic scattering of photons from molecules, altering their energy in the process. The discrepancy in energy between the incident and scattered photons is termed the Raman shift. This energy differential provides valuable insights into the level of phonon excitation and alterations in the electronic state of a material due to the scattering event.

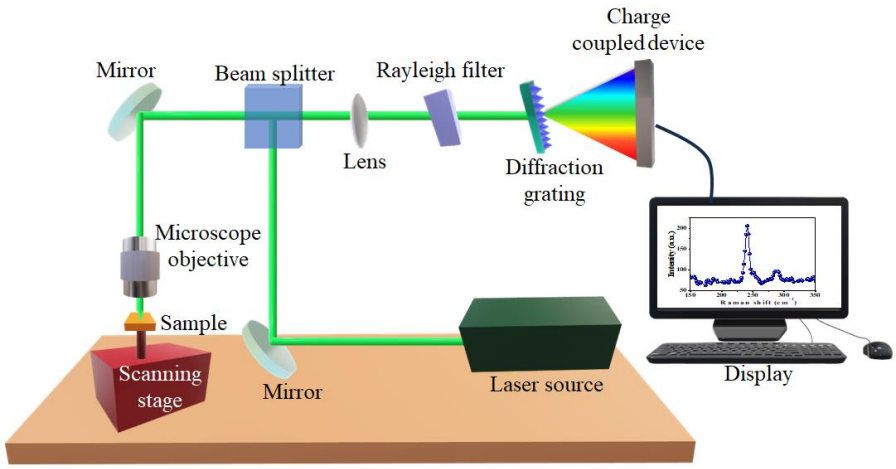

Figure 3.7. Schematic diagram of micro-Raman spectroscopy

Raman scattering manifests in two primary forms: Stokes and anti-Stokes scattering. In Stokes scattering, the energy of scattered photons decreases, while the molecules assume a higher vibrational energy state post-scattering. Conversely, in anti-Stokes Raman scattering, photon energy increases as vibrational energy states decrease.

Optical fiber cables are utilized to capture the transmitted laser beams from the sample, with a charge-coupled device (CCD) subsequently displaying the resultant Raman spectrum. In the specific context of this thesis work, micro-Raman spectroscopy was employed to ascertain peak position, quality, and the number of 2D TMD layers. The experimental setup, schematically shown in Fig. 3.7., includes a 532 nm wavelength argon-ion laser, a thermoelectrically-cooled CCD detector featuring 1024×256-pixel resolution, a 100X objective, and a 600 gr/mm grating with a numerical aperture of 0.9, resulting in a laser spot diameter of approximately 0.7 μm.

3.2.7. Vibrating sample magnetometer (VSM)

The VSM serves as a fundamental tool for characterizing magnetic materials[17], facilitating the precise examination of their static magnetic properties. This is achieved by measuring the

magnetic moment (magnetization) as a function of both magnetic field strength and temperature.

The operational principle of VSM relies on Faraday's law, stating that any alteration in magnetic flux through a coil induces an electromotive force (emf) within it, as expressed by:

$$E = -NA\frac{dB}{dt} \quad \text{... .... (3.4)}$$

Here, E represents the induced emf, while A and N denote the area and number of turns of the coil, respectively. By substituting B with $(H + 4\pi M)$ in Eq. (1) and assuming a constant applied field, we get,

$$E = -NA\frac{dM}{dt} \quad \text{... .... (3.5)}$$

Equation (2) demonstrates that the electromotive force (emf) induced in the coil is directly linked to the sample's magnetization, provided the initial magnetization remains negligible compared to the magnetization driven by the applied field.

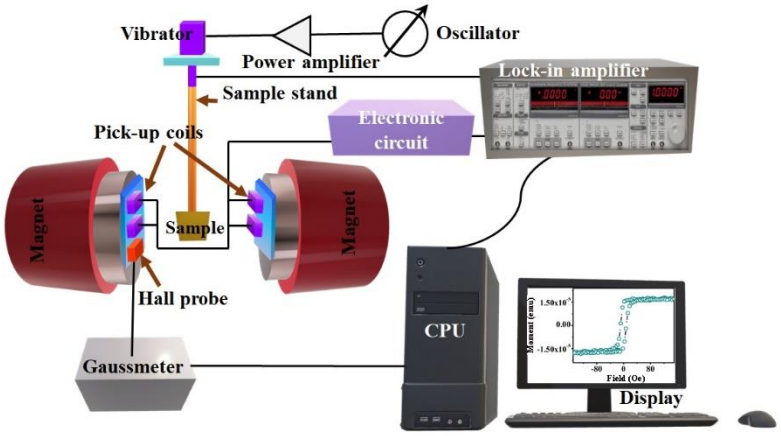

Figure 3.8. Schematic diagram of VSM

In a VSM setup, depicted in Fig. 3.8, the sample is placed within a uniform magnetic field established between two pole pieces. It is secured using a vertical, nonmagnetic support, commonly crafted from quartz or plastic, which is connected to a piezoelectric transducer. A sinusoidal electrical signal, produced by an oscillator, is transformed into mechanical vibrations by the transducer. These vibrations cause the sample to oscillate, creating disturbances in the external magnetic field, which are subsequently detected by the pick-up coils. The changing magnetic flux piercing the coils induces a corresponding emf, described by:

$$E = -m\omega z y_0 N N_C G \cos(\omega t) \quad \ldots\ldots (3.6)$$

where ω *and* z represent the frequency and amplitude of vibration, respectively, y_0 is the distance between two pick-up coils, N_C is the number of pick-up coils, and G is the geometric factor of the sample. As the sample vibrates vertically, it generates an induced voltage in the pick-up coil, directly proportional to its magnetization. This voltage is precisely recorded by a lock-in amplifier, which synchronizes with the piezoelectric frequency as a reference. To monitor the applied magnetic field, a Hall sensor is strategically placed adjacent to the pick-up coil, ensuring accurate field measurements. In this study, VSM was employed to analyze M-H curves of various samples at room temperature.

3.2.8. Static magneto optical Kerr effect magnetometry

The static magneto-optical Kerr effect (static MOKE) serves as a powerful method for probing the static magnetization characteristics of ferromagnetic systems, such as thin films and confined magnetic structures. This technique leverages the fundamental principle of the Kerr effect, wherein the plane of polarization of light undergoes a rotation influenced by the material's magnetization.

The experimental setup [18], presented in Fig. 3.9., involves a continuous wave He-Ne laser with a wavelength (λ) of 632 nm serving as the light source. A variable attenuator controls the input laser intensity falling on the sample depending on the sample's damage threshold. The laser beam with a spot size of ~ 100 μm, first passes through a Glan-Thomson polarizer to become an s-polarized light, is guided by two mirrors (M1 and M2) and focused by a lens (L1) onto the magnetic sample. The sample is precisely mounted at the midpoint between the two pole pieces of an electromagnet, with the field varied by adjusting the current in its coil, on a high precession rotating mount. Subsequently, the reflected beam from the sample surface is collimated by a single lens (L2) / lens assembly (not shown here) towards an optical bridge detector (OBD) passing through a photoelastic modulator (PEM) operating at a frequency of 1 kHz for detecting rotation within the plane of polarization, while the frequency of the PEM provides the reference signal for the lock-in amplifier. Phase-sensitive detection is achieved using a combination of the lock-in amplifier and PEM to enhance the signal-to-noise ratio. Monitoring of the Kerr signal during magnetization reversal measurement is facilitated through a LabVIEW-based software.

In our study, we utilized longitudinal MOKE geometry to measure Kerr rotation as a function of applied magnetic field (hysteresis loop). For each magnetic field strength, the Kerr rotation is analyzed using the OBD. The OBD operates on a straightforward principle: a polarized beam splitter (PBS), essentially a Wollaston prism within the OBD, divides the incoming beam into two linearly polarized components orthogonal to each other (refer to Fig. 3.10). Two silicon photodiodes convert these optical signals into electrical signals (denoted as A and B). The variation in Kerr rotation is encoded in the differential signal (A-B), while the sum signal represents the reflectivity (A+B).

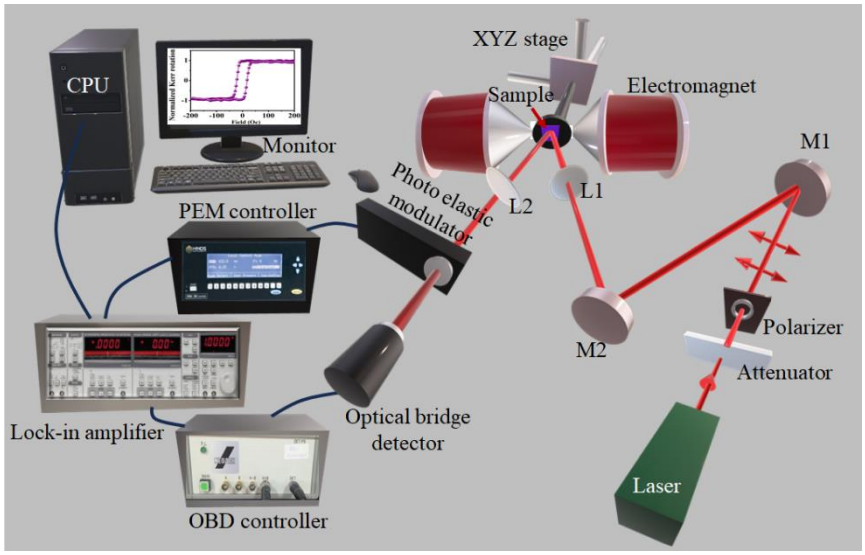

Figure 3.9. Schematic diagram of the static MOKE set in our lab at SNBNCBS

Prior to the application of any external magnetic field, the PBS axis is adjusted to achieve a balanced state where A equals B. This condition is termed the balanced state of the OBD. As an external magnetic field is applied, the magnetization of the sample alters, resulting in a change in the polarization plane and thus a non-zero value for A-B emerges. The output signal from the OBD is detected by a lock-in amplifier operating in a phase-sensitive manner. To minimize the signal-to-noise ratio, the amplifier receives a reference signal at 50 kHz generated by the PEM placed in the path of the reflected beam.

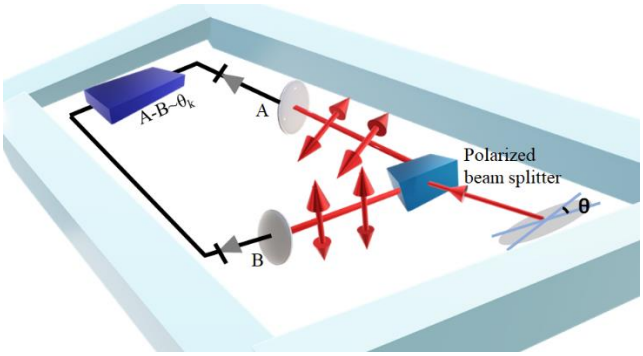

Figure 3.10. Schematic diagram of the OBD

The PEM introduces a periodic phase shift at 50 kHz between the two optical components. The lock-in amplifier selectively detects harmonics of this modulation frequency, thereby eliminating other components and reducing noise. The Kerr rotation, measured in volts, can be converted to angular units by multiplying with a calibration factor. This calibration factor is determined by recording the rotation (in degrees) of the PBS axis on both sides from its balanced state and noting the corresponding voltages.

3.3. Measurement Techniques for Magnetization Dynamics

3.3.1. Brillouin light scattering (BLS) spectroscopy

The technique of light scattering stands as one of the most potent methods for exploring diverse physical properties across gases, liquids, and solids. In this method, incident light interacts with a sample, and the resulting scattered light contains valuable information regarding numerous crucial physical characteristics. Raman scattering, for instance, involves incident photons interacting with the rotational or vibrational degrees of freedom within the system[15]. Brillouin light scattering (BLS), on the other hand, entails the scattering of photons from low-frequency excitations, such as phonons, magnons, and plasmons. BLS offers a non-contact and non-invasive means of measuring elastic properties across various materials, ranging from water [19, 20], solids [21], to organic materials like the eye lens [22]. In this thesis, our focus lies specifically on investigating the contribution of magnons within ferromagnetic heterostructures and nanostructures utilizing BLS.

In 1922, L. Brillouin [23] and Mandelstam [23, 24] independently forecasted the occurrence of light scattering from acoustic waves. Subsequently, in 1930, Gross experimentally verified this phenomenon of light scattering in liquids [25]. The advent of the laser during the 1960s marked

a transformative period in this research domain. However, it was not until 1971, when Sandercock engineered a sophisticated spectrometer, that scientists could explore for detecting acoustic waves and SWs in optically opaque materials[24]. A pivotal innovation of this spectrometer is its utilization of two Fabry-Pèrot interferometers, enabling the scattered light to traverse multiple passes for a substantial enhancement in the sensitivity of a Fabry-Pèrot interferometer[24] . By employing two interferometers in tandem, Sandercock and Wettling successfully detected both surface and bulk SWs in polycrystalline films of Fe and Ni [25].

To maintain the precise alignment of etalon mirrors over extended periods, several strategies have been developed and applied. First, minimizing the impact of ground vibrations is essential, often accomplished by employing an optical table or an actively stabilized platform as a secure base for the etalon mirrors [26]. Second, thermal and acoustic disturbances can be mitigated by enclosing the interferometer within a specially designed housing lined with materials for soundproofing and thermal insulation. Lastly, the active stabilization system is a cornerstone of this approach, ensuring consistent parallelism and synchronization between the pairs of etalon mirrors. Since then, BLS has emerged as a valuable asset in magnetism research, thanks to its versatility in handling samples and its capabilities in high-frequency, phase, time, and localized spatial resolution. Additional advantages include:

(i) The capacity to assess thermal excitations under ambient conditions. (ii) Exploration of SW responses across a wide frequency spectrum ranging from 2 GHz to 500 GHz, with a digital resolution as fine as 30 MHz. (iii) Facilitation of the determination of various magnetic properties of a ferromagnetic material, such as saturation magnetization, intra and inter-layer exchange constant, magnetic anisotropy, interfacial Dzyaloshinskii-Moriya Interaction (iDMI), effective damping, spin-mixing conductance, and interfacial parameters between different magnetic materials, through BLS. (iv) Examination of SW dispersions encompassing a range of absolute values and orientations of the corresponding wave vectors across all three possible applied magnetic field geometries.

3.3.1.1. Working principles

In BLS spectroscopy, a highly monochromatic laser beam is directed onto the sample surface. The majority of incident light undergoes either absorption or reflection, with only a small fraction scattering both elastically and inelastically due to thermally excited SWs in the sample.

In elastic scattering, such as Rayleigh scattering, the energy or frequency of scattered photons remains constant, whereas in inelastic scattering, the energy or frequency of the scattered beam is altered, attributed to the frequency of SWs present in the sample.

The backscattered light, positioned at a 180° angle from the incident light, is collected by the same lens used to focus the incident beam onto the sample surface, within a defined solid angle. This configuration, known as the 180° backscattered geometry, offers several advantages: (i) it optimizes the magnitude of the SW wave vector involved in the 180° backscattered process, and (ii) it minimizes phonon contributions after isolating the scattered beam from the reflected beam. Furthermore, a single 90° analyzer in the path of the scattered beam is employed to block the remainder of the phonon component, allowing only the magnon portion to pass through.

The scattered light is subjected to frequency analysis using a high-resolution (3+3)-pass tandem Fabry-Pèrot interferometer (TFPI) to characterize the properties of surface and bulk magnons.

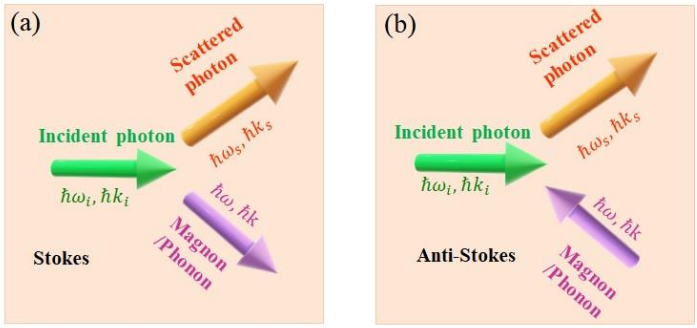

Figure 3.11. Schematic representation of the (a) Stokes, (b) Anti-Stokes processes in BLS.

The phenomenon of inelastic scattering can be elucidated as a quantum mechanical collision between a photon and a magnon, illustrated in Fig. 3.11.(a)-(b). Photons with energy $\hbar\omega_i$ and momentum $\hbar k_i$ interact with elementary quanta of SWs ($\hbar\omega$, $\hbar k$), known as magnons. If time invariance and translational invariance are maintained, the scattered photon experiences an increase in energy and momentum if a magnon is annihilated (anti-Stokes process). Conversely, a magnon can be created (Stokes process) through energy and momentum transfer from the photon. At finite temperatures ($T \gg \hbar\omega/k_B \approx 5K$), both processes occur with about the equal probability. During the interaction between the magnon, of wave vector k and angular frequency ω, and the incident (i) and scattered (s) photons, the conservation laws of energy (frequency)

and momentum (wave vector) are upheld. These principles are mathematically represented by the following equations:

$$\omega_s = \omega_i \pm \omega \quad \text{... .... (3.7.a)}$$

$$k_s = k_i \pm k \quad \text{... .... (3.7.b)}$$

In these equations, the symbols '+' and '−' denote the anti-Stokes and Stokes shifts, respectively, while ω_i, ω_s, k_i, and k_s signify the angular frequencies and wave vectors of the incident and scattered light. Classically, the scattering process can be visualized as follows: spin-orbit coupling within the material induces a phase grating that travels at the velocity of the SW. Light is Bragg-reflected from this moving grating, and its frequency undergoes a Doppler shift corresponding to the SW frequency. For light interacting with thin films, the perpendicular wave vector component is not conserved because translational symmetry is disrupted. Thus, these equations pertain only to the in-plane wave vector component k.

In BLS, the magnon energy, approximately 10^{-4} eV, is minuscule compared to the energy of visible light photons, which is typically a few eV. As a result, the energy exchanged during the scattering process—corresponding to the magnon energy—is negligible compared to the photon's initial energy. Consequently, the wave vector of the scattered photon (k_s) remains almost identical to that of the incident photon (k_i).

Figure 3.12.(a) depicts the scattering dynamics of a bulk magnon interacting with a photon, where the magnon exhibits a wave vector component perpendicular to the material surface. The scattered photon's wave vector (k_s) is constrained within a dashed circular boundary, its radius corresponding to the wave vector (k_i) of the incident photon. The conical shape in the illustration represents the scattering beam's collection angle during the Brillouin light scattering (BLS) experiment, with its axis aligned along the incident photon's wave vector. In the backscattering geometry, where $k_s = -k_i$, the magnitude of the bulk magnon's wave vector $|k|$ is precisely twice that of the incident photon's wave vector ($2|k_i|$).

Alternatively, the depiction of a photon scattering off a surface magnon is presented in Fig. 3.12 (b). In this scenario, with the momentum direction, $\boldsymbol{k}$, confined to the horizontal plane, momentum conservation occurs solely within the plane parallel to the sample surface. Put differently, the conserved portion of the incident beam equals $|k_i|sin\theta$, where θ represents the

angle between k_i and the sample surface. Consequently, the wave vector of the magnon examined in this case can be expressed as: $|\vec{q}| = |\vec{k}_i \sin\theta - \vec{k}_s \sin\theta| = 2|k_i| \sin\theta$ (3.8)

This analysis suggests that varying the angle of incidence fails to provide new perspectives on bulk magnons. However, surface magnons reveal the vital relationship between frequency and wave vector dispersion. The mathematical framework is encapsulated in Equation 3.8, commonly known as Bragg's condition, which serves as a reliable approximation for the majority of light scattering experiments. By modulating either the wavelength λ or the angle θ, the magnitude of the wave vector ($\boldsymbol{k}$) can be finely tuned in accordance with the principles outlined in Equation 3.8.

3.3.1.2. Uncertainty regarding the selected SW wave-vector

Due to the constrained aperture angle of the objective lens used for focusing and collecting light from the sample, an inherent uncertainty arises in the determination of the selected SW wave vector. When the angle of incidence θ is finite, this results in a distribution of wave vectors, which can be described as:

$$\Delta k = 2k_i \cos\theta \sin\frac{\phi}{2} = 4\frac{\pi}{\lambda} NA \cos\theta \quad \ldots \ldots (3.9)$$

Here, ϕ represents the collection angle of the lens, and NA = sin(ϕ/2) denotes its numerical aperture. This uncertainty is most pronounced when the incidence angle is normal (θ = 0°). It is worth noting that there could also be a potential uncertainty in θ resulting from the focusing of the incident beam. However, in practical experiments, this is mitigated by employing a very narrow beam (with a width of ~50 μm), which consequently enlarges the size of the focused spot.

3.3.1.3. Polarization of scattered beam:

To comprehend the light scattering phenomenon from SWs, it is essential to grasp the magneto-optic interaction occurring between incident photons and magnons. When a medium contains

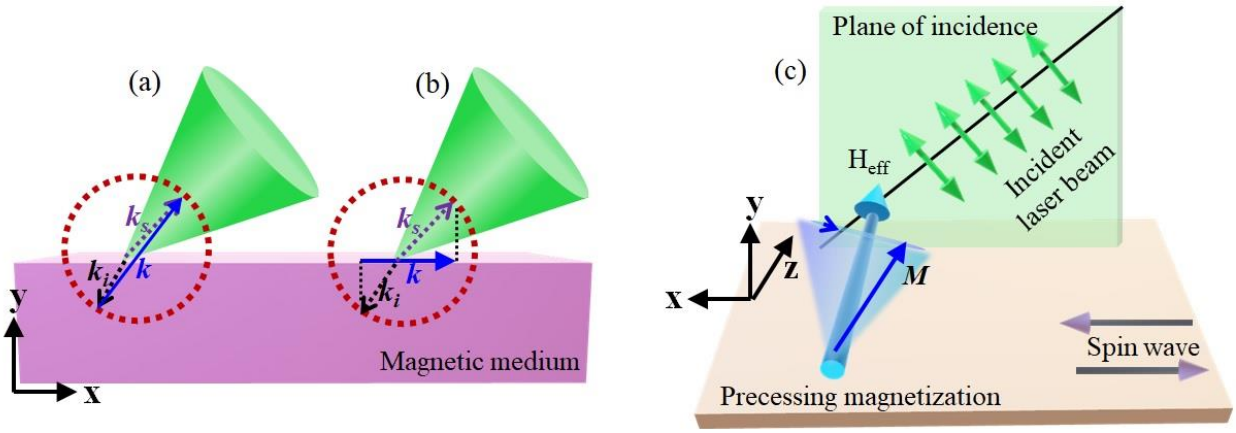

Figure 3.12. Scattering of the laser beam by (a) bulk magnon, (b) surface magnon where the direction of $\boldsymbol{k}$ corresponds to anti-Stokes process. (c) Schematic of the interaction between the p-polarized incident beam and the precessing magnetization.

precessing magnetization or SWs, it induces a spatially periodic fluctuation in polarizability due to the Lorentz force acting on oscillating electric dipoles. As a result, this interaction prompts the emission of a scattered electromagnetic wave, with its electric field vector oriented perpendicular to that of the incoming wave. In the linear response regime, when a magnetic material is subjected to an external optical electric field, it generates an electric polarization, $\boldsymbol{P}$, that is directly proportional to the applied electric field, $\boldsymbol{E}$. The relationship between $\boldsymbol{P}$ and $\boldsymbol{E}$ in this linear response regime [27] can be expressed as:

$$4\pi\boldsymbol{P} = (\epsilon_{11} - 1)\boldsymbol{E} + \frac{K}{M_S}(\boldsymbol{E} \times \boldsymbol{m}) \qquad \ldots\ldots (3.10)$$

with saturation magnetization M_S, frequency-dependent complex coefficients ϵ_{11} (dielectric constant) and K (magneto-optic coefficient), contingent upon the specific details of the band structure, this process is delineated in Fig. 3.12.(c) for p-polarized incident light (polarization parallel to the plane of incidence) in the DE geometry.

When a monochromatic laser beam impinges on the ferromagnetic sample, its electric dipoles predominantly oscillate due to the oscillatory electric field, defined as $\vec{\boldsymbol{E}} = E_x\hat{\imath} + E_y\hat{\jmath}$. Considering the dynamic component of $\boldsymbol{M}$ denoted as $\boldsymbol{m}$, $\boldsymbol{M}$ can be represented as $\boldsymbol{M}=\boldsymbol{M_0}+\boldsymbol{m}$, where $\boldsymbol{m} = m_x\hat{\imath} + m_y\hat{\jmath}$. Subsequently, according to equation 3.10, $\boldsymbol{m}$ exerts a Lorentz force, proportional to $(\boldsymbol{E} \times \boldsymbol{m})$ on the electric dipoles, leading to the polarization direction of the scattered beam for p-polarized incident light pointing in the $\hat{k}$ direction, i.e., s-polarized

scattered beam. Similarly, for incident light with s-polarization, the scattered light is expected to be p-polarized. Consequently, the scattered light by a magnon consistently exhibits polarization perpendicular to that of the incident light. Conversely, when light is scattered by acoustic phonons, no alteration in the polarizations of the incident and scattered beams is observed. Hence, by appropriately orienting the analyzing polarizer, the phonon component of the backscattered ray is effectively eliminated in the experiment[27].

3.3.1.4. **Experimental set up**:

Generally, BLS measurements are conducted in two distinct geometries:

(i) *Forward scattering geometry*: In this configuration, the scattered light is collected subsequent to the transmission of the probing beam through a transparent sample.

(ii) *Backscattering geometry*: In this scenario, the 180° backscattered light is collected from the surface of an opaque sample. Additionally, to the extension of this geometry, the concept of BLS microscopy (micro-BLS) can be employed to map the profile of SWs in a space-, time-, and phase-resolved manner, extending the capabilities of this geometry. However, this thesis will solely concentrate on detailing the conventional backscattered geometry.

Figure 3.13 presents a schematic of the standard BLS setup. The arrangement involves several key components, including a single-mode continuous solid-state laser emitting green light with a wavelength of 532 nm, a beam splitter (BS), a half-wave plate (HWP), and a polarizing beam splitter (PBS). Additionally, the system incorporates mirrors (M), an achromatic doublet (L), an electromagnet, a polarizer (P), a focusing lens (L), and a tandem Fabry-Pérot interferometer (TFPI), which works in conjunction with a single-photon detector (D). The entire system is controlled by a computer running multi-channel analyzer software, such as GHOST or TFPDAS 4.2.

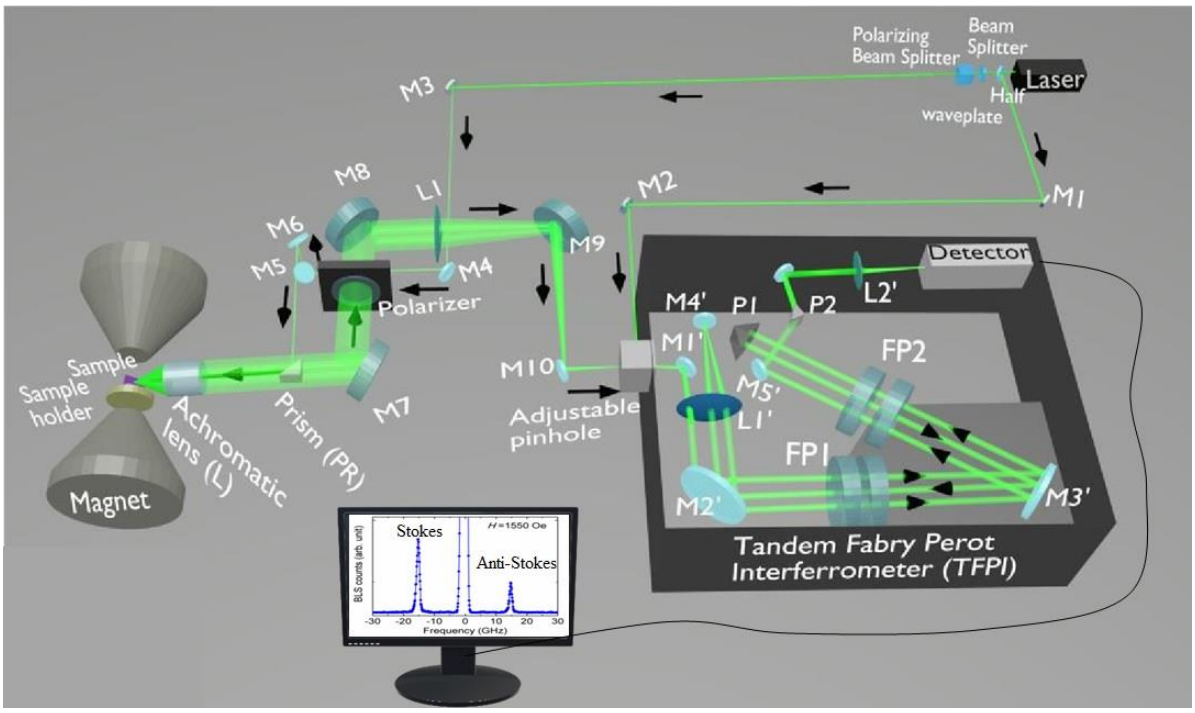

Figure 3.13. (a) Schematic diagram of the BLS setup present in our lab at SNBNCBS.

A laser beam with a power of ~230 mW and a wavelength of 532 nm is divided into two portions (1:9 ratio) using a beam splitter (BS). The 10% fraction serves as a reference beam, directed straight towards the TFPI via mirrors M1 and M2. The purpose of this reference beam is multifaceted: (i) It aids in stabilizing the mirror spacing of the FP etalons. (ii) It generates the central elastic peak in BLS spectrum, enabling the measurement of the frequency shift of the scattered beam in relation to the incident one. (iii) It assists in estimating the transmission order of the FP etalon, which is necessary for determining the frequencies SW present in the scattered beam.

To eliminate any small in-plane polarized component from the remaining 90% of the partially polarized laser beam, it undergoes polarization adjustments. Initially, the beam passes through a HWP and a PBS. Subsequently, the beam becomes perpendicular to the optical table and is guided by mirrors M3, M4, M5, M6, and the prism (PR) towards the sample. Positioned between the poles of an electromagnet at the focal length of the achromatic doublet (L) lens, the sample minimizes obstruction of the backscattered beam. This setup enables the sample's rotation on a stage in the vertical plane to adjust the angle of incidence and select different transferred SW wave vectors, as per Eq. 3.9. Measurements are conducted under a perpendicular magnetic field

to the wave vector, in the DE geometry. The scattered beam is collected by the same achromatic lens (Ach), then passes through a crossed analyzer (P) to filter out elastically scattered beam and phonon signals. Subsequently, the magnon signal is focused by lens L1 and directed towards the entrance pinhole of a (3+3)-pass TFPI for frequency analysis.

In the TFPI setup, the incident beam is first directed to mirror M1', which reflects it towards FP1 through lens L1' and mirror M2'. As the beam passes through FP1, it undergoes its initial pass (beam 1) and is subsequently reflected by mirror M3' (beam 2), continuing through FP2. After being reflected from PR1, the beam retraces its path through FP2 (beam 3) and FP1 (beam 4), ultimately reaching mirror M4'. Here, the beam is reflected once again at M4' and passes through FP1 and FP2 for the third time (beam 5 and beam 6), before it reaches the single-photon detector (D) for final detection. This multi-pass configuration is designed to amplify the contrast of the inelastically scattered light, and the data captured by the detector is stored in the computer for subsequent analysis.

3.3.1.5. Instrumentation

3.3.1.5.1. Solid state laser

We employ an extremely precise single-mode solid-state continuous wave (CW) laser with an exceptionally narrow bandwidth in our BLS set up. Throughout this doctoral research, two lasers are employed: one from 'Excelsior' and the other from 'Oxxius'. The 'Excelsior' laser delivers an output power of 230 mW, while the 'Oxxius' laser provides 220 mW, both emitting at a wavelength of 532 nm (green laser). The laser system consists of a laser head and a separate controller unit, facilitating power routing and signal monitoring between the laser head and the main system. A diode laser pumps Nd^{3+} ions within yttrium vanadate (Nd: YVO_4) crystal, emitting photons at 1064 nm. This infrared output undergoes frequency doubling via a non-linear lithium triborate (LBO) crystal, resulting in visible light at 532 nm. The emitted laser beam measures approximately 670 μm in diameter with a beam divergence of about 1.03 mrad. Overall, the laser system exhibits high reliability, maintaining steady output power and beam direction without requiring external adjustments during normal operation.

3.3.1.5.2. Pinhole and light modulator

The light modulator, depicted in Fig. 3.14. (a), consists of two shutters, SH1 and SH2, positioned behind the entrance pinhole of the TFP. These shutters alternate opening and closing to regulate

the light intensity reaching the photon detector. The detector, being highly sensitive, is at risk of damage from intense elastic light. To prevent this, the modulator works in tandem with the scanning stage. During the scanning of the elastic peak (regions I, IV, and V), P1 is blocked, and P2 remains open, permitting the reference beam to pass through. This reference beam is crucial for maintaining the stability of the angular alignment of the Fabry-Pérot interferometers (FPIs). In contrast, when scanning for Brillouin shifts (regions II and III), the roles are reversed: P2 is closed, and P1 is open, ensuring that only the necessary components of the system are active during each phase of scanning. The appropriate size of the input pinhole for a specific measurement relies on the interferometer's

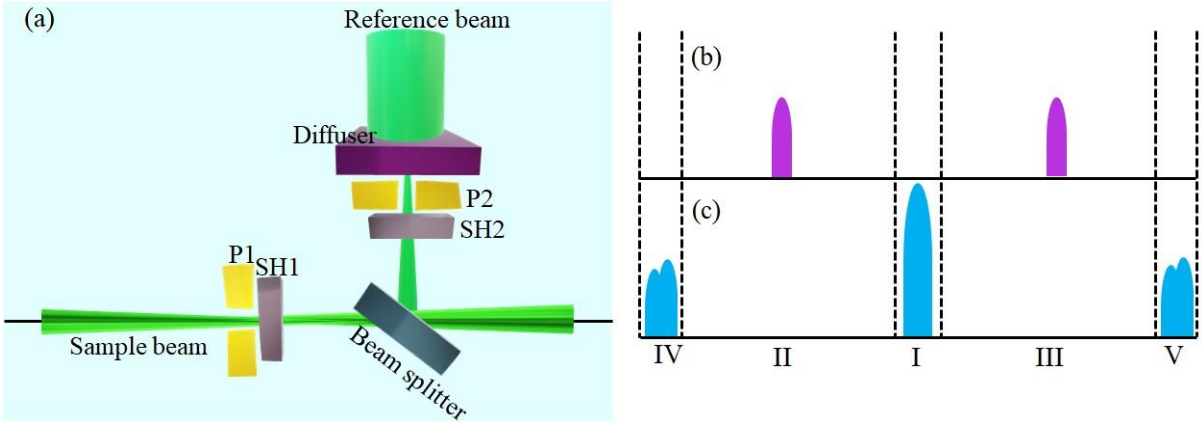

Figure 3.14. (a) Schematic diagram of the pinhole and light modulator system. A schematic of the part of the BLS spectrum which passes through (b) SH1 and (c) SH2 when another shutter remains closed. A superposition of both of the spectra is obtained when SH1 and SH2 operates in synchronization.

resolution and can be calculated using a standard formula:

$$\Omega R = 2\pi \qquad \ldots\ldots (3.11)$$

Here, Ω represents the solid angle covered by the pinhole at the input lens plane, while R indicates the resolution, expressed in finesse (F) and mirror spacing (L) as follows: $R = \frac{2FL}{\lambda} \ldots \ldots (3.12)$

3.3.1.5.3. Tandem Fabry-Pérot interferometer (TFPI)

BLS operates similarly to Raman scattering, but with frequency shifts in the GHz region compared to the THz region of Raman scattering. Observed frequency of magnon is nearly 10^{-}

^{5} times smaller than that of a typical excitation frequency of laser light. Achieving high spectral resolution for analyzing SWs is challenging due to the small cross-section of inelastic photon scattering compared to elastic scattering. To ensure efficient detection of the fractional amount of incident laser power with a high signal-to-noise ratio, high contrast is essential. This is addressed by using a (3+3) pass tandem TFPI in the BLS setup[5]. The TFPI, comprising two single FPIs connected in series, allows the light to pass through each FPI three times, enhancing spectral resolution for SW frequency analysis. The system is characterized by two main features: extensive dynamic synchronization across a wide scanning range and robust static synchronization enabled by a compact design that allows both interferometers to share the same environment. It is noteworthy that an enclosure is necessary around the interferometer to safeguard it from sound waves, which have the potential to induce high-frequency resonances within the system.

- **Fabry-Pérot interferometer (FPI)**

An etalon, or standard Fabry-Pérot interferometer (FPI), is made up of two parallel, flat mirrors that are carefully aligned and separated by a specific distance (L). As light enters the FPI, it bounces between these mirrors, reflecting multiple times. The transmitted beams overlap, and their interference results in constructive interference under normal incidence, fulfilling a particular condition, which is described as: $L = \frac{n\lambda}{2}$ … … (3.13)

Here, where n = 1, 2, 3… represents an integer (transmission order), and λ is the wavelength of light. Consequently, the consecutive interference orders are distinguished by a frequency difference Δf known as free spectral range (FSR) given by: $\Delta f = \frac{c}{2L} = \frac{150}{L}$ GHz mm^{-1}. 'c' represents the speed of light. The 'finesse' of the interferometer is associated with the FSR as expressed by: $F = \frac{\Delta F_{FSR}}{\Delta F_{FWHM}}$ … … (3.14)

Here, ΔF_{FWHM} represents the FWHM of the transmission curve. The finesse, F influences the transmitted intensity (I_t) through the FPI according to the Airy's function:

$$I_t = \frac{I_0}{1+\left(\frac{2F}{\pi}\right)^2 sin^2\frac{2\pi L}{\lambda}} \quad \text{… … (3.15)}$$

where I_0 is the intensity of the incident light. The finesse reflects instrument quality, linked to FPI's reflectivity (R) as,

$$F = \frac{\pi\sqrt{R}}{1-R} \quad \ldots\ldots (3.16)$$

Hence, greater reflectivity boosts finesse and lowers the frequency resolution, as F_{FWHM} diminishes. Conversely, with fixed R, enlarging L decreases the FSR, thus enhancing frequency resolution while finesse remains constant. The contrast of an FPI is defined as:

$$C = 1 + \frac{4R}{(1-R)^2} \quad \ldots\ldots (3.17)$$

In an n-pass interferometer, the contrast is magnified by the nth power compared to a single-pass interferometer. For example, a five-pass system can achieve a contrast that is several orders of magnitude greater—potentially five or six times higher—than what a single-pass setup can offer.

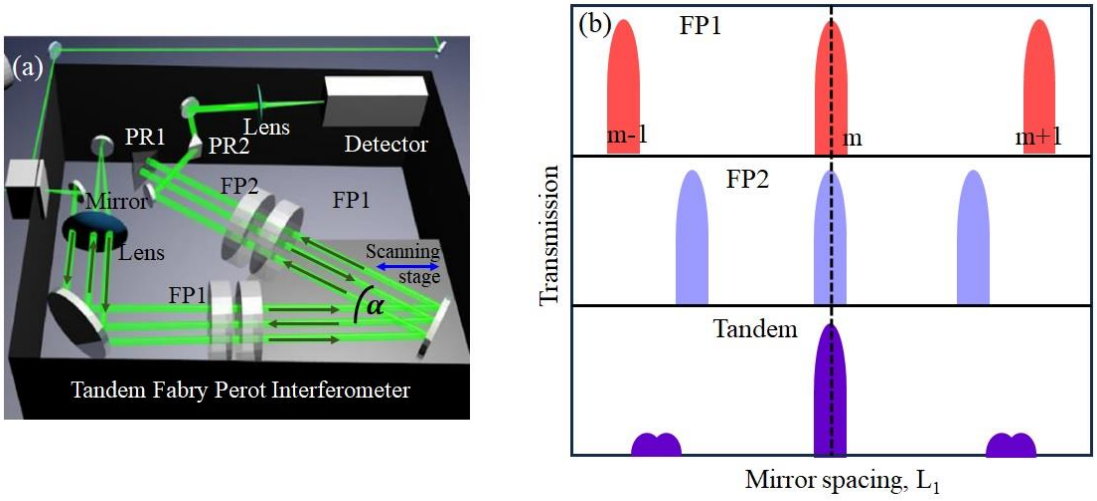

Figure 3.15. (a) Schematic diagram of the optical arrangement of TFPI. b) Transmission spectra of FP1, FP2 and in tandem operation, 'm' is the order number of the mode.

❖ Tandem operation

As the transmitted intensity depends on the mirror spacing, it exhibits periodicity with multiple passes. This periodicity introduces concerns for the FPI, particularly regarding the periodic FSR. For instance, when considering a constant mirror spacing, L and the presence of two wavelengths, λ_1 and λ_2 with transmission order m_1 and m_2, then $2L = m_1\lambda_1 = m_2\lambda_2$ … … (3.18)

When two wavelengths pass through the FPI, they may belong to different orders. However, as the second wavelength's order cannot be discerned from the reference beam, it remains indistinguishable. This makes it difficult to ascertain whether a peak signal corresponds to the Stokes side of a specific transmission order or the anti-Stokes signal of the preceding order. Hence, accurately distinguishing between these signals poses a challenge. To address these issues of identifying peak signals and determining the transmission order of wavelengths, a tandem principle is utilized. This method involves sequentially passing the light through two interferometers set at an angle α. Developed by Dr. J. R. Sandercock in 1971, this setup is illustrated in Figure 3.15.(a). Each of the two FPIs comprises two mirrors, with one mirror mounted on a translation stage and the other on an angular orientation device. The translation stage allows the right mirror of each pair to move along the optical axis of FP1. A displacement d of the translation stage results in a change of the mirror distance in FP1 by $\Delta L_1 = d$, while the change for FP2 is expressed as: $\Delta L_2 = \Delta L_1 \cos \alpha$ … … (3.19)

And the corresponding synchronization condition is given as: $\frac{\delta L_2}{\delta L_1} = \frac{\Delta L_2}{\Delta L_1}$ … … (3.20)

Now, it can prevent the mixing of different orders by adjusting the transmission of each FPI independently before scanning the linear stage. Although the two FPIs have distinct transmission orders, together they provide a central transmission order that can be adjusted by modifying the mirror spacing of FP2 (as illustrated in Fig. 3.15(b)). This alteration suppresses other orders due to the differing free spectral ranges (FSR) of the two FPIs. This setup allows for an increase in the FSR of the final spectrum while maintaining the resolution. As the TFPI stage is moved, the mirror spacing of both FP1 and FP2 changes in tandem. $l_1 = L_{10} + d$, $l_2 = (L_{10} + d) \cos \alpha$ … … (3.21)

respectively, where L_{10} represents the initial mirror spacings of FP1 when $d = 0$. This approach addresses the earlier uncertainties by establishing a stable transmission order. As discussed, the light passes through each FPI three times, enhancing the overall contrast. After undergoing six passes through the FPIs, the light is directed to a photomultiplier, which measures the transmitted photons in relation to the mirror spacing, allowing for the determination of a frequency shift. To achieve this, the scanning stage continuously adjusts the distance to cover the required frequency range, while data collection occurs over a prolonged period to ensure

statistical reliability. Consequently, the resulting BLS intensity correlates with the intensity of SWs at specific frequencies[28].

3.3.2. Time resolved magneto-optical Kerr effect (TR-MOKE) technique

TR-MOKE is a sophisticated all-optical non-invasive technique for investigating ultrafast kinetics of a magnetic system with high temporal resolution. This technique relies on the MOKE principle and tailored for time-domain measurement of magnetization based on two-colour collinear pump-probe spectroscopy. The temporal window for probing can be extended from a few femtoseconds to several nanoseconds through precise control of the probe's arrival time at the sample. Thus, accurate calculation of the optical path traversed by both the pump and probe beams to reach the sample surface is imperative for this experimental technique. In our custom-built set up, the probe is set to go through a tunable path length to avail a time span of few femtoseconds to a maximum of 3.2 nanoseconds[18]. Our TR-MOKE setup works in polar MOKE geometry, quantifying variations in the out-of-plane magnetization component as a function of the relative time delay between the pump and the probe beams. Additionally, beyond assessing magnetization dynamics, this technique enables the measurement of dynamic alterations in total reflectivity, which essentially reflects the coupled response of electron and lattice dynamics within the sample.

In this thesis, we have utilized a TR-MOKE setup in collinear geometry to explore a wide range of microscopic phenomena including precessional dynamics of SWs, plasmon dynamics, acousto-plasmo-magnon dynamics of ferromagnetic nanostructures.

3.3.2.1. TR-MOKE microscope

Utilizing a collinear geometry, this arrangement can capture signals from features down to submicrometer scales. Broadly, the collinear setup includes an fs pulsed laser system, a second harmonic generator (SHG), a motorized delay stage, various guiding optics, and a detection system. The fs oscillator system comprises two laser systems, Millennia eV and Tsunami from Spectra Physics. Presented here is a concise summary of the experimental setup, data acquisition, and detection methodology.

3.3.2.1.1. Ultrafast laser system

The **Millennia eV**[29] 10S model of Spectra Physics (Newport), a diode-pumped solid-state (DPSS) laser, emits a stable s-polarized (TEM_{00}) CW green laser at 532 nm with a maximum power output of 10 W. This laser system comprises a water-cooled laser head, a 48 V DC utility unit, and controlling software. Within its optical cavity, the Millennia eV utilizes a folded cavity resonator architecture, where a diode module delivers the pump beam to a vanadate crystal. The crystal absorbs the pump beam and emits a laser at 1064 nm, which is then converted to a 532 nm green laser via frequency doubling within a non-critically phase-matched LBO crystal. The LBO crystal exhibits a smaller nonlinear coefficient[30] relative to other crystals. Nonetheless, its large acceptance angle contributes to the stability of the Millennia eV cavity, particularly in the event of minor misalignments. Advanced technology, including 'Quiet Multi-Axial Mode Doubling,' ensures stable and high-amplitude beam output by managing various parameters and minimizing noise, while an output coupler allows the green beam to exit the cavity. Control mechanisms, including feedback systems and a shutter, maintain precise power levels. The laser head is cooled by a recirculating water chiller to ensure optimal performance. A fraction of the output beam undergoes sampling via a beam splitter and photodiode to provide feedback for the diode pump system, ensuring a consistent output within ±1% of the setpoint during power mode operation. A software-controlled shutter is positioned outside the cavity enclosure. Cooling of the laser head during lasing is facilitated by a recirculating water chiller set at a constant temperature of 20°C from Polyscience. In our setup, the Millennia eV maintains a fixed output power of 8 W.

The output from the Millennia eV laser is directed into the cavity of the second laser, **Tsunami**, via a Brewster's window to generate mode-locked femtosecond laser pulses[31]. Tsunami operates as an oscillator cavity system, employing a titanium-doped sapphire (Ti:sapphire) crystal rod as the active medium and an acousto-optic modulator (AOM) for active mode locking. Laser emission originates from Ti^{3+} ions within the Ti:sapphire crystal, triggered by fluorescent transitions in the infrared spectrum (690-1080 nm) between its ^2E_g and $^2T_{2g}$ vibrational energy bands. Within the Tsunami cavity, the laser beam is reflected back and forth by a series of mirrors. The AOM, positioned along this path, transforms the CW laser into a mode-locked laser. Comprising a quartz crystal and a piezoelectric transducer, the AOM

operates by generating a radiofrequency (RF) signal to induce a sound wave within the quartz. This sound wave establishes a transient diffraction grating, causing periodic diffraction of the laser light out of the cavity, thereby increasing cavity loss. This periodic loss, occurring at twice the frequency of the RF signal, enables stable mode-locking. Upon turning off the AOM, the cavity undergoes Q-switching, transitioning from low Q (ratio of gain to loss) to high Q, resulting in a sudden increase in cavity gain. This Q-switching mechanism yields intense laser pulses with a repetition rate of 80 MHz, characterized by an intensity proportional to the number of phase-locked modes (N) and the CW laser intensity ($I_{pulse} = NI_{CW}$).

The Tsunami laser's output wavelength is adjusted using a sequence of four prisms and a tuning slit between them. Altering the slit width controls the spectral width, which in turn affects the temporal width ((related through time bandwidth product relation) of the pulsed laser. The Tsunami's output is set at 800 nm (ideal for Si photodiode sensitivity), with a pulse width of about 80 fs maintained by adjusting the spectra's full width at half maxima (FWHM) around 12 nm. This adjustment is achieved through wavelength selection and group velocity dispersion (GVD) knobs, which control the prisms' positions and the slit width. The temperature of the Ti:sapphire rod is regulated by a water chiller unit to ensure a stable output. Continuous purging of the cavity with clean, dry nitrogen gas maintains humidity levels by eliminating dust and water vapor.

3.3.2.1.2. Second harmonic generation

The SHG (Model no. 3980-4) from Spectra Physics is designed for frequency doubling which converts the one part of the Tsunami's output beam of 800 nm to a wavelength of 400 nm which is used as the pump beam in our system. The second harmonic generation is based on the nonlinearities of the optical parameters of a material[32]. The dielectric polarization of a dielectric material consists of nonlinear higher order terms besides the linear term of the electric field. The second harmonic generation which is a coherent optical process of radiation of dipoles in a material depends on the second order electric field term in the expansion of the polarization. When a dipole of a non-centrosymmetric crystal oscillates in presence of an oscillatory electric field of frequency ω, it can emit a frequency of 2ω apart from the fundamental frequency ω. Therefore, the near-IR light converts to near-UV light. Here, the SHG employed a non-linear β-barium borate (BBO) optical crystal which produces a second harmonic of the fundamental

laser pulse. The second harmonic beam becomes parallelly polarized whereas the fundamental beam remains vertically polarized. The BBO crystal outperforms the LBO crystal in terms of second-harmonic generation (SHG) conversion efficiency, and unlike LBO, it operates without the need for additional heating. SHG conversion efficiency is inversely related to the beam spot size, so a telescopic lens system is employed to optimize the beam waist. To reduce pulse broadening caused by group velocity dispersion (GVD), a thin BBO crystal is selected. This crystal is capable of phase matching across the full tunable wavelength range of 690 to 1080 nm. To safeguard the hygroscopic BBO crystal from moisture, it is housed in a cylindrical enclosure with antireflection-coated windows and filled with an index-matching fluid. The second harmonic and fundamental beam are separated by using a prism with a highly reflective coating for the fundamental beam. The second harmonic beam diffracts through a pair prism which compensates the beam shape distortion and horizontal displacement due to the SHG crystal. Finally, both the beams exit the SHG unit through two different output paths.

3.3.2.2. Experimental setup of TR-MOKE microscope

At our laboratory in the S. N. Bose National Centre for Basic Sciences (SNBNCBS), we utilize a specially designed TR-MOKE microscope that operates in a two-colour collinear pump-probe configuration under ambient conditions. A fraction of the fundamental laser beam beam (λ_{probe} = 800 nm, fluence = 2 mJ cm^{-2}, pulse width = 80 fs) from a mode-locked Ti-sapphire laser (Tsunami, Spectra-Physics) is employed to measure the polar Kerr rotation, termed the probe beam. The pump beam, which is the frequency-doubled counterpart of the probe (λ_{pump} = 400 nm, fluence = 16 mJ cm^{-2}, pulse width = 100 fs), is used to induce magnetization dynamics in the sample.

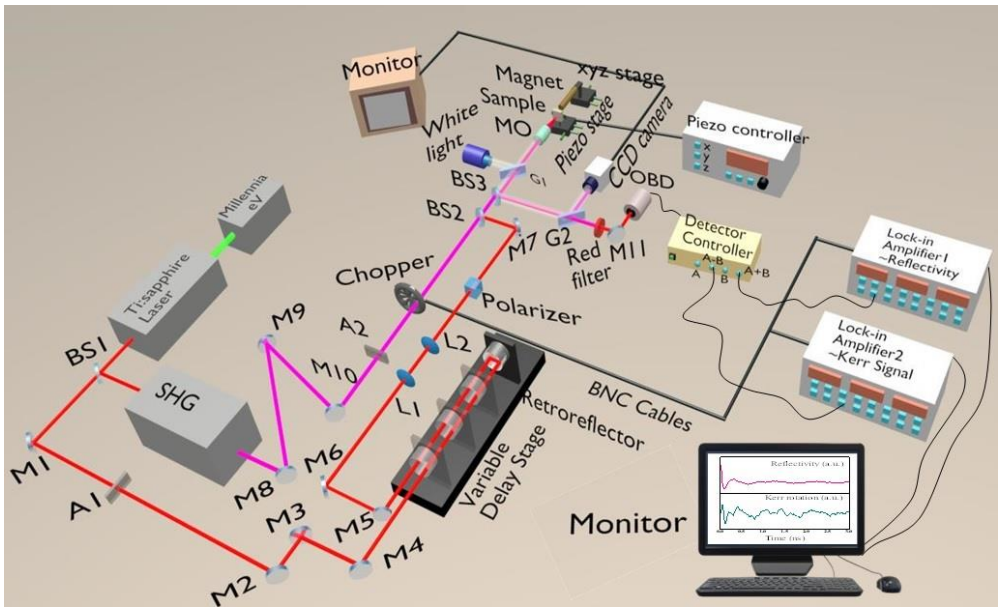

Figure 3.16. Schematic diagram of the collinear TR-MOKE microscope set up present in our laboratory at SNBNCBS

The output from the Tsunami laser is initially divided into a 70:30 ratio by a beam splitter (BS1). The intense part goes through the SHG to generate the pump beam, directed towards the sample via steering mirrors. The residual part is attenuated using a variable attenuator (A1) and is used as the probe beam, which travels along a fixed optical path, guided by four mirrors (M1, M2, M3, and M4), towards a retroreflector (RR) situated on a motorized delay stage. The position of the RR can be finely tuned through a motorized delay stage, which alters the optical path length. This modification introduces a precise optical path difference between the pump and probe beams, directly influencing the time delay applied during the experiment. The reflected 800 nm beam is then directed by two mirrors (M5 and M6) in a straight path, passing through a collimating lens assembly (L1 and L2). After collimation, the beam passes through a Glan-Thompson polarizer to ensure high degree (100,000:1) of linear polarization. Subsequently, the beam's path is rotated by a mirror (M7) to align it with the pump beam. The pump beam, along with the probe beam, is directed to a microscope objective (MO: M-40X, N.A. = 0.65) using three mirrors (M8, M9, and M10), with its power attenuated by A2. Both beams converge at a 50:50 beam splitter (referred to as the beam combiner) and enter the microscope objective (MO). The MO focuses the probe beam onto the sample surface, resulting in a spot diameter of approximately 800 nm, while the pump beam becomes slightly defocused with a spot diameter of around 1000 nm due to chromatic aberration. After interacting with the sample, the beams

reflect back through the MO and follow their incident paths. Another beam splitter (BS2) separates the reflected beams from the incident beams, guiding them along different paths. The probe beam is filtered using an infrared bandpass filter (red filter) and directed to an OBD for detection of reflectivity and Kerr rotation. Additionally, a viewing setup is established using two glass slides (G1 and G2) and a CCD camera, illuminated by a white light source to capture images of the sample surface.

A permanent magnet, mounted on a translational x-y-z stage, applies a magnetic field to the sample, while the sample is securely held in place by a motorized piezoelectric (x-y-z) stage, allowing precise scanning at the nanometer scale in both horizontal and vertical directions. To observe precessional dynamics, the magnetic field is intentionally tilted slightly relative to the anisotropy direction, generating a finite demagnetizing field along the pump direction. The intense pump beam can then dislodge the magnetization from its equilibrium position, inducing precessional motion around an effective field direction. At each measurement time step, the Kerr rotation associated with the magnetization's z-component is analyzed by the OBD, similar to the static-MOKE setup. However, here, two separate lock-in amplifiers are employed to simultaneously measure Kerr rotation (A-B) and total reflectivity (A+B) data from the electric signals generated by the OBD. A mechanical chopper modulates the pump beam at a frequency of 2 kHz to produce a reference signal for both lock-in amplifiers. To express Kerr rotation in terms of angle and maximize its measurement, the OBD undergoes calibration, and the A-B signal is adjusted to zero before the pump beam interacts with the sample.

❖ Routine alignments during experiment

Ensuring precise alignment of the pump and probe beams is crucial for the effectiveness of our TR-MOKE microscope. To achieve this, we conduct regular alignment procedures:

1. *Optimizing Tsunami output*: We maximize the power output of the Tsunami laser using external micrometer controllers, while simultaneously adjusting the spectrum to achieve the desired central wavelength ($\lambda_{probe} = 800 \pm 2$ nm) and FWHM of approximately 12 nm.
2. *RR alignment check*: We verify the alignment of the RR by observing the beam position after reflection by moving the delay stage between its two ends. Any movement of the beam in this process is corrected by adjusting the mirrors before the RR.

3. *Pump-probe beam overlap check*: We ensure the alignment of the pump and probe beams after they are combined. Correct alignment results in both beams following the same path, known as collinear geometry.

4. *MO co-axial alignment check*: We confirm that the beams are co-axial with the MO central axis by checking their positions at the back aperture of the MO. Misalignments are corrected by adjusting mirror tilts, with fine-tuning done by monitoring beam spots on a CCD camera.

5. *OBD alignment adjustment*: The alignment of the OBD is adjusted by aligning the back-reflected beam with the incident beam.

6. *Reflectivity data comparison*: Once the optical components are properly aligned, we capture time-resolved reflectivity data from a standard Silicon (Si) substrate. This allows us to compare the relaxation rate with established reference values, ensuring the pump and probe beams are correctly aligned before moving on to collect data from the magnetic sample.

3.4. Numerical Methods

Micromagnetism is a continuum-based theory that describes how magnetic properties vary across space. In micromagnetic simulations, the material is discretized into small units or cells, with each cell containing a magnetic moment. These moments interact with their neighboring cells through both short-range exchange forces and long-range dipolar interactions. The system's behavior is further influenced by anisotropy fields and external magnetic fields, with the flexibility to introduce additional field terms when necessary. Magnetization magnitude is fixed at each position but can freely rotate in 3D. Simulations use finite difference or finite element methods to discretize the sample. Solving these simulations requires iterative solutions of the Landau-Lifshitz-Gilbert (LLG) equations, often employing finite element method (FEM) or finite difference method (FDM) on cubic model geometries.

FDM utilizes a discrete lattice of points to approximate the continuous solution domain, necessitating the assignment of boundary conditions and finite difference operators. Regular grids, such as rectangular ones, are employed for spatial discretization. However, FDM may introduce artificial edge roughness, particularly in cases of complex geometries or irregular microstructures, due to its inherent limitations in representing curved boundaries accurately.

FEM discretizes the model into finite elements, with element shape—such as triangles, squares, rectangles in 2D, and tetrahedra, hexahedra, or cubes in 3D—determining problem representation. FEM facilitates the construction of complex geometries seamlessly. Nonetheless, FEM is computationally slower compared to FDM. Consequently, for larger-scale problems, FDM is often preferred due to its efficiency and practicality[33].

Examples of FEM based simulators include NMAG [34], MicroMagnum [35], TetraMag [36], COMSOL[37] etc. Conversely, Finite Difference Method (FDM) based simulators encompass Object Oriented Micromagnetic Frameworks (OOMMF)[38] , LLG micromagnetic simulator[39], MicroMagus[40, 41], MuMax3[42], Boris[43], and more. Micromagnetic simulations are applicable for timescales greater than 1 ps and length scales exceeding the atomic scale[41]. In this thesis, we employed FDM based OOMMF and MuMax3 softwares. Additionally, we utilized a custom-built DotMag software to analyze SW mode profiles utilizing dynamic output files from the micromagnetic simulators. Further descriptions of these software packages are provided below.

3.4.1. OOMMF

Developed by M. J. Donahue and D. G. Porter[38] at the National Institute of Standards and Technology (NIST) in 1999, the object oriented micromagnetic frameworks (OOMMF) software is a versatile tool for micromagnetic simulations. Its core is coded in C++ and TCL/Tk, ensuring cross-platform compatibility with Unix, Windows, and Mac OS systems. OOMMF utilizes an ordinary differential equation solver to relax spins on a quasi-two-dimensional mesh of square cells.

At the onset of simulation, users define input parameters such as anisotropy, applied field, saturation magnetization, exchange stiffness constant, damping, gyromagnetic ratio, sample structure, and dimensions in OOMMF micromagnetic input format (MIF). The size of rectangular cells must be equal to or smaller than the material's exchange length. Magnetization in each cell is updated using either a time evolver (typically 4th order Runge-Kutta) to track LLG dynamics or an energy minimization evolver to find the local energy minima.

The simulation convergence is defined by a specific stopping criterion based on the change in magnetization over time (dm/dt). This criterion is designed such that the maximum torque,

expressed as $\left(\vec{m} \times \vec{H}\right)$ (where $\vec{m} = \frac{|\vec{M}|}{Ms}$), drops below 10^{-6} Am^{-1} at a temperature of T = 0 K, ensuring the system reaches a stable state.

To simulate magnetization dynamics, a small external perturbation is introduced. Output files in 'omf', 'ohf', or 'ovf' formats contain time-dependent magnetization components, demagnetizing fields, and energies. OOMMF includes a visualization tool (mmDisp) for displaying initial magnetization profiles and demagnetizing field profiles. It accommodates arbitrarily shaped elements composed of one or multiple magnetic materials, making it a versatile option for micromagnetic simulations.

3.4.2. MuMax3

MuMax3 stands out as an open-source, GPU-accelerated micromagnetic simulator[42] requiring a high-performance graphics card. Developed at the DyNaMat group of Prof. Van Waeyenberge at Ghent University, the software package is written in Go language and leverages CUDA C kernel for enhanced processing speed. Compatible with Unix, Windows, and Mac platforms, MuMax3 employs a Windows PowerShell interface, with progress monitoring facilitated through a web-based user interface. Output data is obtained in 'ovf' format, compatible with postprocessing and viewing tools for OOMMF. Code is written in 'mx3' or 'go' format. Sample geometry can be defined using PNG images or basic 2D/3D shapes provided by MuMax3, allowing for complex geometries through rotational, translational, and scaling functions, as well as Boolean operations (AND, OR, XOR). MuMax3 offers various Runge-Kutta methods (RK45, RK23, RK12) for solving the LLG equation, each with different convergence criteria and error estimation. The solver is defined within the code by specifying the solver number. Additionally, MuMax3 provides 'relax' and 'minimize' functions to find the energy minimum of the system, with the former aimed at closely approximating the minimum energy while preventing excitations (e.g., temperature, current, time-dependent magnetic field).

3.4.3. DotMag

In order to determine the spatial power and phase distribution associated with a specific SW mode, we utilize a custom built MATLAB code called Dotmag[44]. The power map provides insight into the spatial location of the detected mode, while the phase assists in identifying its

dispersive nature. Dotmag conducts analysis and post-processing of output files obtained from micromagnetic simulators such as OOMMF and MuMax3.

The dynamic magnetization obtained from micromagnetic simulations comprises three components, expressed as $m_i = m(x,y,z,t)$ where $i = x, y, z$. This represents a resultant oscillatory signal averaged across the simulated volume. Typically, we focus on the z-component (m_z) to extract power and phase information for various resonant modes distributed on the xy-plane at a fixed z value ($z = z_0$). This involves performing a discrete Fourier transform with respect to time using Dotmag, yielding the spatially-dependent m_z at different frequencies. The frequency resolution is determined by the total simulation time, while spatial resolution depends on the sample discretization during micromagnetic simulation.

$$\tilde{m}_{z_0}(x, y, f) = FFT[m_z(x, y, z_0, t)] \quad \ldots\ldots (3.22)$$

Then the power (in dB) and phase (in radian) associated with a particular frequency $f = f_n$ is calculated from the complex function m_z as,

$$P_{z_0}(x, y) = 20\, log_{10}\left|\tilde{m}_{z_0}(x, y, f_n)\right| \quad \ldots\ldots (3.23.a)$$

$$\phi_{z_0}(x, y) = tan^{-1}\left[\frac{Im(\tilde{m}_{z_0}(x,y,f_n)}{Re(\tilde{m}_{z_0}(x,y,f_n)}\right] \quad \ldots\ldots (3.23.b)$$

The Dotmag code runs within the MATLAB environment, generating output that includes spatially dependent power and phase diagrams across different frequencies. The frequency resolution is directly tied to the overall duration of the simulation, while the precision of the spatial resolution in the power and phase maps depends on the level of sample discretization, specifically the number of cells used in the micromagnetic model.

3.4.4. Plane wave method (PWM)

The plane wave method (PWM) is a commonly employed approach for calculating excitation spectra, such as band structures, in systems with inhomogeneous or periodic geometries. This technique finds applications across various fields, including electronics, photonics, phononics, and magnonics[45-48]. It is a straightforward approach capable of providing a comprehensive spectrum of inherent excitations for various lattice types, scattering center shapes, and periodicity dimensions. In magnonic crystals (MCs), where the internal magnetic field exhibits irregularities, PWM addresses this by combining plane waves. This manipulation effectively

transforms the LLG equation into an eigenvalue problem. Subsequently, numerical methods are employed to solve this problem, enabling the determination of eigenvalues (SW frequencies) and eigenvectors (amplitude of the dynamic magnetization component).

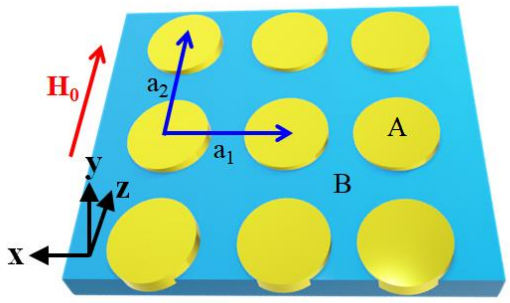

Figure 3.17. A rectangular magnonic crystal formed by circular ferromagnetic elements A embedded in matrix B with horizontal lattice constant a_1 and vertical lattice constant a_2

To calculate the spin wave spectra, we model a magnetic composite (MC) consisting of scattering centers made from ferromagnetic material A, with finite thickness, embedded in an infinite ferromagnetic matrix B. A schematic representation of this MC is shown in Figure 3.17, where circular scattering centers are arranged in a rectangular pattern, with coordinate axes indicated. The x-axis is considered perpendicular to the sample's surface, and an external bias field, H_0, is applied within the plane of the sample along the z-axis. To describe the dynamics of the magnetization vector $\boldsymbol{M}(\boldsymbol{r}, t)$, we solve the Landau–Lifshitz (LL) equation, which governs the motion of magnetization in space and time, as given by:

$$\frac{\partial \boldsymbol{M}(\boldsymbol{r},\mathrm{t})}{\partial \mathrm{t}} = -\gamma\mu_0 \boldsymbol{M}(\boldsymbol{r},t) \times \boldsymbol{H_{eff}}(\boldsymbol{r},t) \qquad \ldots\ldots (3.24)$$

Here, effective magnetic field ($\boldsymbol{H_{eff}}(\boldsymbol{r},t)$) is given by: $\boldsymbol{H}_{eff}(\boldsymbol{r},t) = \boldsymbol{H} + \boldsymbol{H}_{dem} + \boldsymbol{H}_{ex}$, …… (3.25) where the total demagnetizing field ($\boldsymbol{H}_{dem}$) can be written as: $\boldsymbol{H}_{dem} = \boldsymbol{H}_d(\boldsymbol{r}) + \boldsymbol{h}_d(r)e^{i2\pi vt}$ …(3.26)

The static $(\boldsymbol{H}_d(\boldsymbol{r}))$ and dynamic $(\boldsymbol{h}_d(\boldsymbol{r}))$ components of the dipolar field adhere to magnetostatic Maxwell's equations. The exchange field ($\boldsymbol{H}_{ex}$) is given by[49]

$$\boldsymbol{H}_{ex} = (\boldsymbol{\nabla}.l_{ex}^2(\boldsymbol{r})\boldsymbol{\nabla})m(\boldsymbol{r},t) \qquad \ldots\ldots (3.27)$$

where exchange length is $l_{ex}(r) = \sqrt{\frac{2A(r)}{\mu_0 M_s^2(r)}}$ by ignoring the contribution of anisotropy field.

In the linear approximation, the part of the magnetization vector aligned with the static magnetic field (in this case, along the z direction) remains constant over time t, and it is greater in

magnitude than the dynamic perpendicular components i.e. $\boldsymbol{M}(\boldsymbol{r}, t) = M_s(\boldsymbol{r})\hat{\boldsymbol{z}} + \boldsymbol{m}(\boldsymbol{r}, t)$ with $|\boldsymbol{m}(\boldsymbol{r},t)| \ll M_z(\boldsymbol{r})$ and $M_z \sim M_s$. So, the final form of H_{eff} can be written as:

$$\boldsymbol{H}_{eff}(\boldsymbol{r},t) = \boldsymbol{H} + \boldsymbol{H}_d(\boldsymbol{r}) + \boldsymbol{h}_d(\boldsymbol{r})e^{i2\pi\nu t} + (\boldsymbol{\nabla}.l_{ex}^2(\boldsymbol{r})\boldsymbol{\nabla})m(\boldsymbol{r},t) \quad \ldots\ldots (3.28)$$

The components of the magnetization vector $\boldsymbol{M}(\boldsymbol{r}, t)$ and the effective magnetic field $\boldsymbol{H}_{eff}(\boldsymbol{r},t)$ along the different coordinate axes are employed to compute the vector product in the Landau-Lifshitz equation. By equating this product with the corresponding terms on the left-hand side, we derive the expressions for the dynamic components of magnetization, $m_x(r)$ and $m_y(r)$, as outlined below:

$$m_x(r) = \frac{\gamma\mu_0}{i\omega}\left[m_y(r)(H + H_{ms}) - M_s h_{d,y} - M_s\nabla \cdot l_{ex}^2(r)\nabla m_y(r)\right] \quad \ldots\ldots (3.29.a)$$

$$m_y(r) = \frac{\gamma\mu_0}{i\omega}\left[-m_x(r)(H + H_{ms}) + M_s h_{d,x} - M_s\nabla \cdot l_{ex}^2(r)\nabla m_x(r)\right] \quad \ldots\ldots (3.29.b)$$

In the subsequent step, Bloch's theorem is invoked, asserting that the solution to a differential equation with periodic coefficients can be expressed as the product of plane waves and a periodic Bloch function, characterized by a lattice constant "a". This approach allows for solving the LL equation, yielding:

$$m(r) = \sum_G m_k(G)e^{i(k+G)\cdot r} \quad \ldots\ldots (3.30)$$

where $\boldsymbol{G} = (G_x, G_z) = \frac{2\pi}{a}(n_x, n_z)$ and $\boldsymbol{k} = (k_x, k_z)$ are denoted the reciprocal lattice vector of the periodic structure and the wavevector in the first Brillouin zone (BZ) respectively. In this method, all the material parameters are supposed to follow the periodicity of the lattice, i.e.

$$M_S(\boldsymbol{r} + \boldsymbol{a}) = M_S(\boldsymbol{r}),\ A_{ex}(\boldsymbol{r} + \boldsymbol{a}) = A_{ex}(\boldsymbol{r}),\ l_{ex}^2(\boldsymbol{r} + \boldsymbol{a}) = l_{ex}^2(\boldsymbol{r}) \quad \ldots\ldots (3.31)$$

In the reciprocal space, $\boldsymbol{M}_s(\boldsymbol{r})$ and $l_{ex}^2(\boldsymbol{r})$ can also be written by their Fourier transforms as follows,

$$M_S(r) = \sum_G M_s(G)e^{iG\cdot r} \quad \ldots\ldots (3.32.a)$$

$$l_{ex}^2(r) = \sum_G M_s(G)e^{iG\cdot r} \quad \ldots\ldots (3.32.b)$$

Here $M_s(G) = M_{S,A}t + M_{s,B}(1 - n)$ for G = 0 $\quad \ldots\ldots (3.33.a)$

$M_s(G) = (M_{S,A} - M_{s,B})I(G)$ for G ≠ 0 $\quad \ldots\ldots (3.33.b)$

where n is the filling fraction of magnetic material and $M_{S,A}$ and $M_{S,B}$ are saturation magnetization of two magnetic materials A and B, respectively. $I(G)$ is a function that is specific to the structure of the magnonic crystal used in this calculation.

Generally, the reciprocal lattice vector G can be calculated using the expression

$$\vec{G} = \left(m\vec{a}^* + n\vec{b}^*\right), \text{ where } \vec{a}^* = 2\pi\frac{\vec{b}\times\hat{n}}{|\vec{a}\times\vec{b}|},\ \vec{b}^* = 2\pi\frac{\hat{n}\times\vec{a}}{|\vec{a}\times\vec{b}|} \quad \ldots\ldots (3.34)$$

Where *m, n* are integers, $\vec{a}(\vec{a}^*)\ and\ \vec{b}(\vec{b}^*)$ are the lattice vectors of real (reciprocal) lattice.

For the structure under consideration, by solving the Maxwell's equation with proper boundary conditions at both surface of the slab, the magnetostatic fields can be represented as[49],

$$H_{ms,z}(r_\parallel, x) = -\sum_G \frac{M_S(G)}{G^2} G_z^2 \times \left(1 - \cosh\left(|G|x\right)e^{-\frac{|G|d}{2}}\right)e^{iG\cdot r_\parallel} \quad \ldots\ldots (3.35.\text{a})$$

$$h_{ms,y}(r_\parallel, x) = -\sum_G \frac{m_x(G)}{|q+G|^2}\left(q_y + G_y\right)^2 \times \left(1 - \cosh\left(|(q+G)|x\right)e^{-\frac{|q+G|d}{2}}\right)e^{i(q+G)\cdot r_\parallel} \quad \ldots\ldots (3.35.\text{b})$$

$$h_{ms,x}(r_\parallel, x) = -\sum_G m_x(G) \times \cosh\left(|(q+G)|x\right)e^{-\frac{|q+G|d}{2}}e^{i(q+G)\cdot r_\parallel} \quad \ldots\ldots (3.35.\text{c})$$

Here, d denotes the thickness of the slab. In the research outlined in this thesis, the aforementioned expressions are computed at x=d/2, specifically at the film's surface.

By substituting Eqs. 3.27 through 3.35 into Eq. 3.29, we can derive the dynamic magnetization components as an infinite system of equations in Fourier space.

$$\frac{i\omega}{\gamma\mu_0}m_{x,q}(\vec{G}) = Hm_{y,q}(\vec{G}) + \sum_{\vec{G}'}\frac{m_{y,q}(\vec{G})}{\left|q+\vec{G}'\right|^2}\left(q_y + \vec{G}_y'\right)^2 \times \left(1 - \cosh\left(\left|q+\vec{G}'\right|x\right)e^{-\frac{|q+\vec{G}'|d}{2}}\right)M_S(\vec{G} - \vec{G}') - \sum_{\vec{G}'}\frac{m_{y,q}(\vec{G})}{\left|\vec{G}-\vec{G}'\right|^2}\left(\vec{G}_z - \vec{G}_z'\right)^2 \times \left(1 - \cosh\left(\left|\vec{G}-\vec{G}'\right|x\right)e^{-\frac{|\vec{G}-\vec{G}'|d}{2}}\right)M_S\left(\vec{G}-\vec{G}'\right) + \sum_{\vec{G}'}\sum_{\vec{G}''}(q + G')\cdot(q+G'')l_{ex}^2(G''-G')M_S(G-G'')m_{y,q}\left(\vec{G}\right) \quad \ldots\ldots (3.36.\text{a})$$

$$\frac{i\omega}{\gamma\mu_0}m_{y,q}(\vec{G}) = -Hm_{x,q}(\vec{G}) - \sum_{\vec{G}'}m_{x,q}(\vec{G})\cosh\left(\left|q+\vec{G}'\right|x\right)M_S\left(\vec{G}-\vec{G}'\right) - \sum_{\vec{G}'}\frac{m_{x,q}(\vec{G})}{\left|\vec{G}-\vec{G}'\right|^2}\left(\vec{G}_z - \vec{G}_z'\right)^2 \times \left(1 - \cosh\left(\left|\vec{G}-\vec{G}'\right|x\right)e^{-\frac{|\vec{G}-\vec{G}'|d}{2}}\right)M_S\left(\vec{G}-\vec{G}'\right) + \sum_{\vec{G}'}\sum_{\vec{G}''}(q+G')\cdot(q+G'')l_{ex}^2(G''-G')M_S(G-G'')m_{x,q}(\vec{G}) \quad \ldots\ldots (3.36.\text{b})$$

When limiting the analysis to N reciprocal lattice vectors, the equations become finite. This results in an eigenvalue problem with eigenvalues $\frac{i2\pi f}{\gamma\mu_0 H}$ and eigenvectors $m_{x,q}(\vec{G})$ and $m_{y,q}(\vec{G})$, organized in matrix form,

$$\widehat{M}m_q = \frac{i2\pi f}{\gamma\mu_0 H}m_q \quad \ldots\ldots (3.37)$$

where the eigenvector is defined as $m_q^T = \left[m_{x,q}(G_1) \dots \dots m_{x,q}(G_N), m_{y,q}(G_1) \dots \dots . m_{y,q}(G_N)\right]$ and the corresponding matrix $\widehat{M}$ is the Bloch matrix: $\widehat{M} = \begin{pmatrix} \widehat{M}^{xx} & \widehat{M}^{xy} \\ \widehat{M}^{yx} & \widehat{M}^{yy} \end{pmatrix}$ … … (3.38)

The sub-matrices of $\widehat{M}$ are given by[48]: $\widehat{M}^{xx} = \widehat{M}^{yy} = 0$

$$\widehat{M}_{ij}^{xy} = \delta_{ij} + \sum_l \frac{(q+G_j)\cdot(q+G_l)}{H} l_{ex}^2 (G_l - G_j) M_S(G_i - G_l) + \frac{(q_y+G_{y,j})^2}{H|q+G_j|^2}\left(1 - C\left(q + G_{j,x}\right)\right) M_S(G_i - G_j) -$$

$$\frac{(G_{z,i}-G_{z,j})^2}{H|G_i-G_j|^2} M_S(G_i - G_j)\left(1 - C(G_i - G_j, x)\right) \quad \dots \dots (3.39.a)$$

$$\widehat{M}_{ij}^{yx} = -\delta_{ij} - \sum_l \frac{(q+G_j)\cdot(q+G_l)}{H} l_{ex}^2 (G_l - G_j) M_S(G_i - G_l) + \frac{1}{H}\left(C\left(q + G_{j,x}\right)\right) M_S(G_i - G_j) -$$

$$\frac{(G_{z,i}-G_{z,j})^2}{H|G_i-G_j|^2} M_S(G_i - G_j)\left(1 - C(G_i - G_j, x)\right) \quad \dots \dots (3.39.b)$$

The SW dispersion measured experimentally using BLS (for this thesis) typically exhibits strong concordance with PWM results. Nevertheless, the experimental BLS intensity is compared with the square of the modulus of the dynamic magnetization, as expressed by:

$$I_{BLS} \propto \left|m_q(G=0)\right|^2 \quad \dots \dots (3.40)$$

Subsequently, spatial mode profiles can be determined for a given wave vector and frequency by calculating the magnitude of the dynamic magnetization mx(r)m_x(r)mx(r) at each spatial coordinate. It is crucial to emphasize that PWM computations operate under the assumption that both the scattering centers and the matrix are composed of ferromagnetic materials. Nevertheless, in cases involving dot or antidot arrays where either the scattering centers or the matrix lacks magnetic properties, it becomes essential to assign minimal values to the material parameters. This precaution ensures the avoidance of implausible or erroneous solutions.

References

[1] J. Yang, W. Cui, Y. Li, G. Xie, N. Zhang, R. Wang, T. Hu, H. Zhang, *Applied Surface Science* **2016**, 382, 88.
[2] S. Swann, *Physics in Technology* **1988**, 19, 67.
[3] A. H. A. Ripain, Y. F. Lim, C. S. Lim, R. Zakaria, *Journal of Optics* **2023**, 52, 1258.

[4] K. Masood, M. Iqbal, M. Zakaullah, *Nuclear Instruments and Methods in Physics Research Section A: Accelerators, Spectrometers, Detectors and Associated Equipment* **2008**, 584, 9.
[5] C. Vieu, F. Carcenac, A. Pépin, Y. Chen, M. Mejias, A. Lebib, L. Manin-Ferlazzo, L. Couraud, H. Launois, *Applied Surface Science* **2000**, 164, 111.
[6] S. Pal, S. Saha, M. V. Kamalakar, A. Barman, *Nano Research* **2016**, 9, 1426.
[7] S. Pal, S. Saha, D. Polley, A. Barman, *Solid State Communications* **2011**, 151, 1994.
[8] S. Glasstone, *An Introduction to Electrochemistry*, Vol. 10 th printing, Affiliated East-West Press Pvt. Ltd., May 1942., New Delhi, INDIA **1942**.
[9] S. Fan, N. R. Chapline Mg Fau - Franklin, T. W. Franklin Nr Fau - Tombler, A. M. Tombler Tw Fau - Cassell, H. Cassell Am Fau - Dai, H. Dai.
[10] A. A. Talin, K. A. Dean, J. E. Jaskie, *Solid-State Electronics* **2001**, 45, 963.
[11] V. S. R. a. J. J. Beaudoin, *Handbook of Analytical Techniques in Concrete Science and Technology: Principles, Techniques and Applications*, Elsevier, **2000**.
[12] G. Binnig, C. F. Quate, C. Gerber, *Physical Review Letters* **1986**, 56, 930.
[13] N. Amos, R. Fernandez, R. Ikkawi, B. Lee, A. Lavrenov, A. Krichevsky, D. Litvinov, S. Khizroev, *Journal of Applied Physics* **2008**, 103, 07E732.
[14] *OPERATION MANUAL for Basic TEM, TF20: Tecnai G2 200kV TEM (FEI)* **2018**.
[15] C. V. Raman, *Current Science* **1998**, 74, 382.
[16] A. C. Ferrari, D. M. Basko, *Nature Nanotechnology* **2013**, 8, 235.
[17] S. Foner, *Review of Scientific Instruments* **1959**, 30, 548.
[18] A. Barman, J. Sinha, Springer International Publishing, 2018.
[19] J. S. Tse, *Journal of inclusion phenomena and molecular recognition in chemistry* **1994**, 17, 259.
[20] *Chinese Physics Letters* **2013**, 30, 054302.
[21] E. Courtens, J. Pelous, J. Phalippou, R. Vacher, T. Woignier, *Physical Review Letters* **1987**, 58, 128.
[22] S. Reiß, G. Burau, O. Stachs, R. Guthoff, H. Stolz, *Biomed. Opt. Express* **2011**, 2, 2144.
[23] n. Balkanski, *Light scattering in solids: proceedings of the second international conference on light scattering in solids, Paris, July 19-23, 1971*, Flammarion sciences, **1971**.
[24] R. Mock, B. Hillebrands, R. Sandercock, *Journal of Physics E: Scientific Instruments* **1987**, 20, 656.
[25] J. J. Krebs, *Applied Physics A* **1989**, 49, 513.
[26] G. G. Manuel Cardona, *Light Scattering in Solids VI: Recent Results, Including High-Tc Superconductivity*.
[27] G. G. Manuel Cardona, *Light Scattering in Solids VII: Crystal-field and magnetic excitations,* January, **2000**.

[28] T. T. S. Ltd., *TANDEM FABRY-PEROT SPECTROMETERS, TFP-1 AND TFP-2 HC, Operator manual*.
[29] C. Spectra-Physics, USA, *User's Manual, Millenia eV: Diode-Pumped, CW Visible Laser System,* **2017**.

[30] P. E. E. A. Y. A. Yariv, P. Yeh, and P. Yeh, *Optical Waves in Crystals: Propagation and Control of Laser Radiation, Wiley* **1984**.
[31] C. Spectra-Physics, USA, *User's Manual, Tsunami: Mode-locked Ti:sapphire Laser* **2002**.
[32] C. Spectra-Physics, USA, *User's Manual, Model 3980: Frequency Doubler and Pulse Selector* **2002**.
[33] S. Sundara Mahalingam, B. V. Manikandan, S. Arockiaraj, *Journal of Physics: Conference Series* **2019**, 1172, 012070.
[34] T. Fischbacher, M. Franchin, G. Bordignon, H. Fangohr, *IEEE Transactions on Magnetics* **2007**, 43, 2896.

[35] C. Abert, *The European Physical Journal B* **2019**, 92, 120.
[36] A. Kákay, E. Westphal, R. J. I. T. o. M. Hertel, **2010**, 46, 2303.
[37] *COMSOL Inc, COMSOL Multiphysics Reference Manual, version 5.3"*.
[38] M. D. a. D. G. Porter, *OOMMF User's guide, version1.0, Interagency Report NISTIR 6376; National Institute of Standard and Technology: Gaithersburg, MD, U.S.A.* **1999**.
[39] *LLG Micromagnetics Simulator,* http://llgmicro.home.mindspring.com/.
[40] *MicroMagus,* http://www.micromagus.de/home.html.
[41] S.-K. Kim, *Journal of Physics D: Applied Physics* **2010**, 43, 264004.
[42] A. Vansteenkiste, J. Leliaert, M. Dvornik, M. Helsen, F. Garcia-Sanchez, B. Van Waeyenberge, *AIP Advances* **2014**, 4, 107133.
[43] S. Lepadatu, *Journal of Applied Physics* **2020**, 128, 243902.
[44] D. Kumar, S. Ponraj, A. Barman, O. Dmytriiev, *Journal of Physics D, Applied Physics* **2012**, 45, 10.
[45] V. Laude, M. Wilm, S. Benchabane, A. Khelif, *Physical Review E* **2005**, 71, 036607.
[46] Z.-J. Yao, G.-L. Yu, Y.-S. Wang, Z.-F. Shi, *International Journal of Solids and Structures* **2009**, 46, 2571.
[47] M. Krawczyk, H. Puszkarski, *Physical Review B* **2008**, 77, 054437.
[48] M. Krawczyk, S. Mamica, M. Mruczkiewicz, J. W. Klos, S. Tacchi, M. Madami, G. Gubbiotti, G. Duerr, D. Grundler, *Journal of Physics D: Applied Physics* **2013**, 46, 495003.
[49] M. Krawczyk, M. L. Sokolovskyy, J. W. Klos, S. Mamica, *Advances in Condensed Matter Physics* **2012**, 2012, 764783.

Chapter 4

4. Spin Texture Driven Reconfigurable Magnonics in Diatomic Nanodot Arrays

4.1. Introduction

Charge based devices with a millions of field effect transistor (FET) are not appropriate to fulfil the ever-increasing demands of modern technology. To a great extension of density of storage, memory and processor units in integrated chip can face a huge challenge of thermal management in technological point of view [1]. Spin based devices offer an alternative means to minimize this problem efficiently leading to the development of research fields like spintronics [2], magnonics [3,4], spin-orbitronics [5], etc. Magnonics use magnons (quanta of spin waves (SWs)) as potential information carrier in artificially patterned periodic nanostructure. The emerging properties of SWs can be efficiently manipulated through simple and energy-effective means, such as tuning the lattice constant [6], dot size [7], magnetic material [8], shape [9], external magnetic field [10], and field-induced spin textures [11] in nanostructures.

Research in spin-texture-based magnonics has gained ample momentum owing to its potential applications in energy-efficient, on-chip communication and processing devices [1]. Understanding and control over SW dynamics in a myriad of patterned nanostructures have unraveled a wealth of information during the last couple of decades. Magnonic crystals (MCs) [12,13] are magnetic structures with periodically modulated magnetic properties with SWs acting as information carriers through them. Manipulation of SW properties by tuning geometric properties of MCs have been useful, but spin-textures provide a novel route to define on-demand MCs only by subtle variation of external magnetic or electric field or current leading towards much better energy efficiency and flexibility in MCs.

The comprehensive excitation, detection and manipulation of SW dynamics within patterned magnetic nanostructures have been at the forefront of spintronics research over recent decades. These nanostructures having periodicity in one-dimension (1D) [7,14], two-dimension (2D)

[15,16] and three-dimension (3D) [17,18], serve as a versatile platforms for investigating the propagation and dispersion of SWs.

In the past decade, extensive research has been conducted on coupled arrays of ferromagnetic nanodots [19-22]. Investigation of circular dot arrays, arranged in diverse lattice symmetries, revealed a remarkable variation in SW spectra, as documented in ref. [23]. Furthermore, the magnonic band structure in Fe circular dot arrays, as elucidated in ref. [24] unveils a distinctive band structure. Expanding the exploration, 2D bi-component magnonic crystals (BMC) comprising ferromagnetic circular nanodots partially embedded in another ferromagnetic film are subjected to both experimental studies using Brillouin light scattering (BLS) and theoretical analysis utilizing diverse techniques [8,25,26].

The dynamic response of antidots, featuring alternating antidot diameters (diatomic antidot lattice), leads to modifications in both the number of SW modes and mode profiles in comparison to homogeneous antidot lattices [27]. The intricate nonuniform distribution of the demagnetizing field between consecutive holes is proposed as a potential factor influencing SW dynamics. Also based on observed SW anisotropy[28], frequency dependent XNOR and XOR logic gates have been numerically proposed intended for integrated spin-based high-frequency nanocircuits [29-31].

An experimental study of diatomic dots arrays reveals an isotropic behavior of SW modes, attributed to the competition between dipolar coupling and magnetostatic coupling among dissimilar dots in a diatomic basis [32]. The magnetic spin texture within a nanodot emerges as a fundamental determinant of SW dynamics. Recent experimental findings introduce an efficient method for controlling the magnonic band structure in connected $Ni_{80}Fe_{20}$ (permalloy, Py hereafter) dots. Remarkably, this control is achieved through the manipulation of the magnetic spin texture, even under identical magnetic field conditions [11]. Notably, scarce literature reports exist on the modulation of SW dynamics through spin texture control.

Here, we present the development of reconfigurable magnonic band structure (MBS) and band gap by a bias-field controlled spin texture in a two-dimensional (2D) diatomic nanodot lattice with a complex double-dot unit cell made of Py nanodots in a rectangular symmetry. Motivated by previous findings, we investigated SW dispersion experimentally using BLS and validated the results theoretically via the plane wave method (PWM). Two distinct quasi spin texture

coupling regions were explored: 'leaf state–leaf state' coupling (H_1 = 1 kOe) and 'leaf state–S state' coupling (H_2 = 300 Oe obtained by reducing the field from saturated state). The interplay between magnetostatic and dipolar couplings plays a crucial role in altering the ground state spin texture, leading to significant changes in SW mode behavior. These findings pave the way for designing energy-efficient, high-speed, reconfigurable magnon waveguides using magnetic spin textures in nanomagnets.

4.2. Experimental and Theoretical Methods

4.2.1. Sample Fabrication and Characterization

A circular diatomic dot (DAD) array composed of a 25-nm-thick Py layer and spanning a total area of 500 μm×500 μm has been meticulously crafted on a self-oxidized Si [100] substrate. The array features a sophisticated double-dot unit cell, arranged on a rectangular lattice, and was fabricated using electron beam lithography (EBL) combined with electron-beam evaporation (EBE). During deposition, the chamber pressure was maintained at 2×10^{-8} Torr, while the lithography employed a beam current of 500 pA and a dose time of 1.0 μs.

Each unit cell comprises a larger dot (D_1) of approximately 470 nm in diameter and a smaller dot (D_2) measuring about 260 nm. The intra-unit spacing (s_1) between the two dots is ~35 nm, whereas the inter-unit separation (s_2) is ~170 nm. The lattice constants are defined as a = 1185 nm and b = 850 nm, as depicted in the inset of Figure 4.1(a). Deviations in the dot diameters and edge-to-edge separations were observed, with variations of up to ±5% and ±10%, respectively.

The topography of the sample is illustrated in the AFM image shown in Figure 1(b), while Figure 1(c) confirms the dot height to be approximately 25 nm. The average surface roughness of the dots, detailed in the inset of Figure 4.1(c), is measured at ~0.90 nm. Furthermore, Figure 4.1(d) presents the magnetic hysteresis loop of the DAD array, obtained through static magneto-optical Kerr effect (SMOKE) measurements at an azimuthal angle $\varphi = 0°$.

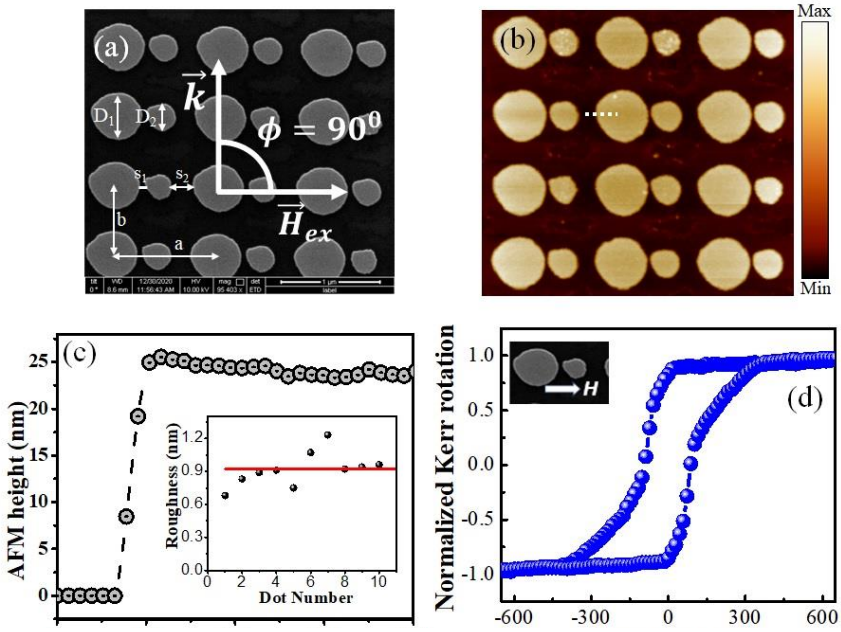

Figure 4.1: (a) Scanning electron microscope (SEM) image [the in-plane orientation (φ) of the applied bias magnetic field H is also shown] and (b) atomic force microscope (AFM) image of the DAD arrays. (c) Height of nanodot obtained from the AFM image along the dotted line in (b). Inset shows roughness of various dots in the sample. (d) Experimental hysteresis loop measured by static MOKE microscope in the indicated direction.

We have theoretically calculated the SW dispersion (frequency vs. wavevector) and spatial profiles of SW modes using the PWM [17,26]. In this approach, diatomic circular nanodots with material parameters corresponding to Py (saturation magnetization M_S = 800 kAm^{-1}, exchange constant A = 1.3×10^{-11} Jm^{-1}, g = 2.0) are considered, while negligible values of M_S and A are assigned to air gaps to avoid unphysical frequencies. A total of 450 plane waves are included to ensure convergence of the eigenvalue problem.

Here $M_s(G) = M_{S,A}t + M_{s,B}(1-n)$ for $G = 0$ … (4.1.a)

$M_s(G) = (M_{S,A} - M_{s,B})D(G)$ for $G \neq 0$ …(4.2.b)

Here, n represents the filling fraction of Py in the lattice, and $M_{S,A}$ and $M_{S,B}$ ($M_{S,B} << M_{S,A}$) correspond to the saturation magnetizations of Py and the air gap, respectively. $D(G)$ is a structure-dependent function specific to the diatomic nanodot arrangement.

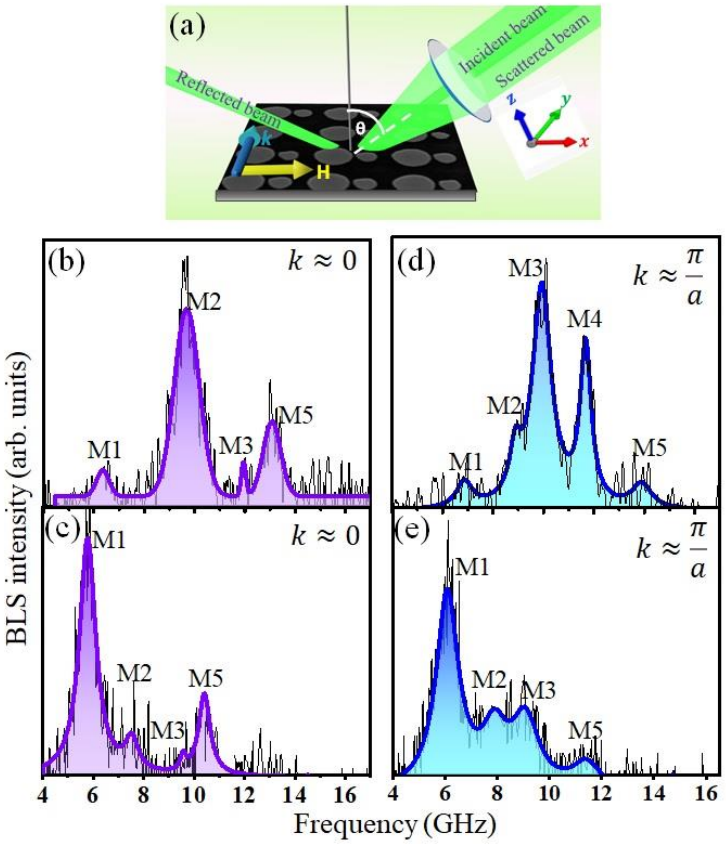

Figure 4.2: (a) Schematic of the BLS measurement in the backscattering geometry. The incident and scattered beams and the angle θ between them are shown. The Stokes side of BLS spectra at wavevector, $k \sim 0$ at (b) 1 kOe and (c) 300 Oe. The Stokes side of BLS spectra at wavevector, $k \sim \frac{\pi}{a}$ at (b) 1 kOe and (c) 300 Oe.

4.2.3. Results and Discussions

Figure 4.2.(a) schematically illustrates the experimental BLS setup in conventional backscattering geometry. To investigate the magnonic band structure of 2D magnonic crystals (MCs), it is essential to vary both the SW wave vector and its propagation direction across the sample surface. By rotating the sample in the vertical plane, the angle θ is adjusted, allowing control of the SW wave vector (k) and enabling SW dispersion measurements along the principal directions of the Brillouin zones (BZs) of the 2D MCs. In Figs. 4.2(b)-(e), we present representative BLS spectra for two magnetic states: leaf state-leaf state coupling at H_1 = 1 kOe and leaf state-C state coupling at H_2 = 330 Oe (reduced from saturation). The spectra are captured at the center of the Brillouin zone ($k \approx 0$) and at the first BZ boundary ($k \approx \pi$/a, k = 3.02 rad μm^{-1}), with coupling referring to the interaction between the spin textures of large and small dots. Our aim is to explore the tunability of the magnonic band structure through

interactions between propagating SWs and distinct spin textures. Notably, two contrasting spin textures are achieved by varying the magnetic field. At H_1 = 1 kOe, four clear peaks are observed at $k \approx 0$, and five modes at $k \approx \pi/a$. Conversely, at H_2 = 330 Oe, four peaks are well resolved at both $k \approx 0$ and $k \approx \pi/a$.

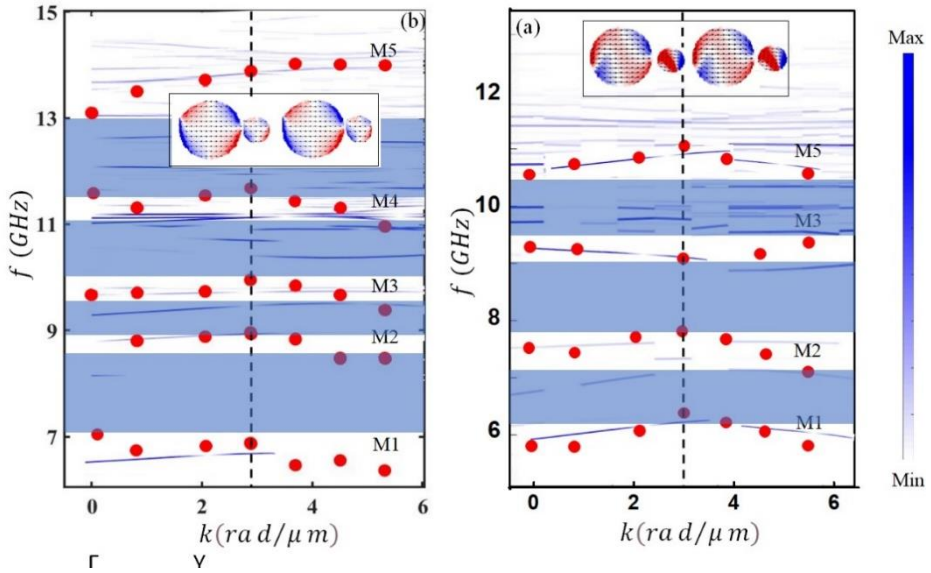

Figure 4.3: Magnonic band structure corresponding to two different bias magnetic field values: (a) H_1 = 1000 Oe (leaf state - leaf state coupling, simulated ground state is shown in the inset) and (b) H_2 = 300 Oe (leaf state - C state coupling, simulated ground state is shown in the inset). Here, filled symbols represent BLS peak frequencies for different k values, the dashed vertical line is the boundary of the first BZ. The three-dimensional surface plots of the PWM calculated SW dispersion is superposed on the experimental data in (a) and (b). Shaded regions indicate the band gaps in the dispersion. The corresponding color map for (a) and (b) is shown at the right side of

The experimentally measured SW dispersion relations for the two bias fields, H_1 and H_2, are plotted in Figure 4.3 (a) and (b), respectively, as symbols. For H_1, four distinct band gaps (BGs) are observed, whereas H_2 presents a notably different behavior with three pronounced BGs of varying widths. This indicates that the internal spin texture plays a crucial role in modulating SW propagation [11], consistent with previous observations in other systems [31,32]. The calculated magnonic band structures using the PWM are presented in Fig. 4.3(a)-(b) as 3D surface plots, superimposed on the experimental dispersion data. The color map (white to blue) represents the intensity of SW modes [$I \propto |m_y(k)^2|$], highlighting the mode strength alongside the dispersion. The color scale is adjusted to emphasize only the high-intensity SW modes, shown in blue, which clearly illustrates that the calculated and experimental high-intensity modes are in strong overall agreement.

To elucidate the impact of spin texture on magnon dispersion, a deeper understanding of SW dynamics is obtained by calculating SW mode profiles using PWM, with a focus on the modulus of the x-component of the dynamic magnetization corresponding to the experimental modes. Fig. 4.4(a) shows the spatial profiles of the SW modes at $k = 0$ (center of the Brillouin zone) and $k = \pi/a$ (1st Brillouin zone boundary) for H_1. Similarly, Fig. 4.4(b) presents the mode profiles for H_2, offering a clear visualization of the SW behavior at these key points in the Brillouin zone.

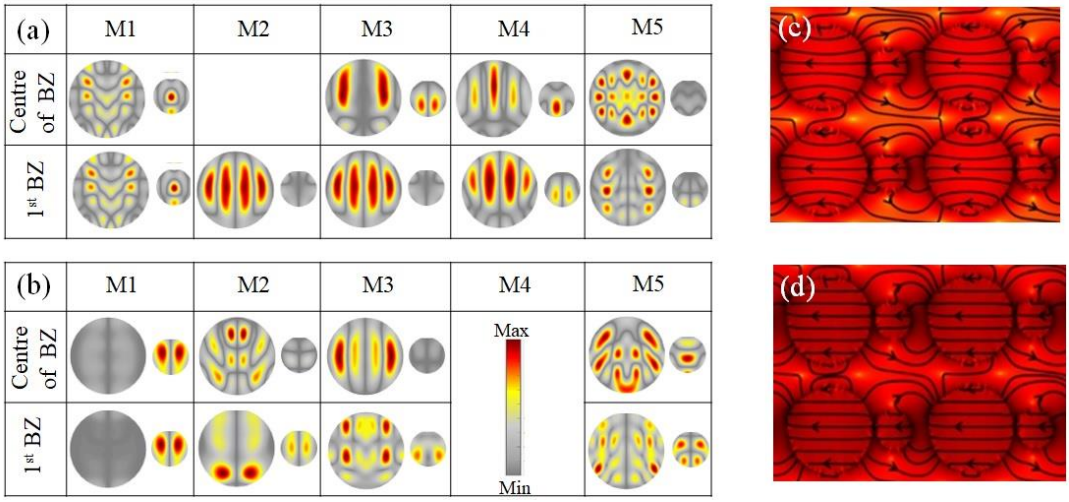

Figure 4.4: Spatial profiles of selected spin-wave modes for two different magnetic states (a) at H_1, (b) at H_2. Simulated demagnetization field distribution with spin texture coupling at two different bias magnetic field values, (c) H_1 = 1000 Oe (leaf state - leaf state coupling) and (d) H_2 = 300 Oe (leaf state - C state coupling).

At H_1, the M2 mode at $k = 0$ exhibits a hybrid backward volume (BV) and Damon-Eshbach (DE) character within the diatomic segment, which remains unchanged as k approaches π/a. At $k = \pi/a$, M2 transitions to a purely BV magnetostatic SW mode, with power localized in the larger dots. Modes M3 and M4 remain predominantly BV-like, with changes in quantization number between $k = 0$ and $k = \pi/a$, reflecting differences between the larger and smaller dots. For M3 at $k = \pi/a$, most of the power is concentrated in the larger dot. M5 shows a mixed BV-DE character at both $k = 0$ and $k = \pi/a$, with varying mode numbers, though power remains largely focused on the larger dot in the array.

At H_2, the calculated mode profile for M_1 at $k = 0$ exhibits a BV magnetostatic SW mode with an azimuthal index m = 2, where the power is concentrated primarily in the smaller dots within each diatomic segment of the array. No significant changes are observed in the spatial profile of M_1 at $k = \pi/a$. The mode M_2 at $k = 0$ displays a mixed character, combining BV and DE

components, with the power localized mainly in the larger dots. As k approaches π/a, M_2 transitions almost entirely to a BV-like mode. For modes M_3 and M_5, the profiles within the diatomic dot segment show a mixed BV-DE character at both $k = 0$ and $k = \pi$/a, with varying mode numbers, although the overall power distribution shifts across the different lobes.

A substantial increase in unsaturated magnetic spins drives this transition as the magnetic field is reduced from H_1 to H_2. This change is attributed to enhanced dynamic dipolar interactions between neighboring dots, as illustrated in Fig. 4.4(c)-(d).

4.3. Conclusions

This study demonstrates the significant role of magnetic spin textures in tuning SW dynamics within diatomic Py nanodot arrays. By systematically exploring two distinct magnetic states—'leaf state–leaf state' and 'leaf state–S state'—we reveal how subtle variations in the external magnetic field can reconfigure magnonic band structures —leading to diverse SW mode profiles and energy distributions across the nanodot array. Experimentally measured SW dispersions by BLS technique, corroborated by theoretical PWM simulations, showcase the tunable nature of SW modes and their spatial profiles. At high magnetic field (H_1), SW modes predominantly exhibit a BV character, with mode power localized in the larger nanodots. As the field is reduced (H_2), enhanced dipolar coupling between dots significantly modifies both the mode profiles and band gaps, driving transitions between BV and mixed BV-DE modes. The manipulation of the magnetic field not only alters the SW dispersion but also enhances dynamic dipolar interactions, suggesting a pathway for creating energy-efficient and high-speed magnon waveguides. These findings highlight the potential of leveraging spin textures for reconfigurable, energy-efficient magnonic devices, paving the way for future applications in on-chip communication and processing systems.

References

[1] K. Molvig, M. S. Tekula, and A. Bers, Physical Review Letters **38**, 1404 (1977).
[2] I. Žutić, J. Fabian, and S. Das Sarma, Reviews of Modern Physics **76**, 323 (2004).
[3] S. A. Nikitov, P. Tailhades, and C. S. Tsai, Journal of Magnetism and Magnetic Materials **236**, 320 (2001).
[4] V. V. Kruglyak, S. O. Demokritov, and D. Grundler, Journal of Physics D: Applied Physics **43**, 260301 (2010).
[5] A. Manchon, J. Železný, I. M. Miron, T. Jungwirth, J. Sinova, A. Thiaville, K. Garello, and P. Gambardella, Reviews of Modern Physics **91**, 035004 (2019).

[6] R. Mandal *et al.*, ACS Nano **6**, 3397 (2012).
[7] Z. K. Wang, V. L. Zhang, H. S. Lim, S. C. Ng, M. H. Kuok, S. Jain, and A. O. Adeyeye, ACS Nano **4**, 643 (2010).
[8] S. Tacchi, G. Duerr, J. W. Klos, M. Madami, S. Neusser, G. Gubbiotti, G. Carlotti, M. Krawczyk, and D. Grundler, Physical Review Letters **109**, 137202 (2012).
[9] A. Barman, S. Mondal, S. Sahoo, and A. De, Journal of Applied Physics **128**, 170901 (2020).
[10] C. Banerjee, S. Choudhury, J. Sinha, and A. Barman, Physical Review Applied **8**, 014036 (2017).
[11] A. K. Mondal, C. Banerjee, A. Adhikari, A. K. Chaurasiya, S. Choudhury, J. Sinha, S. Barman, and A. Barman, Physical Review B **101**, 224426 (2020).
[12] Z. K. Wang, V. L. Zhang, H. S. Lim, S. C. Ng, M. H. Kuok, S. Jain, and A. O. Adeyeye, Applied Physics Letters **94**, 083112 (2009).
[13] B. Lenk, H. Ulrichs, F. Garbs, and M. Münzenberg, Physics Reports **507**, 107 (2011).
[14] S. Saha, S. Barman, Y. Otani, and A. Barman, Nanoscale **7**, 18312 (2015).
[15] V. V. Kruglyak, A. Barman, R. J. Hicken, J. R. Childress, and J. A. Katine, Physical Review B **71**, 220409 (2005).
[16] S. Tacchi *et al.*, Physical Review B **86**, 014417 (2012).
[17] M. Krawczyk and H. Puszkarski, Physical Review B **77**, 054437 (2008).
[18] S. Sahoo, S. Mondal, G. Williams, A. May, S. Ladak, and A. Barman, Nanoscale **10**, 9981 (2018).
[19] A. Imre, G. Csaba, L. Ji, A. Orlov, G. H. Bernstein, and W. Porod, Science **311**, 205 (2006).
[20] D. Bhowmik, L. You, and S. Salahuddin, Nature Nanotechnology **9**, 59 (2014).
[21] S. Barman, A. Barman, and Y. Otani, Journal of Physics D: Applied Physics **43**, 335001 (2010).
[22] N. Hasegawa, S. Sugimoto, H. Fujimori, K. Kondou, Y. Niimi, and Y. Otani, Applied Physics Express **8**, 063005 (2015).
[23] S. Saha, R. Mandal, S. Barman, D. Kumar, B. Rana, Y. Fukuma, S. Sugimoto, Y. Otani, and A. Barman, Advanced Functional Materials **23**, 2378 (2013).
[24] F. S. Ma, H. S. Lim, Z. K. Wang, S. N. Piramanayagam, S. C. Ng, and M. H. Kuok, IEEE Transactions on Magnetics **47**, 2689 (2011).
[25] J. O. Vasseur, L. Dobrzynski, B. Djafari-Rouhani, and H. Puszkarski, Physical Review B **54**, 1043 (1996).
[26] M. Krawczyk, S. Mamica, M. Mruczkiewicz, J. W. Klos, S. Tacchi, M. Madami, G. Gubbiotti, G. Duerr, and D. Grundler, Journal of Physics D: Applied Physics **46**, 495003 (2013).
[27] J. Ding, D. Tripathy, and A. O. Adeyeye, EPL (Europhysics Letters) **98**, 16004 (2012).
[28] S. Saha, S. Barman, J. Ding, A. O. Adeyeye, and A. Barman, Applied Physics Letters **103**, 242416 (2013).
[29] D. A. Allwood, G. Xiong, C. C. Faulkner, D. Atkinson, D. Petit, and R. P. Cowburn, Science **309**, 1688 (2005).
[30] Y. Au, M. Dvornik, O. Dmytriiev, and V. V. Kruglyak, Applied Physics Letters **100**, 172408 (2012).
[31] S. Shichi, N. Kanazawa, K. Matsuda, S. Okajima, T. Hasegawa, T. Okada, T. Goto, H. Takagi, and M. Inoue, Journal of Applied Physics **117**, 17D125 (2015).

[32] A. De, C. Banerjee, A. Kumar Chaurasiya, R. Mandal, Y. Otani, R. Kumar Mitra, and A. Barman, Journal of Magnetism and Magnetic Materials **491**, 165557 (2019).

Chapter 5
5. Magnetization Dynamics in Diatomic Antidot Arrays

5.1. Introduction

The burgeoning field of magnonics has witnessed considerable advancements over the past decade into a significant domain within condensed matter physics and nanoscience[1]. It explores on-chip energy-efficient information processing and communication devices through the excitation, manipulation, and detection of SWs[2-4]. Magnetic antidot lattices (ADLs)[5], i.e., periodically perforated ferromagnetic thin films are considered to be a strong candidate for designing reconfigurable MCs. In these structures, periodic arrays of voids embedded in ferromagnetic media induce a spatial modulation of magnetic properties, allowing precise control over magnon wavelengths, even in the sub-100 nm regime, through tailored dipole-exchange interactions[6]. Early studies on ADLs revealed unique magnonic behaviors, including the excitation of nonuniform SW modes[7], pattern-induced mode splitting, field-dependent localization and anisotropic propagation of SWs[8-11]. Subsequent investigations, both experimental and computational, have focused on manipulating the magnonic band structure by varying the antidot geometry, lattice constant[12], lattice symmetry[13, 14], and external magnetic field parameters[15]. This has led to promising applications in GHz-frequency on-chip magnonic devices such as SW filters, waveguides, multiplexers[16], couplers[17], phase shifters[18], and logic circuits[19]. Recently, introducing geometric complexity into ADLs has garnered significant attention, as it enables richer and more reconfigurable spin-wave dynamics[4]. Complex lattice designs—such as quasiperiodic[20], fractals[21], and aperiodic structures—exhibit enhanced tunability in magnonic behavior. Notable examples include quasiperiodic octagonal lattices, defective honeycomb lattices[22], and artificial fractal structures, each offering novel reconfigurability in SW propagation. The periodic modulation introduced by the antidot edges not only alters SW quantization but also creates a periodically modulated internal magnetic field via the demagnetization effect[21, 23-25]. In square ADLs, this field induces coexisting localized and extended SW modes, dependent on the applied magnetic field. Furthermore, ADLs with alternating hole diameters[26] demonstrate modified resonance profiles and enhanced tunability of the coercive field[27, 28]. These effects, coupled with antidot size, shape, and density variations,

highlight the ability of ADLs to systematically engineer the magnetization reversal process—a phenomenon not yet fully understood at the nanoscale.

Here, we investigated the precessional magnetization dynamics of 2D Py antidot lattices with a double-antidot unit cell using TR-MOKE microscopy and micromagnetic simulations. The SW dynamics show a rich dependence on the strength and in-plane orientation of the external bias field, revealing mode conversion from extended to localized states. This study uncovers the opening and closing of SW propagation channels across a wide range of field angles (0° to 90°), offering key insights into the tunable behavior of the diatomic antidot (DAA) magnonic crystal.

5.2. Experimental and Theoretical Methods

5.2.1. Sample Fabrication and Characterizations

Arrays of 2D Py antidots, each spanning 250 × 250 μm^2, featuring a di-atomic basis and arranged in a square lattice symmetry, were meticulously crafted through a sequential process involving electron-beam lithography, electron-beam evaporation, and ion milling. Throughout the evaporation process, the deposition chamber maintained a base pressure of 2×10^{-8} Torr, ensuring precise fabrication conditions. Lithography was conducted with a beam current of 500 pA for a duration of 1.0 μs. The SEM images presented in Fig. 5.1 (a) and (b) showcase two distinct antidot arrays, labelled A1 and A2. A1 and A2 arrays exhibit a larger antidot diameter of ~400 nm, while

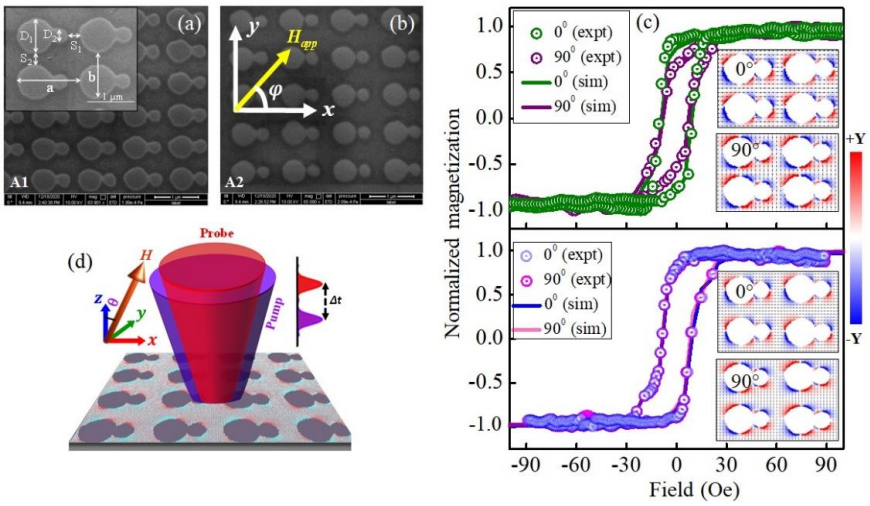

Figure 5.1: Scanning electron microscopy (SEM) images of the DAA lattices named (a) A1 (D = 200 nm) [The inset shows the SEM image of the sample with the parameters.] and (b) A2 (D = 300). (c) Experimental and simulated magnetic hysteresis loops of the samples at φ = 0° and 90° field orientations, upper and lower panel are for A1 and A2 arrays respectively. The points represent experimental data and the dashed lines are micromagnetic simulation results. Inset shows the ground state spin textures as specific configurations. (d) Schematic of the measurement geometry with collinear pump and probe beam.

they feature smaller antidots with a diameter of ~200 nm. The inter-unit separation (S_1) is about 200 nm for array I and 300 nm for array II and also S_1~S_2 for both arrays individually. The corresponding lattice constants are a~800 nm, b~600 nm for A1 and a~900 nm, b~700 nm for A2, as shown in the inset of Fig. 1(b). Notably, the diameters of the antidots exhibited a maximum deviation of ±5%, while the edge-to-edge separation between them displayed a maximum deviation of ±10%. Experimental and simulated hysteresis loops along with the ground state spin textures for both of the arrays are shown in Fig. 5.1(c).

A significant change in coercivity is observed with varying filling fractions, accompanied by distinct modifications in the shape of the experimental and simulated magnetic hysteresis loops. For the A1 array, the hysteresis loops exhibit notable differences at φ = 0° and 90° field orientations, while the two loops for the A2 array are nearly identical due to the increased inter-unit distance. These findings highlight the reconfigurability of the magnetic properties in the DAA arrays.

5.2.2. Micromagnetic Simulation

The micromagnetic simulations are performed using the OOMMF software to reproduce the experimental findings, wherein the samples are discretized into identical rectangular cuboids with dimensions of 4 × 4 × 10 nm^3. 2D periodic boundary condition (PBC) was applied to imitate the sample area used in the experiment. The length of each unit cell was below the exchange length (~5.29 nm), $l_{ex} = \sqrt{\frac{2A}{\mu_0 M_S^2}}$ of Py to incorporate the exchange interaction in the system. The material parameters used for the simulation are: saturation magnetization M_S = 850 emu cc^{-1}, anisotropy constant K = 0, gyromagnetic ratio γ = 17.6 MHz Oe^{-1}, the exchange stiffness constant $A_{ex} = 1.3 \times 10^{-11}$ J m^{-1} [2] and damping coefficient $\alpha = 0.008$[3] for dynamic simulation.

To investigate the magnetization dynamics, we first simulated the static magnetic ground state at a specific bias-field value, ensuring the system reached equilibrium by allowing sufficient relaxation time. Following this, the optical excitation was mimicked by a square pulsed field (10 ps rise time, 200 ps width and a peak amplitude of 20 Oe) perpendicular to the sample plane. The FFT of the time-resolved out-of-plane magnetization component (m_z) from the simulation provided the SW spectra.

5.2.3. Results and Discussions

The ultrafast magnetization dynamics was measured by using a home-built TR-MOKE microscope based upon a two-colour collinear pump–probe setup[29], as discussed in chapter 3. Figure 5.2(a) shows the representative background-subtracted experimental time-resolved Kerr rotation data for φ = 0° and 90° of the in-plane bias magnetic field for the two antidot arrays, A1 and A2. Subsequently FFT was applied to the time-resolved data with rectangular window function to obtain the power vs. frequency spectra of the SW modes for the two lattices. Figure 5.2(b) - (e) represents the bias field variation of frequency (*f* vs. *H*) of SW modes in the range 0.40 kOe ≤ H ≤ 1.8 kOe at $\varphi = 0°$ and 90°. A systematic variation in *f* with *H* is observed in both DAA arrays confirming purely magnetic origin of the modes.

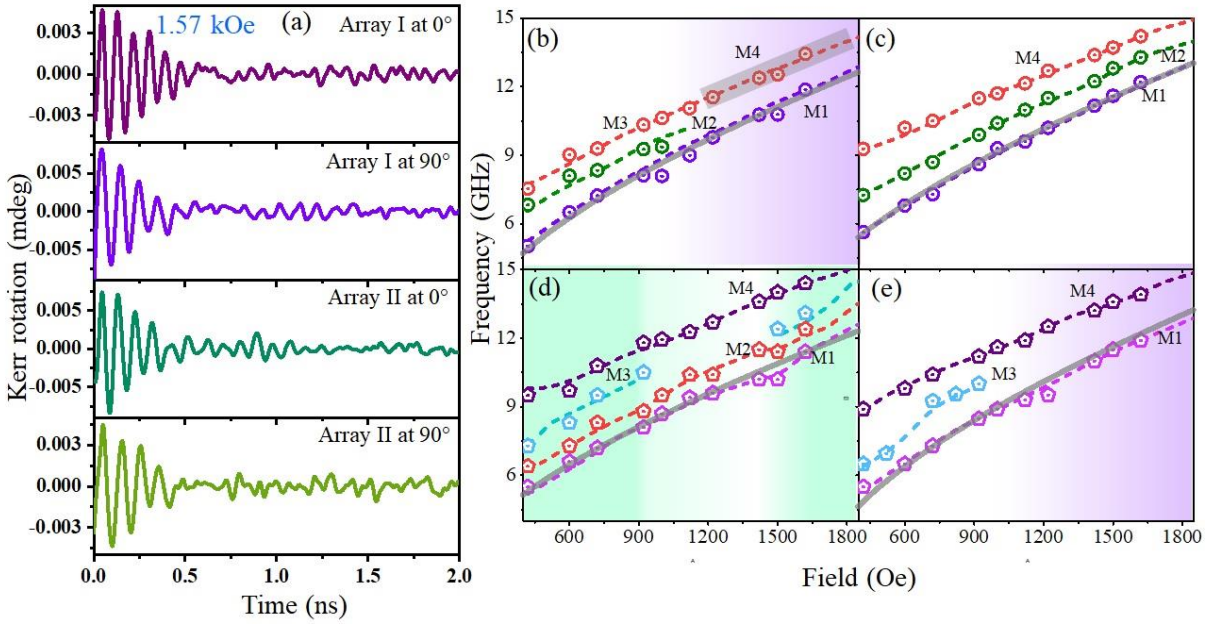

Figure 5.2: (a) Representative background subtracted time-resolved Kerr rotation showing precessional oscillations from A1 and A2 array at $\varphi = 0°$ and 90° at 1.57 kOe. (b) - (e) Bias magnetic field dependence of the observed dominant frequencies in the Kerr oscillations for (b) A1 at 0°, (c) A2 at 0°, (d) A1 at 90° and (e) A2 at 90°, The symbols represent experimental data and the solid line is Kittel fit. The dashed lines are micromagnetic simulation results.

Interestingly, mode M1 can be identified as a uniform mode both for both A1 and A2 arrays. Therefore, we fitted *f* vs. *H* for M1 with the well-known Kittel equation:

$$f = \frac{\gamma}{2\pi}\sqrt{H(H + 4\pi M_{eff})} \qquad \ldots\ldots (5.1)$$

using magneto-crystalline anisotropy field H_K = 0 and extracted the effective magnetization values (M_{eff}) as 767 emu/cc and 918 emu/cc for A1 and A2 DADL, respectively. Here M_{eff} takes care of the effects from the demagnetizing fields around the antidot and readjusts itself resulting in a significant alteration from its bulk value. To explore the impact of configurational magnetic anisotropy on SW dynamics, time-resolved precessional oscillations were measured at φ = 0° and 90° with H = 1.57 kOe. At φ = 0°, for A1 array. Three modes are observed up to ~1.1 kOe, which transform to two modes in the higher field range. In contrast, for A2 array, with larger lattice constants, three modes persist across the entire field range, indicating a distinct SW spectrum compared to A1 array. At φ = 90°, for A1 array four modes are present up to ~0.95 kOe, reappearing above 1.5 kOe. These observations suggest a significant modification in the collective magnetization dynamics as φ varies from 0° to 90°.

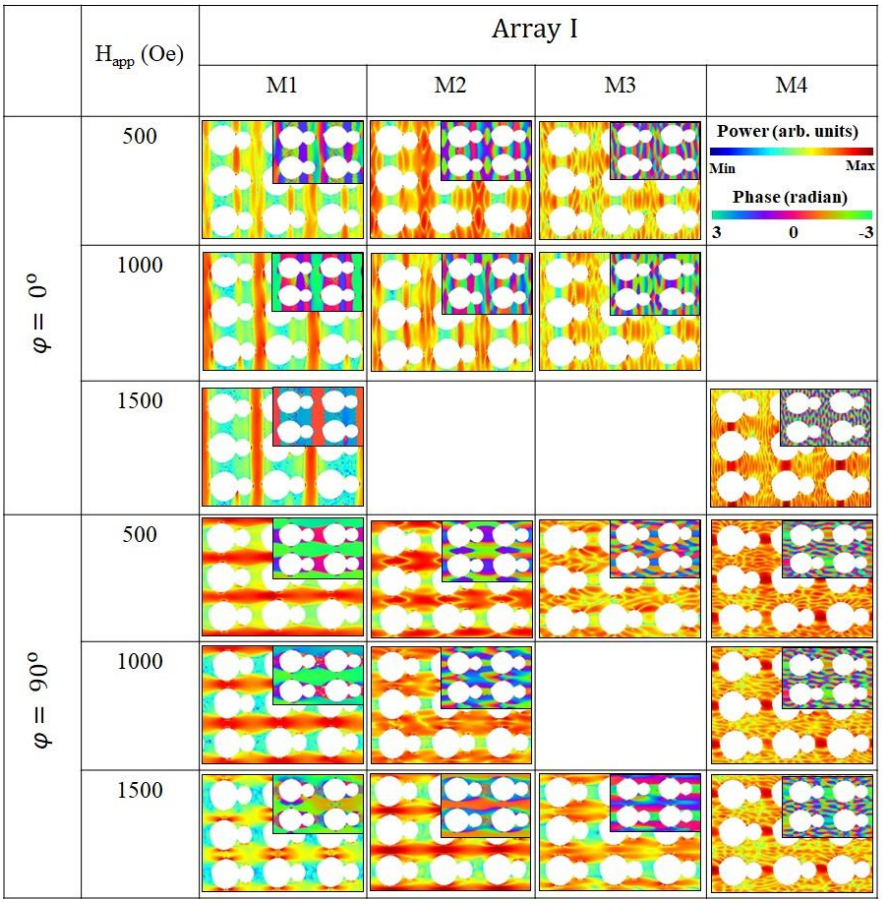

Figure 5.3: Simulated power and phase profiles of the SWs associated with the dominant frequencies M1, M2, M3 and M4 in the time-resolved Kerr rotation at three different bias fields for A1 array at φ = 0° and 90° field orientations. The colour maps are shown accordingly.

To gain deeper insights into the origin and behavior of the SW modes at different angles, spatial profiles (both power and phase) were computed using a custom MATLAB-based code called "Dotmag"[30]. The simulated power and phase maps for the DAA arrays, depicted in Figures 3 and 4 for A1 and A2 arrays, respectively, reveal the existence of distinct SW resonant modes. These include a uniformly extended mode propagating through the antidot channels, and quantized standing wave modes resulting from the modulation of the confining magnetic potential by the demagnetizing fields around the DAAs. To consistently describe the standing SW modes, we assign the quantization number '*n*' to each resonant mode confined between two neighboring basis units.

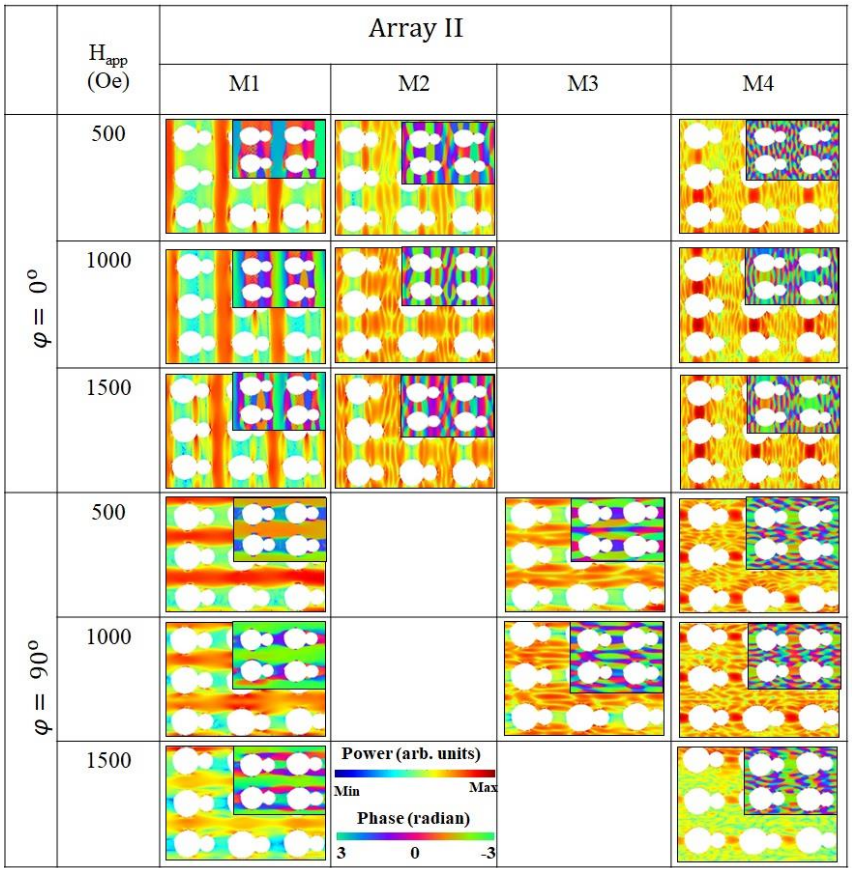

Figure 5.4: Simulated power and phase profiles of the SWs associated with the dominant frequencies M1, M2 and M4 in the Kerr oscillations at three different bias field for A2 array at φ = 0° and 90° field orientations. The colour maps are shown accordingly.

For A1 at φ = 0°, mode M1 extends along the y-direction through the Py channel, supported by dipole and exchange interactions, while forming a standing wave in the x-direction between adjacent antidots in a backward volume (BV)-like geometry. As the field increases, power in the channel rises while quantization number *n* decreases. At φ = 90°, M1 becomes localized

with reduced power concentrated at the antidot edges. At φ = 90°, mode M2 reclaims its extended nature along the x-direction, demonstrating a mode conversion with changing magnetic field orientation. At φ = 0°, M2 and M3 remain highly quantized with limited power in the vertical channel between the antidots. Above ~1.1 kOe, M2 and M3 merge to form a new mode, M4, a quantized standing wave in the BV geometry, absent at lower fields. M3 disappears in a specific field range but reappears later. These behaviors of M1 and M2 are consistent between arrays A1 and A2.

We simulated the SW spectra and power-phase profiles for both a single large dot and a small dot, as shown in Figure 5.5, revealing only two distinct modes in each case. This contrasts with the rich, multi-modal SW spectra observed in the diatomic unit cell.

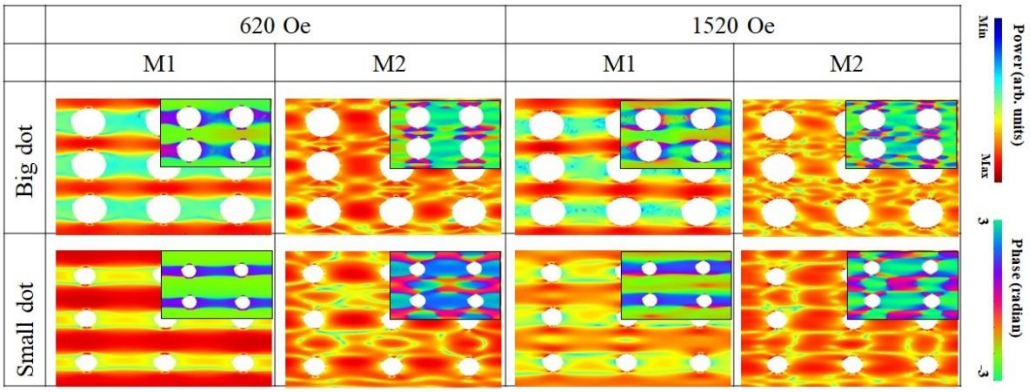

Figure 5.5: Simulated power and phase profiles of the SWs associated with the dominant frequencies M1 and M2 in the time-resolved Kerr rotations at two different bias fields for A2 array at φ = 90° field orientation considering only larger and smaller dot instead of a diatomic basis. The colour maps are shown accordingly.

Figure 5.6 provides an exemplary demonstration of how the SW propagation can be manipulated in the DADL arrays. For that, the SW response to microwave excitation is simulated for the two φ values, with same dimension, at 0° and 90°. Using OOMMF software, SWs are launched at the left end of the considered structure through a 400-nm-wide region. For excitation, we use a time-varying field of "sinc" profile (frequency window of 25 GHz) applied along the stripe axes as shown in Figure 5.6(a) and (b).

A careful observation will reveal that the SW power along the direction perpendicular to the bias field is appreciable in A2 array, while it fades away quickly in A1 array. This asserts a possible application of A2 array (larger lattice constant) as an omnidirectional emitter of SW

while A1 (smaller lattice constant) can be considered for application in SW waveguide with faster SW propagation. The spatial maps of SW also reveal that the transmission of the nodal planes at 8.9 GHz travelled over longer distance at φ = 90° in array A1 than A2 as evident from Figure 6(c) and (d). This clearly indicates, the velocity of SW is much higher in A1 as opposed to A2.

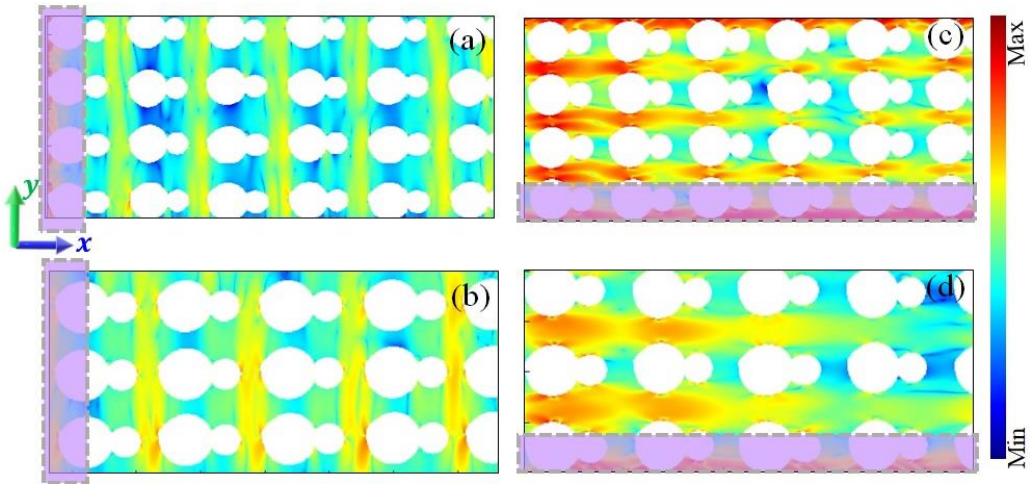

Figure 5.6: Amplitude profiles of different SW modes at 8.9 GHz excited locally at the shaded region for φ = 0° field orientation in (a) A1 array and (b) A2 array, and for φ = 90° field orientation in (c) A1 array and (d) A2 array.

5.3. Conclusions

In this chapter, we investigated the magnetization dynamics in DAA arrays using TR-MOKE microscopy and micromagnetic simulations. The results reveal a rich dependence of SW dynamics on the external bias magnetic field's strength and orientation. By varying the field angles between 0° and 90°, we observed a mode conversion between extended and localized SW states, highlighting the tunability of SW propagation channels. The two antidot arrays (A1 and A2) exhibited distinct magnetization dynamics, with A1 showing faster SW propagation and A2 demonstrating omnidirectional SW emission, making them suitable for different magnonic device applications such as magnonic waveguides and emitters. The variation in antidot size and lattice constant, coupled with field orientation, significantly influences the SW behavior, providing insights into their potential use in reconfigurable magnonic devices operating at GHz frequencies. These findings contribute to the growing understanding of antidot arrays' role in designing energy-efficient magnonic circuits.

References

[1] B. Lenk, H. Ulrichs, F. Garbs, M. Münzenberg, *Physics Reports* **2011**, 507, 107.
[2] V. V. Kruglyak, S. O. Demokritov, D. Grundler, *Journal of Physics D: Applied Physics* **2010**, 43, 260301.
[3] M. Krawczyk, D. Grundler, *Journal of Physics: Condensed Matter* **2014**, 26, 123202.
[4] A. Barman, G. Gubbiotti, S. Ladak, A. O. Adeyeye, M. Krawczyk, J. Gräfe, C. Adelmann, S. Cotofana, A. Naeemi, V. I. Vasyuchka, B. Hillebrands, S. A. Nikitov, H. Yu, D. Grundler, A. V. Sadovnikov, A. A. Grachev, S. E. Sheshukova, J. Y. Duquesne, M. Marangolo, G. Csaba, W. Porod, V. E. Demidov, S. Urazhdin, S. O. Demokritov, E. Albisetti, D. Petti, R. Bertacco, H. Schultheiss, V. V. Kruglyak, V. D. Poimanov, S. Sahoo, J. Sinha, H. Yang, M. Münzenberg, T. Moriyama, S. Mizukami, P. Landeros, R. A. Gallardo, G. Carlotti, J. V. Kim, R. L. Stamps, R. E. Camley, B. Rana, Y. Otani, W. Yu, T. Yu, G. E. W. Bauer, C. Back, G. S. Uhrig, O. V. Dobrovolskiy, B. Budinska, H. Qin, S. van Dijken, A. V. Chumak, A. Khitun, D. E. Nikonov, I. A. Young, B. W. Zingsem, M. Winklhofer, *Journal of Physics: Condensed Matter* **2021**, 33, 413001.
[5] S. A. Nikitov, P. Tailhades, C. S. Tsai, *Journal of Magnetism and Magnetic Materials* **2001**, 236, 320.
[6] C. Liu, J. Chen, T. Liu, F. Heimbach, H. Yu, Y. Xiao, J. Hu, M. Liu, H. Chang, T. Stueckler, S. Tu, Y. Zhang, Y. Zhang, P. Gao, Z. Liao, D. Yu, K. Xia, N. Lei, W. Zhao, M. Wu, *Nature Communications* **2018**, 9, 738.
[7] O. N. Martyanov, V. F. Yudanov, R. N. Lee, S. A. Nepijko, H. J. Elmers, R. Hertel, C. M. Schneider, G. Schönhense, *Physical Review B* **2007**, 75, 174429.
[8] S. Neusser, B. Botters, M. Becherer, D. Schmitt-Landsiedel, D. Grundler, *Applied Physics Letters* **2008**, 93, 122501.
[9] H. Ulrichs, B. Lenk, M. Münzenberg, *Applied Physics Letters* **2010**, 97, 092506.
[10] S. Tacchi, P. Gruszecki, M. Madami, G. Carlotti, J. W. Kłos, M. Krawczyk, A. Adeyeye, G. Gubbiotti, *Scientific Reports* **2015**, 5, 10367.
[11] S. Neusser, G. Duerr, H. G. Bauer, S. Tacchi, M. Madami, G. Woltersdorf, G. Gubbiotti, C. H. Back, D. Grundler, *Physical Review Letters* **2010**, 105, 067208.
[12] R. Mandal, S. Saha, D. Kumar, S. Barman, S. Pal, K. Das, A. K. Raychaudhuri, Y. Fukuma, Y. Otani, A. Barman, *ACS Nano* **2012**, 6, 3397.
[13] R. Mandal, S. Barman, S. Saha, Y. Otani, A. Barman, *Journal of Applied Physics* **2015**, 118, 053910.
[14] A. Manzin, O. Bottauscio, *Journal of Physics D: Applied Physics* **2012**, 45, 095001.
[15] S. Choudhury, S. Majumder, S. Barman, Y. Otani, A. Barman, *Physical Review Applied* **2018**, 10, 064044.
[16] K. Vogt, F. Y. Fradin, J. E. Pearson, T. Sebastian, S. D. Bader, B. Hillebrands, A. Hoffmann, H. Schultheiss, *Nature Communications* **2014**, 5, 3727.
[17] H. Yu, G. Duerr, R. Huber, M. Bahr, T. Schwarze, F. Brandl, D. Grundler, *Nature Communications* **2013**, 4, 2702.
[18] Y. Au, M. Dvornik, O. Dmytriiev, V. V. Kruglyak, *Applied Physics Letters* **2012**, 100, 172408.
[19] T. Schneider, A. A. Serga, B. Leven, B. Hillebrands, R. L. Stamps, M. P. Kostylev, *Applied Physics Letters* **2008**, 92, 022505.
[20] S. Choudhury, S. Barman, Y. Otani, A. Barman, *ACS Nano* **2017**, 11, 8814.
[21] Y. Y. Dai, H. Wang, T. Yang, Z. D. Zhang, *Journal of Magnetism and Magnetic Materials* **2019**, 483, 70.
[22] S. Choudhury, S. Barman, Y. Otani, A. Barman, *Journal of Magnetism and Magnetic Materials* **2019**, 489, 165408.
[23] S. Neusser, B. Botters, D. Grundler, *Physical Review B* **2008**, 78, 054406.
[24] S. Neusser, D. Grundler, *Advanced Materials* **2009**, 21, 2927.
[25] R. Zivieri, S. Tacchi, F. Montoncello, L. Giovannini, F. Nizzoli, M. Madami, G. Gubbiotti, G. Carlotti, S. Neusser, G. Duerr, D. Grundler, *Physical Review B* **2012**, 85, 012403.

[26] M. Madami, S. Tacchi, G. Gubbiotti, G. Carlotti, J. Ding, A. O. Adeyeye, J. W. Klos, M. Krawczyk, *IEEE Transactions on Magnetics* **2013**, 49, 3093.
[27] C. C. Wang, A. O. Adeyeye, N. Singh, *Nanotechnology* **2006**, 17, 1629.
[28] N. G. Deshpande, M. S. Seo, X. R. Jin, S. J. Lee, Y. P. Lee, J. Y. Rhee, K. W. Kim, *Applied Physics Letters* **2010**, 96, 122503.
[29] A. Barman, J. Sinha, Springer International Publishing, 2018.
[30] D. Kumar, S. Ponraj, A. Barman, O. Dmytriiev, *Journal of Physics D, Applied Physics* **2012**, 45, 10.

Chapter 6

6. Acousto-Plasmo-Magnonics: Coupling Spin Waves with Hybridized Phonon-Plasmon Waves in a 2D Artificial Magnonic Crystal Deposited on a Plasmonic Material

6.1 Introduction

Plasmonics is a burgeoning research domain focused on downsizing optical devices by manipulating signals at optical frequencies along nanoscale metal-dielectric interfaces, significantly below the optical wavelength [15, 16]. The evolution into magneto-plasmonics explores leveraging magnetism to amplify plasmonic properties, fostering innovations like magneto-optical nano-antennas and circuits [17-19]. While much attention has been given to the impact of magnetic fields on plasmonic properties [20, 21], the reciprocal effect, where surface plasmons, potentially hybridized with phonons, influence dynamic magnetic properties, such as spin waves in magnetic media, remains unexplored. Traditionally, plasma frequencies are orders of magnitude higher than spin wave frequencies, hindering direct strong coupling between plasmons and magnons. However, plasmons can hybridize with phonons, generating a vibrational mode comparable to spin wave frequencies in ferromagnetic media [22]. Notably, hybrid phonon-plasmon modes, observed in a monolayer system like MoS_2 [23], can magneto-elastically couple with magnon modes in magnetostrictive nanomagnets, constituting tripartite phonon-plasmon-magnon coupling. Although magnon-phonon coupling in magnetostrictive nanomagnets has been extensively studied [24, 25], experimental investigations into the coupling between hybrid phonon-plasmon modes and magnon modes are still lacking.

In this study, we employ time-resolved magneto-optical Kerr effect (TR-MOKE) microscopy to unveil the coupling between spin waves and hybridized phonon-plasmon waves, resulting in the emergence of acousto-plasmo-spin waves with a frequency comb. This phenomenon is demonstrated in a 2D artificial magnonic crystal, featuring a periodic array of ≈100 nm magnetostrictive Co nanomagnets (NMs) on a Si substrate with an intervening thin film of Al, acting as a source of surface plasmons. This unique material platform serves as an ideal testbed for investigating the intricate interplay between magnons, phonons, and plasmons.

Fig. 5(a) and (b) show the scanning electron microscope (SEM) images of two sets of samples on Si substrates respectively: (i) a two-dimensional array of elliptical Co NMs and (ii) an

identical array of NMs of the same shape and dimensions with an intervening thin film of Al of 100 nm.

6.2. Experimental and Theoretical Methods

6.2.1 Results and discussion

The FFT analysis (Fig. 6.1(f) and (g)) of the background-subtracted time-resolved reflectivity data (Fig. 6.1(d) and (e)) reveals dominant peaks at 1 and 2 GHz, independent of any bias magnetic field, indicating non-magnetic origin from both plasmonic and non-plasmonic samples.

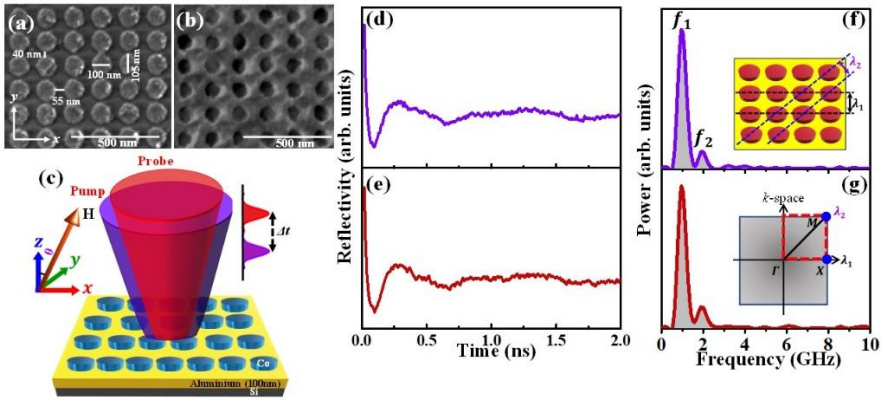

Figure 6.1. (a) and (b) SEM image of the Co nanomagnet (NM) arrays on Si substrate (non-plasmonic) and on Al evaporated on Si substrate (plasmonic) respectively. (c) Schematic of the measurement geometry. (d) and (e) Background-subtracted time-resolved data for reflectivity of non-plasmonic and plasmonic sample, respectively. (f) and (g) FFT of the respective oscillations respectively. The two detected peak frequencies correspond to modes with different periodicities in real space [inset of (f)] and reciprocal space [inset of (g)].

These oscillations arise from surface acoustic waves (SAWs) generated by the pump beam in the Si substrate due to non-uniform thermal expansion/contraction between NMs and the substrate. The 1 GHz frequency corresponds to SAWs with a wavelength λ_1, while 2 GHz corresponds to SAWs with a diagonal wavevector of wavelength λ_2. In fact, the nanomagnets act as mechanical loads and hence as reflectors of SAW, making the sample act not just as a magnonic crystal, but also a "phononic crystal".

Fig. 6.2(a) displays the Kerr oscillation data from Co nanomagnets on Si without Al, measured at various bias magnetic fields. Peaks in the FFT, as shown in Fig. 6(b), reveal spin-wave frequencies, unaffected by plasmonic coupling. Despite a low signal-to-noise ratio, three peaks

('1', '2', '3') are identified. Mode '2' fits to the Kittel formula, indicating a Kittel-like mode with an effective magnetization (M_{eff}) of 1100 emu cm^{-3}. Modes '1' and '3' deviate from Kittel behavior, likely representing an edge mode and a hybrid magneto-dynamical mode, respectively.

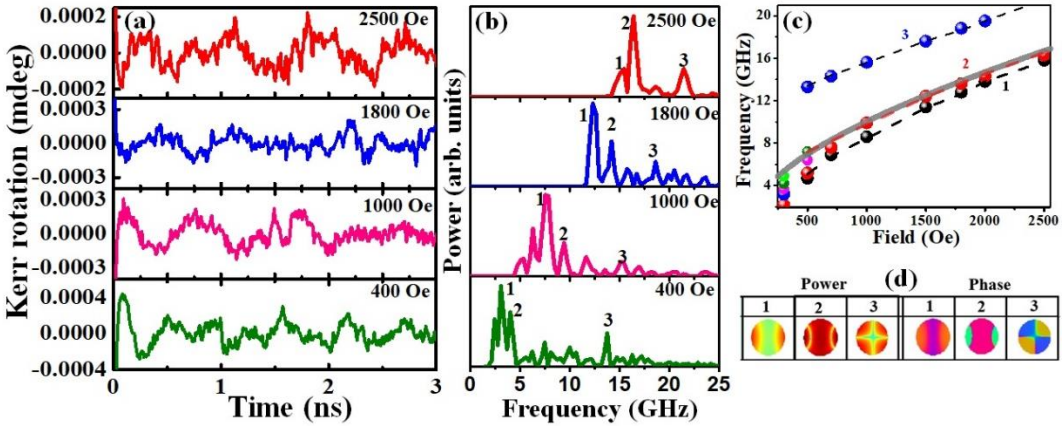

Figure 6.2. (a) Bias magnetic field dependence of the background subtracted time-resolved Kerr oscillations from non-plasmonic sample. (b) the FFT of the corresponding oscillations. (c) Bias magnetic field dependence of the observed three dominant frequencies in the Kerr oscillations. The spheres represent experimental data and the solid line is Kittel fit for mode "2" while the dashed lines are micromagnetic simulation results. (d) Simulated power and phase profiles of the spin waves associated with the three dominant frequencies M1, M2 and M3 in the Kerr oscillations at 1kOe. The power distributions of these modes do not change appreciably much with the external bias field strength showing excellent stability. The units of power and phase are arbitrary units and radians, respectively.

Unlike the Al-free sample, the Al-aided sample, featuring plasmonic coupling, displays a more complex spectrum. Four field-independent modes, forming a frequency comb at 1 GHz, 2 GHz, 3 GHz, and 4 GHz, appear alongside other field-dependent modes. These modes are exclusive to the Al layer, suggesting a plasmonic origin. The frequency comb remains stable across a broad range of bias magnetic fields, showcased in Fig. 6.3(b). Impressively, it spans two octaves, a challenging feat for optical combs. In these samples, higher-frequency field-dependent Kittel (M2) and Kittel-type modes (above 5 GHz) coexist with the field-independent acousto-plasmo-spin wave modes, as shown in Fig. 6.3(d).

We observed mode coupling between field-dependent SW modes M1 and M2 in the presence of hybrid phonon-plasmon modes with aluminum. This coupling is confirmed by a clear anti-crossing gap at a magnetic field of 170 Oe. Figure 7(b) shows the gap 2g and the loss rates (half width at half maximum) of the modes M1 and M2, which are k_1 and k_2. To extract the values of

these quantities, we fitted the peaks corresponding to M1 and M2 with a Lorentzian function. We find g = 0.53 GHz, k_1 = 0.27 GHz, and k_2 = 0.15 GHz. The cooperativity factor for coupling is defined as $C = \frac{g^2}{k_1 k_2}$, which, in our case, has a value of 6.9. Normally, strong coupling is defined as C > 1 and $g > k_1, k_2$, and satisfaction of both conditions is indicative of strong coupling in this case. In our case, there is strong tripartite coupling between phonons, plasmons, and magnons, which is suggestive of generation of a novel quasi-particle that can be called a *acousto-plasmo-spin wave (APSW) polariton*. Notably, no observable coupling occurs in the sample without Al.

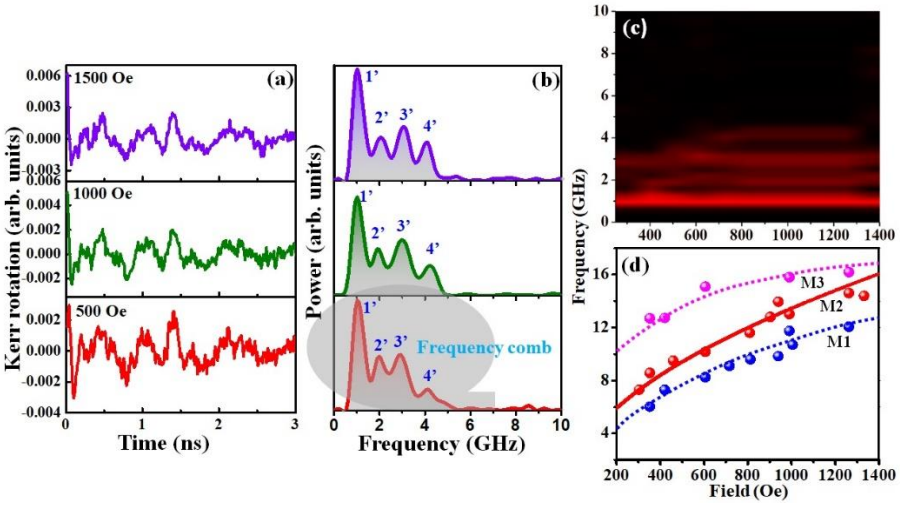

Figure 6.3. (a) Bias magnetic field dependence of the background subtracted time-resolved Kerr oscillations plasmonic samples. b) The FFT of the corresponding Kerr oscillations showing a frequency comb with four "teeth" at 1, 2, 3 and 4 GHz, spanning over two octaves. c) Surface plot of acousto-plasmo-spin wave power spectra as a function of bias magnetic field. (d) Frequencies of the field-dependent modes in the Kerr oscillations versus bias magnetic field. The spheres represent experimental data, and the solid line is Kittel fit for mode M2.

Our experiments also revealed significantly higher MOKE signal and ~200X power amplification (Fig. 8a) in the sample with aluminum compared to the sample without aluminum, indicating the presence of parametric amplification and confirming the strong coupling involved in the tripartite plasmon-phonon-magnon coupling. Here, energy is transferred from the hybridized phonon-plasmon mode to the naturally occurring SW modes to increase the amplitude and power of the resulting APSW mode.

6.3 Conclusions

We report the first observation of acousto-plasmo-spin wave modes born of tripartite non-linear coupling (with cooperativity factor far exceeding unity) resulting from the tripartite coupling of

plasmons, phonons, and magnons in a 2D artificial magnonic crystal fabricated on a plasmonic thin film. These modes exhibit a frequency comb pattern, driven by a non-linear coupling phenomenon that arises from the interaction between hybridized phonon-plasmon modes and

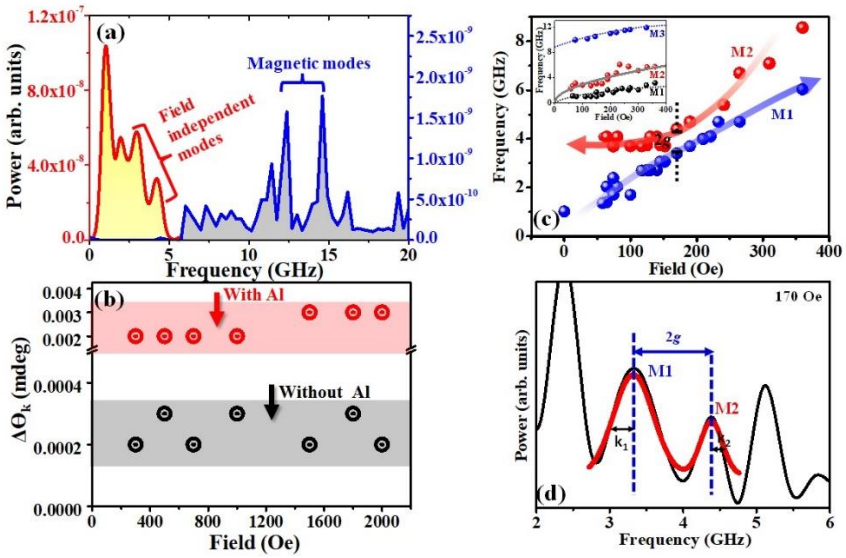

Figure 6.4. (a) Amplitude of power in FFT spectra obtained from Kerr rotation of plasmonic and non-plasmonic samples at H = 1.28 kOe. (b) Average peak-to-peak Kerr rotation amplitude (averaged over all modes) in the plasmonic sample (with Al) and in the non-plasmonic sample (without Al), as a function of the bias magnetic field. (c) Experimental bias magnetic field dependence of the frequencies of field dependent modes M1 and M2 in the magnetic field range of 0– 400 Oe in plasmonic samples. The lines with arrow heads are guide to the eye for the dispersions of the modes M1 and M2. Experimental bias magnetic field dependence of the field dependent modes 1, 2, and 3 in the magnetic field range of 0–400 Oe in non-plasmonic samples [inset of (c)]. (d) FFT power spectrum of the observed field-independent and field-dependent modes (M1 and M2) at the magnetic field of H = 170 Oe (black solid line).

spin-wave modes. Although extensive research has been conducted on optical frequency combs [26] and their applications in precision measurement and devices (atomic clocks), the utilization of spintronic frequency combs, particularly APSW frequency combs, remains unexplored in similar contexts. This tripartite coupling also produces parametric amplification whereby the APSW modes exhibit 200X power amplification arising from transfer of energy from the hybridized phonon-plasmon modes to the naturally occurring spin wave modes in the magnonic crystal. It may facilitate efficient GHz-THz frequency mixing and offers a new avenue to explore nonlinear coupling, parametric amplification, and frequency comb physics. It has potential applications as hardware accelerators in neuromorphic processors and AI systems.

Chapter 7

7. Tripartite Phonon-Magnon-Plasmon Coupling, Parametric Amplification, and Formation of a Phonon-Magnon-Plasmon Polariton in a Two-Dimensional Periodic Array of Magnetostrictive/Plasmonic Bilayered Nanodots

7.1 Introduction

In recent years, the investigation of coupling phenomena in nanostructured magnetic media has gained significant attention due to its potential applications in on-chip quantum transduction and coherent information processing as well as uncovering rich physical interactions. Building upon our previous work[27], we delve into the intriguing features arising from the tripartite coupling among three different entities - phonons, magnons and plasmons, demonstrating the formation of acousto-plasmo-magnonic frequency combs. This exploration extends the well-explored field of bipartite magnetoelastic coupling, progressing from magnon-phonon interactions to tripartite coupling involving phonons, magnons, and plasmons.

This work contributes to this evolving landscape by investigating the aforementioned tripartite coupling in a two-dimensional periodic array of bilayered Co/Al nanodots on a silicon substrate employing TR-MOKE microscopy, schematically shown in Fig. 9(c).

The samples are fabricated using e-beam lithography and sequential e-beam evaporation of various metals. An e-beam resist is applied on a Si substrate and patterned in a Raith system to create openings for nanodots. Subsequently, Ta (10 nm), Al (10 nm), Co (6 nm), and Au (2 nm) are sequentially evaporated, followed by lift-off. The Au layer serves to prevent Co oxidation. Two sets of samples, as shown in SEM images in Fig. 9(a) and (b), are fabricated on Si substrates: (i) a two-dimensional array of elliptical Co NMs and (ii) an identical array of [Co/Al] bilayered NMs. The former lacks plasmons, while the latter incorporates Al as a source of plasmon.

7.2 Results and discussion

In Fig. 9(d) and (e), we present time-resolved reflectivity data for non-plasmonic and plasmonic samples at 16 mJ/cm^2 pump fluence. In the non-plasmonic sample, FFT reveals dominant peaks at 1.5 GHz (f_1) and 2.7 GHz (f_2), attributed to bending waves induced by unequal thermal expansion of nanodots and substrate. The observed frequencies correlate with specific points in the 2D Brillouin zone.

For the plasmonic sample, FFT exhibits four peaks at 2 GHz (f_1'), 5.5 GHz (f_2'), 7.1 GHz (f_3'), and 8.6 GHz (f_4'), with f_1' dominating. A blue shift and increased linewidth in the plasmonic sample suggest a hybrid phonon-plasmon mode, where the quasi-particle is more energetic than the pure phonon (bending waves) due to energy transfer. The heightened linewidth indicates increased lossiness in the hybrid mode, potentially due to strong coupling with electromagnetic waves[28], warranting future investigations into electromagnetic wave emissions.

Fig. 10(a) presents Kerr oscillation data from plasmonic samples at varying bias magnetic fields. Despite modest signal-to-noise ratio, peaks '1', '2', and '3' are discerned in FFT spectra. Mode '2' aligns with Kittel-like behavior, fitted using the Kittel formula, displaying an effective magnetization (M_{eff}) of 1250 emu cm^{-3}. Modes '1' and '3' deviate from Kittel-like behavior, identified as the edge mode and a hybrid magneto-dynamical mode, respectively. In contrast, the plasmonic samples exhibit richer spectra, including a stable field-independent plasmonic mode at ~30.5 GHz. This mode persists regardless of magnetic field presence. Field- dependent modes M4 and M3 display a distinct gap at 820 Oe, indicating coupling mediated by the hybrid phonon-plasmon mode. Lorentzian fits reveal g = 0.78 GHz, k_1 = 0.36 GHz, and k_2 =0.35 GHz, satisfying criteria for strong coupling (C = 4.8), as already discussed in previous work.

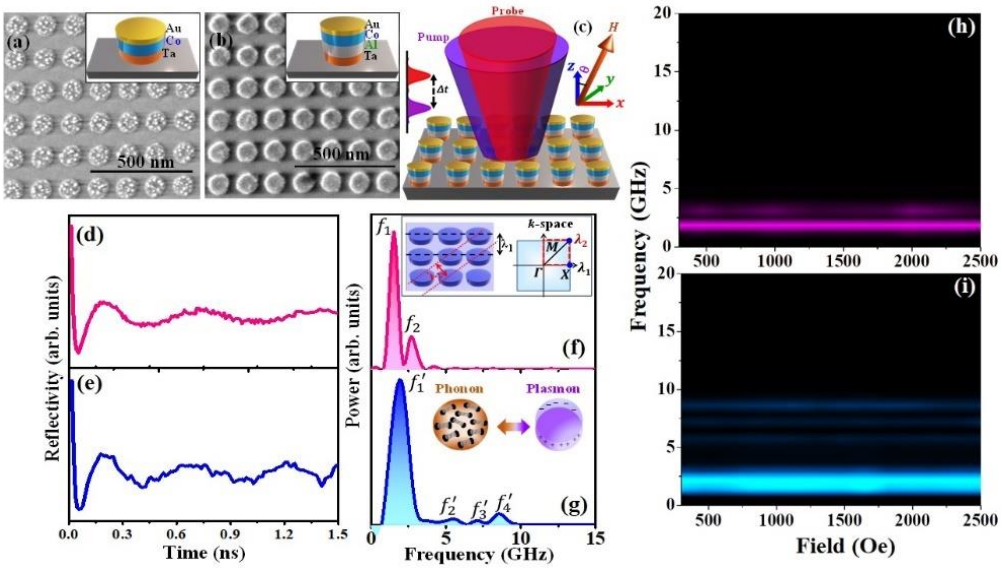

Figure 7.1. SEM images of the (a) Co NM arrays on Si substrate. (b) identical [Co/Al] nanodot arrays. (c) Schematic of the TR-MOKE measurement geometry. Background-subtracted time-resolved data for the reflectivity of (d) the Co NM arrays and (e) the [Co/Al] NM arrays, on Si substrate. (f) and (g) FFT of the respective oscillations. The two detected frequencies in the *non-plasmonic sample* correspond to SAW modes whose wavelengths are commensurate with distinct periodicities in real space and reciprocal space [inset of c)] of the NM arrays. e) and f) Surface plot of reflectivity spectra of the Co NM arrays on Si substrate and on identical [Co/Al] NM arrays, respectively.

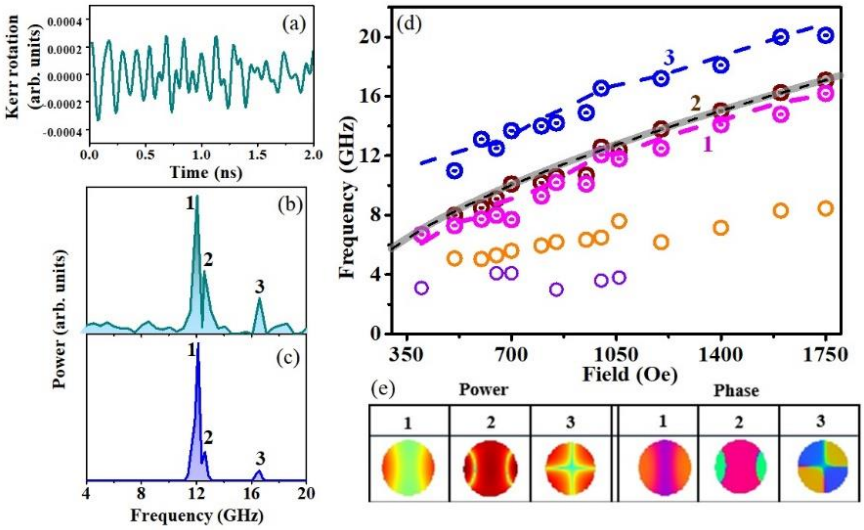

Figure 7.2. a) Background subtracted time-resolved Kerr oscillations from plasmonic samples, b) FFT of the corresponding oscillations. c) FFT of the simulated temporal evolution of the m_z component at 1kOe using OOMMF, showing good agreement with the experimentally measured spectra in (b). d) Bias magnetic field dependence of the observed three dominant frequencies in the Kerr oscillations. The circles represent experimental data and the solid line is Kittel fit for mode '2'. The dashed lines are micromagnetic simulation results.

In the regime of strong coupling[29], our system manifests a novel quasi-particle, a magnon-plasmon-phonon polariton, involving robust tripartite coupling between phonons, plasmons,

and magnons. This intriguing phenomenon, akin to magnon-plasmon polaritons observed in other systems, underscores the pivotal role of plasmons in our setup. Importantly, the absence of observable coupling in the Al-free sample highlights the qualitative impact of plasmons, demonstrating that plasmons introduce distinctions, not just quantitative changes, in spin-wave coupling.

Our experiments reveal two key findings: First, in the plasmonic sample with aluminum (Al), the magneto-optical Kerr effect (MOKE) signal shows a significant 30% increase in the average peak-to-peak Kerr rotation amplitude across all modes, persisting across a range of magnetic fields. Second, the FFT spectra demonstrate that the anti-crossed APSW modes in the Al-containing sample have an amplitude approximately four times greater than the field-dependent modes in the non-plasmonic sample.

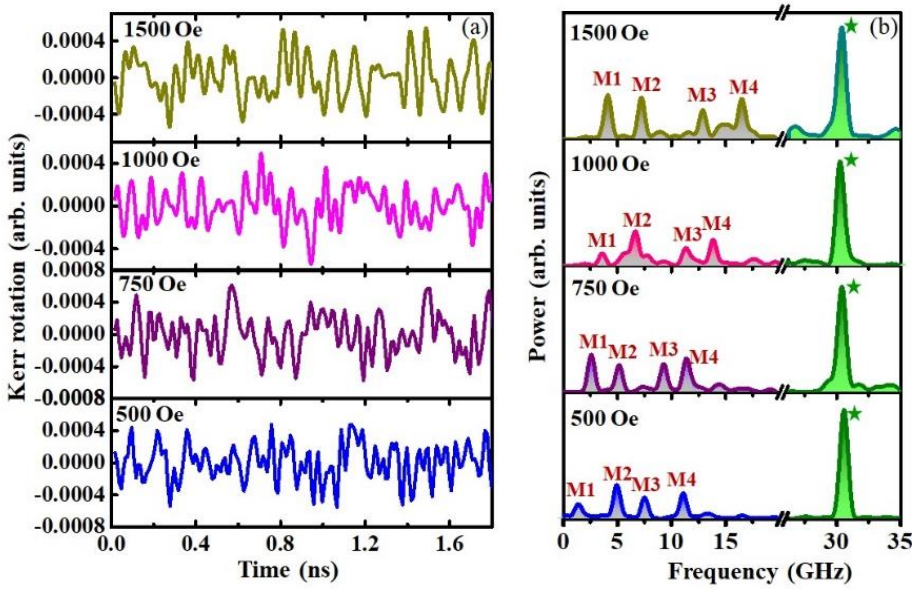

Figure 7.3.a) Bias magnetic field dependence of the background subtracted time-resolved Kerr oscillations from plasmonic samples. b) The FFT power spectra of the corresponding Kerr oscillations showing a field independent mode at 30.5 GHz, which is independent of the bias magnetic field.

Particularly, the intensity of the field-independent mode is ten times higher than that of the field-dependent modes. This notable enhancement in the MOKE signal, specifically the 30% rise in Kerr rotation amplitude in the Al-containing sample, indicates the presence of parametric amplification. This amplification is attributed to the transfer of energy from the hybridized phonon-plasmon mode to intrinsic spin-wave modes in the Al-containing sample, confirming robust tripartite plasmon-phonon-magnon coupling through the observed power transfer.

7.3 Conclusions

In summary, our study reveals (i) tripartite coupling among phonons, plasmons, and magnons in periodic bilayered nanodots of magnetostrictive and plasmonic materials, resulting in a high-frequency magnetic field-independent APSW mode; (ii) parametric amplification of spin-wave modes through hybrid phonon-plasmon modes; and (iii) strong coupling between two spin-wave modes mediated by the hybrid phonon-plasmon wave, forming the magnon-plasmon-phonon polariton. These findings advance our understanding of fundamental interactions in magnonic and plasmonic systems, with practical implications.

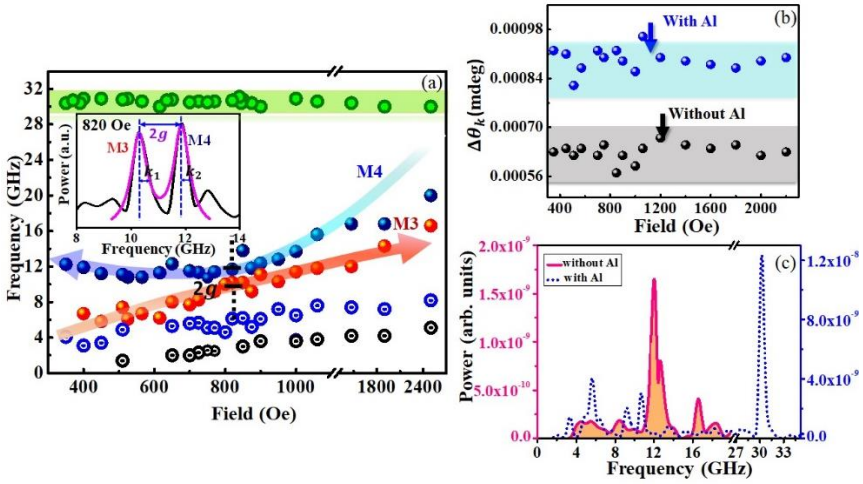

Figure 7.4. a) Experimental bias magnetic field dependence of Kerr oscillation modes in plasmonic samples. The lines with arrow heads are guide to the eye for the modes M4 and M3. A gap of frequency $2g$ opens up between these two dispersion curves at a magnetic field of 820 Oe, showing coupling between them at that magnetic field. Inset showing FFT power spectrum of the observed field-independent and field-dependent modes at the magnetic field of H = 820 Oe (black solid line). b) Average peak-to-peak Kerr rotation amplitude (averaged over all modes) in the plasmonic sample and in the non-plasmonic sample, as a function of the bias magnetic field. c) Amplitude of power in FFT spectra obtained from Kerr rotation of plasmonic and non-plasmonic samples at H =1 kOe.

The observed parametric amplification holds potential for spin-wave device applications, and the results open avenues for controlling spin dynamics through plasmon-phonon-photon interactions, offering exciting prospects for plasmon-driven coherent spintronics and magneto-optical activities.

Chapter 8

8. Large Dzyaloshinskii-Moriya interaction and its dependence on WS_2 layer in ferromagnet/WS_2 heterostructures

8.1 Introduction

Two-dimensional (2D) layered transition metal dichalcogenides (TMDs) are under intense scientific scrutiny for their distinctive features, including substantial spin-orbit coupling (SOC) from heavy metal d-orbitals, disrupted inversion symmetry in odd layers, and spin-valley coupling[2, 3]. Recent theoretical advancements drive exploration into combining 3d ferromagnets (FMs) with 2D TMDs for spin-based devices[4]. Monolayer and few-layer TMDs showcase potential in diverse spintronics functionalities, such as spin-charge interconversion, unconventional spin-orbit torque, field-free magnetization switching, and terahertz radiation emission.

TMDs, demonstrating stable monolayer growth with robust in-plane bonds, exhibit odd-even layer dependence due to characteristic inversion symmetry. In odd-layer TMDs, broken inversion symmetry, coupled with intrinsic SOC, induces spin-orbit splitting in electronic structure valleys, introducing an additional degree of freedom known as the valley degree of freedom[5].

This study addresses knowledge gaps through experiments on WS_2/Co_3FeB heterostructures, utilizing Brillouin light scattering (BLS) and substantiated by density functional theory (DFT) calculations. Variations in WS_2 thickness from one to four monolayers reveal layer-dependent interactions. Notably, WS_2 boasts the largest spin-orbit coupling (SOC) among sulfide-based transition metal dichalcogenides, surpassing heavy metals like Ta and W. These findings offer insights into manipulating magnetization in ferromagnet/TMD heterostructures, elucidating the interplay of inversion symmetry and asymmetry in monolayer to few-layer TMDs.

8.2 Results and Discussion

The number of WS_2 layers has been accurately identified by utilizing the peak separation of the Raman active modes which are analyzed from Fig. 1(a). Fig. 1(b) shows the results of

magnetization measurements on WS_2 (n_{ML})/Co_3FeB(6 nm) heterostructures. The inset in Fig. 1(b) shows the layer number dependence of the saturation magnetization. Apart from the smaller value of the saturation magnetization for the single-layer Co_3FeB(6 nm) sample, the figure indicates a weak decrease in the saturation magnetization with increasing thickness of the WS_2 layer. The variation of coercivity with the angle between the sample plane and the bias magnetic field direction is plotted in Fig. 1(c), which reveals that there is no uniaxial anisotropy present in this sample for odd and even number layer of WS_2.

The study employs Brillouin light scattering to investigate the iDMI in WS_2 (n_{ML})/Co_3FeB(6 nm) [n= 1,2,3,4] bilayers. The signature of DMI in BLS spectra is manifested as an asymmetry in the SW dispersion relation for nonreciprocal propagation of Damon-Eshbach (DE) spin waves,

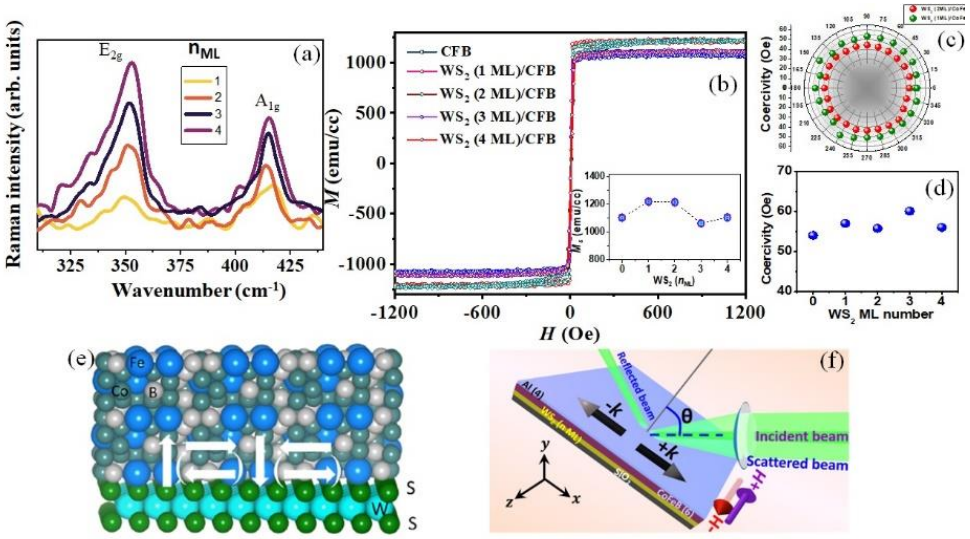

Figure 8.1. (a) Raman spectra of WS_2 with layer thickness ranging from one to four MLs, respectively. (b) Magnetization vs. magnetic field for WS_2 (n_{ML})/Co_3FeB(6 nm) (n_{ML} varying from zero to four MLs). Insets show the saturation magnetization. (c) In-plane variation of coercivity. (d) Variation of coercivity with layer number of WS_2. (e) Schematic of FM/TMD bilayer showing the magnetic vector chirality due to DMI from the WS_2 interface. (f) Schematic of the BLS measurement with the sample in Damon-Eshbach geometry

where the spin-wave wave vector and magnetization both lie in the sample plane and are mutually orthogonal. The experimental geometry is depicted in Figure 1(f). The iDMI constant is determined from the frequency difference Δf between spin waves with opposite wave vectors. The DMI constant is determined using [6],

$$\Delta f(k) = [\omega(-k) - \omega(k)]/2\pi = \frac{2\gamma}{\pi M_S} Dk \qquad \ldots\ldots\ldots (1)$$

where k is the x component of the wave vector, γ is the gyromagnetic ratio, and M_S is the saturation magnetization.

Figures 2(a)–(d) present Brillouin light scattering (BLS) spectra from WS_2/Co3FeB samples with varying WS_2 layers. Extracted Δf values, obtained through Lorentzian fitting, are plotted against measured k vectors in Fig. 3(e), revealing layer-dependent behaviors. The calculated D values, larger than W(2 nm)/Co20Fe60B20 and CoFeB/Ta, differ for odd and even WS2 layers due to spin-orbit coupling and spin-valley interactions. Surface DMI constants (D_s) are determined as 0.69(0.05), 0.71(0.04), 0.48(0.04), and 0.62(0.04) pJ/m for one to four MLs of WS_2, surpassing conventional materials like W and Ta and comparable to Pt/CoFeB. Two conclusions emerge: (i) WS_2 exhibits substantial DMI conducive for generation of chiral spin textures, and (ii) a reduction in DMI for the three-ML sample correlates with the calculated band structure and spin-valley coupling effects, aligning with experimental findings by Wu et al. [7]

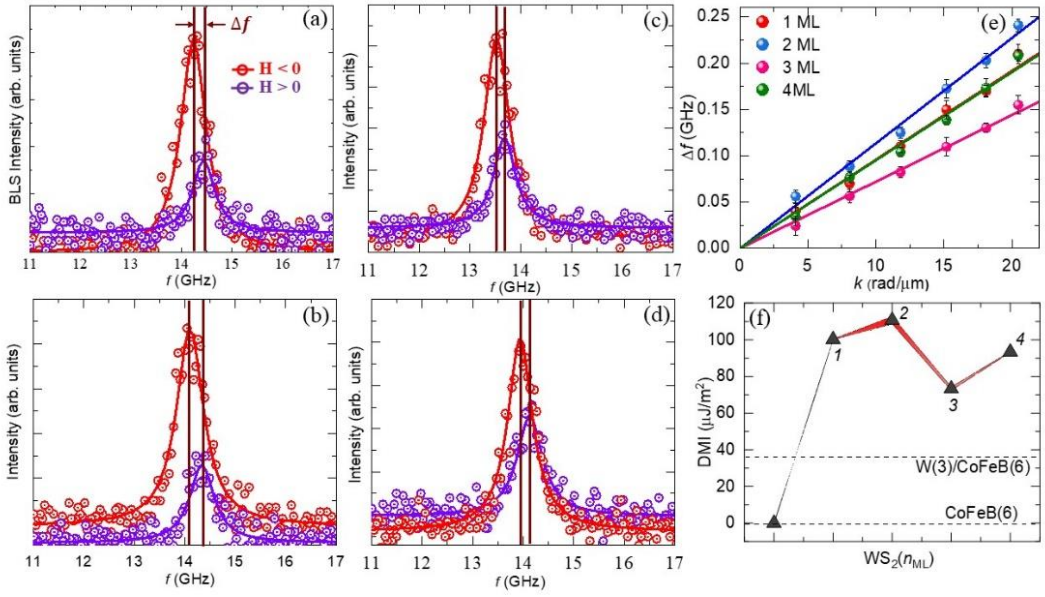

Figure 8.2. (a-d) Representative BLS spectra measured at wave vector $k = 20.45$ rad/μm under an external magnetic field of 0.1 T for WS_2 (n_{ML})/CoFeB(6 nm) with n_{ML} = 1, 2, 3, 4. The symbols represent the recorded BLS spectra, while the solid curves represent Lorentzian fits for two counterpropagating directions of spin waves. Vertical lines show the frequency difference due to asymmetry in the dispersion. (e) Frequency difference Δf of counterpropagating spin waves as a function of wave vector k for samples with different n_{ML}. (g) Variation of D with the number of WS_2 layers (the solid line is a guide to the eye). For reference, the D values for Co_3FeB(6 nm) and W(2 nm)/$CoFe_3B$(6 nm) are also mentioned.

8.3 Conclusions

DFT calculations and experimental results on $WS_2(n_{ML})/Co_3FeB$(6 nm) heterostructures reveal atomic layer thickness dependence, showcasing odd-even layer behavior due to spin-valley

coupling in WS_2. The layer-dependent splitting of valence band maxima and conduction band minima are visualized in calculations, aligning with DMI measurements. Key points include the applicability of a noncontact spin-dynamics approach to study spin-valley effects in WS_2 and the absence of spin-valley splitting at conduction band minima in one-ML WS_2, suggesting implications for designing 2D-material-based quantum devices.

Chapter 9

9. Anatomy of Interfacial Dzyaloshinskii-Moriya Interaction and Heisenberg Exchange with the Scaling of Spin-Orbit Coupling Strength at the Interface of Transition-Metal Dichalcogenides and Permalloy

9.1. Introduction

Spin-orbitronics harnesses spin-orbit coupling (SOC), a key factor in contemporary magnetism [1]. SOC's interaction with magnetism encompasses various interfacial phenomena such as interfacial perpendicular magnetic anisotropy (iPMA)[2], spin Hall effect[3], Rashba-Edelstein effect[4], spin pumping[5], interfacial Dzyaloshinskii-Moriya interaction (iDMI)[6, 7] and many more. The influence of strong SOC induces chirality in magnetic ground states [8, 9], thereby enhancing the electrical control over magnetic properties, as evidenced by experimental results[10, 11]. SOC's dependence on the atomic number (Z) to the fourth power makes heavy metals (HMs) ideal for nonmagnetic layers due to their high Z values [12-14]. Recently, two-dimensional (2D) materials including graphene[15-17], layered transition-metal dichalcogenides (TMDs)[18-21], and topological insulators[22, 23] have shown great potential for engineering interface magnetism.

Monolayer (ML) TMDs, particularly group-VI dichalcogenides MX_2, are known for their robust intrinsic SOC due to the HM's d-orbitals. This strong SOC arises from HM elements, creating pronounced spin-orbit interactions [24-26] that entangle spin and valley degrees of freedom in the valence band states at the K valleys [27]. Additionally, inversion symmetry breaking in odd-layer TMDs induces Rashba-type or Zeeman-type spin splitting, further enhancing SOC effects at the valence band edges of K valleys. [28-31]. These attributes confer high spin-orbit torque (SOT) efficiencies to TMD/ferromagnetic (FM) structures, enabling their seamless integration into spintronics and valleytronics applications[32-34]. Recent theoretical advancements highlight the potential of combining 3d ferromagnets with 2D TMDs for advanced spintronic devices. [24, 35]. Dual intercalation, involving both magnetic atoms and protons, has been reported as a promising method to tailor DMI and manipulate chiral spin textures in 2H-TaS_2, inspiring further exploration across a wide range of TMDs[36]. The magnetic proximity effect from FM substrates, resulting in giant valley exciton splitting in ML TMDs, further underscores the appeal of

TMD/FM heterostructures[37]. Among the various studied TMDs, Mo- and W-based TMDs stand out due to the presence of heavy transition metals: Mo and W, exhibiting significant spin splitting in the valence bands at the K-point. Figure 1(b) shows the theoretical spin splitting values[25] of the valence band and the SOC parameter for these ML TMDs, revealing a monotonic increase in SOC from MoS_2 to $MoSe_2$ to WS_2 to WSe_2.

In magnetic systems, the interatomic exchange interaction (Heisenberg exchange) loses its symmetry under the influence of both SOC and broken local spatial inversion symmetry. This disruption gives rise to the antisymmetric component of the exchange interaction, known as DMI[6, 7], which arises from a three-site indirect exchange mechanism, as shown schematically in the inset of Figure 1 (a)[38, 39]. The interplay between the Heisenberg exchange interaction and iDMI can induce intricate chiral magnetic orders such as spin spirals[40], skyrmions[41], skyrmionic cocoons[42] in both 2D and 3D magnetic systems, hopfions[43] and so on[44-46]. The Rashba model predicts that the interfacial SOT is influenced by the ratio of symmetric to antisymmetric exchange interactions[47]. Therefore, precise control over material systems' ground states or functional devices necessitates accurate quantification of both the iDMI constant (D) and the Heisenberg exchange constant (A) in ultrathin magnetic films.

Measuring the exchange interactions in ultrathin magnetic films is highly complex because the methods and approximations that work well for bulk materials do not apply effectively in the 2D limit. Conventional methods employed for thick films, such as resonance modes[48], often prove inadequate in the 2D limit or are hampered by signal-to-noise constraints. Magnetometry-based approaches relying on the Bloch law are commonly used[12, 49] but their applications to ultrathin films raise concerns about the validity of the underlying 3D model, lacking consensus on mitigation strategies[50]. Hence, rigorous quantitative benchmarking of A values for ultrathin magnetic films is imperative, with techniques such as Brillouin light scattering (BLS) offering promising avenues for advancement[51, 52]. On the other hand, various direct and indirect measurement techniques including BLS[4, 12, 14, 53], magnetic domain wall velocity measurements[54], asymmetric hysteresis loop[55] etc. methods have been employed to measure iDMI.

Recent studies investigating the WS_2/Co_3FeB system have demonstrated larger iDMI compared to conventional HM/FM interfaces like W or Ta/CoFeB[19]. Similarly, investigations into few-layer $MoS_2/Ni_{80}Fe_{20}$ ($Ni_{80}Fe_{20}$: Permalloy, abbreviated as Py hereafter) heterostructures have

revealed enhanced iDMI relative to graphene/Py systems[16], with surface DMI in MoS_2/Py comparable to HM/FM bilayers of equivalent ferromagnetic thickness. Although HM/FM systems[56, 57] have been extensively studied, investigations into iDMI in 2D-TMD/FM systems remain relatively scarce. Despite theoretical and experimental efforts to elucidate the correlation between iDMI and SOC[58, 59], a systematic experimental study that correlates both symmetric and antisymmetric exchange interactions with SOC remains conspicuously absent in current literature.

In this work, we present a systematic investigation into the extraction of exchange constants—both Heisenberg exchange constant and iDMI constant—at the interface of Py (7nm) and large-area ML TMDs including MoS_2, $MoSe_2$, WS_2, and WSe_2. In sputtered thin films, the presence of small grains with varying lattice orientations leads to the cancellation of bulk DMI, leaving only the iDMI effective. Utilizing large-area chemical vapor-deposited ML TMDs [TMDs will refer to (MoS_2, $MoSe_2$, WS_2, and WSe_2), throughout this chapter] interfaced with sputtered Py thin films, we observed asymmetric SW dispersion in the DE geometry across all TMDs/Py (7nm) samples. To validate the interfacial origin of the DMI, we have also varied the thickness of the Py layer (7 nm,10 nm and 15 nm) interfaced with TMDs. The frequency shift between $+k$ and $-k$ propagation directions (k : wavevector) displayed a linear dependence on k at constant magnetic field, enabling extraction of iDMI values inversely proportional to Py thickness. Our findings reveal a consistent increase in exchange constants aligning with SOC strength in ML TMD layers. This study provides a comprehensive understanding of SOC effects at TMD/FM interfaces and associated exchange interactions, thereby advancing the prospects for manipulating nanoscale chiral spin textures and innovating TMD-based nanoscale spin-orbitronic devices.

9.2. Experimental and Theoretical Methods

9.2.1. Static Characterization

We investigated Al_2O_3/ML TMD/Py(7)/Ta(3) [the number in parentheses represents the thickness in nm, as consistently used throughout this chapter] samples, as schematically depicted in Figure 7.1(a), for four distinct large-area ($\sim 5 \times 2$ mm^2) TMDs: MoS_2, $MoSe_2$, WS_2, and WSe_2. Figure 7.1(c) presents the in-plane magnetization hysteresis loops of the sample stacks, measured by vibrating sample magnetometer (VSM) at room temperature.

The Raman spectra of ML TMDs/Py are depicted in Figure 7.1(d)-(g). For both MoS_2/Py (Figure 7.1(d)) and WS_2 (Figure 7.1(f)) samples, two peaks, corresponding to the E^1_{2g} and A_{1g} Raman

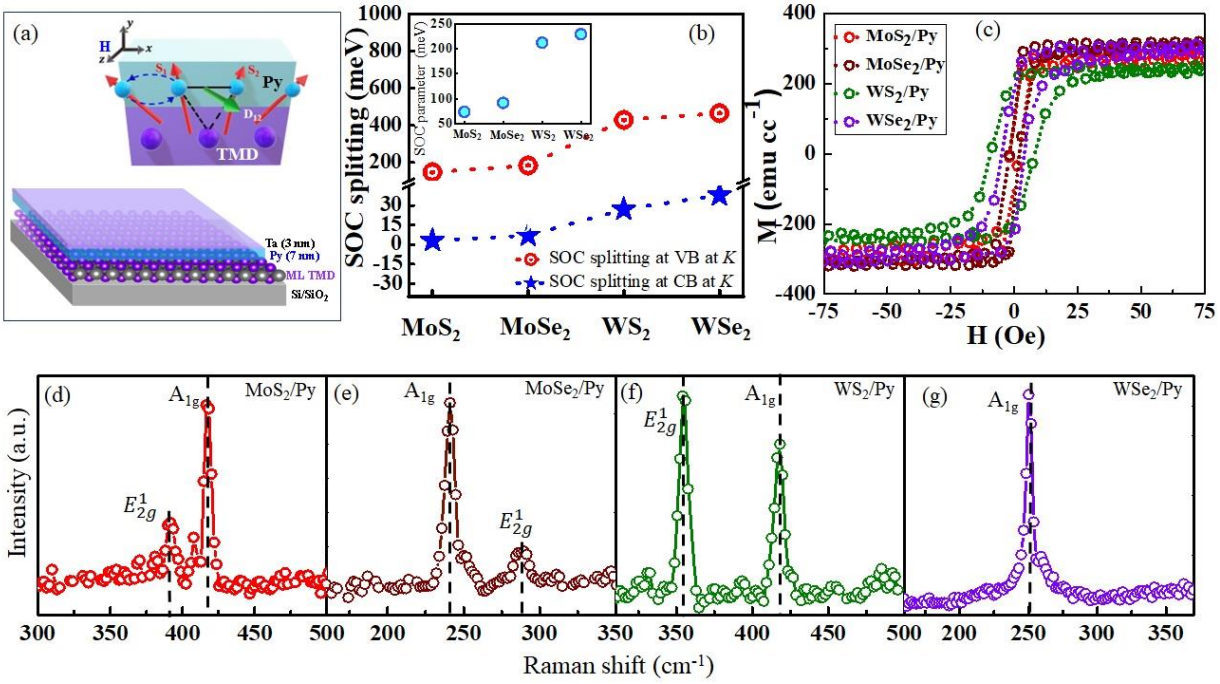

Fig. 9.1. (a) Schematic of the ML TMD/FM heterostructure used in the experiment. Inset: Schematic of the IDMI mechanism. (b) Theoretical spin splitting of the uppermost valence band at the K-point for different ML TMDs, inset shows the corresponding SOC parameter, taken from ref. [26]. (c) Magnetization vs magnetic field for ML TMDs/Py(7). (d) – (g) Raman spectra for different ML TMDs after the deposition of Py and Ta layers.

modes were identified[18, 60]. The E^1_{2g} and A_{1g} peaks are separated by 20.3 cm^{-1} for MoS_2 and 62.2 cm^{-1} for WS_2, confirming their ML thickness[61, 62]. The absence of the B^1_{2g} mode around 353 cm^{-1} (Figure 7.1(e)) and 309 cm^{-1} (Figure 7.1(g)) aligns with previously reported Raman spectra for monolayer $MoSe_2$ and WSe_2, respectively[63]. Singular strong A_{1g} Raman modes at 240 cm^{-1} (Figure 7.1(d)) and 251 cm^{-1} (Figure 7.1(f)) serve as distinctive characteristics of monolayer $MoSe_2$ and WSe_2, respectively[64]. To validate large-area coverage of monolayer TMDs, Raman measurements were conducted at various locations, yielding consistent spectra across the entire substrate (5 × 2 mm^2) and affirming the presence of large-area ML TMDs.

Figure 7.2(a) – (e) shows the AFM images for the ML TMDs/Py (7) sample stack along with reference Py (7) sample to investigate the surface topography. The roughness remains nearly constant at ~0.35 nm for the TMDs/Py heterostructures which is higher than the reference Py

(7) film, which is of ~ 0.25 nm as shown in Figure 7.2(f). R_a values exhibited minimal variation when

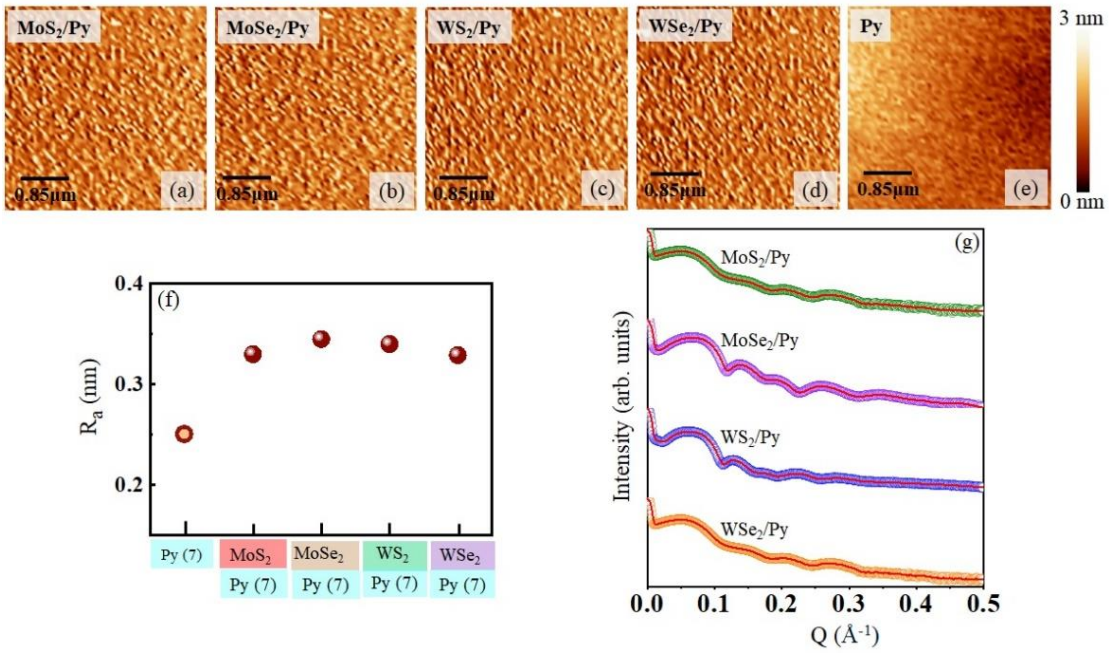

Figure 9.2. AFM images of the (a) MoS_2/Py, (b) $MoSe_2$/Py, (c) WS_2/Py, (d) WSe_2/Py and (e) Py. (f) Variation of the average topographical roughness (R_a) extracted from the AFM images. (g) XRR spectra (open circles) for ML TMD/Py samples fitted using REFLEX (solid line).

measured across different areas of the same film stack, ensuring the smooth deposition of the heterostructures.

XRR measurements were conducted on the as-deposited samples to verify their thickness. Figure 7.2(g) presents well-fitted XRR data for the ML TMDs/Py heterostructures. The XRR fitting parameters, obtained using the REFLEX fitting software, for the sample stacks are listed in the table below.

Sample	Layer	Thickness (nm)	Roughness (nm)	Sample	Layer	Thickness (nm)	Roughness (nm)
ML MoS_2/Py (7)	Al_2O_3	--	1.500	ML WS_2/Py (7)	Al_2O_3	--	1.616
	MoS_2	0.650	0.028		WS_2	1.020	0.020
	Py	7.014	0.313		Py	7.018	0.311
	Ta	1.501	0.586		Ta	1.403	0.533
	Ta_2O_5	1.547	1.150		Ta_2O_5	1.661	1.300

ML $MoSe_2$/Py (7)	Al_2O_3	--	1.555	ML WSe_2/Py (7)	Al_2O_3	--	1.610
	$MoSe_2$	0.790	0.031		WSe_2	0.984	0.045
	Py	7.025	0.309		Py	7.005	0.257
	Ta	1.449	0.521		Ta	1.403	0.554
	Ta_2O_5	1.672	1.200		Ta_2O_5	1.685	1.350

9.2.2. SW Measurement Technique

The SW dispersion of the ML TMDs (MoS_2, $MoSe_2$, WS_2, WSe_2)/Py (7) was measured exploiting BLS spectroscopy in the DE geometry at room temperature. A single-mode continuous wave solid-state laser with a wavelength of 532 nm and a power of ~ 60 mW is directed onto the sample. Conventional back-scattered geometry, with the provision of *k*-selectivity by varying the angle of incidence, was employed to probe the SW dispersion, with *k* ranging from 0 to 20.45 rad/μm. The back-scattered light was collected by an achromatic lens and directed to a (3+3)-pass Sandercock type tandem-Fabry-Pérot interferometer for the spectral analysis to detect the SW frequencies. Figure 7.3 (a) illustrates the schematic of the BLS measurement geometry, where *H* and *k* represent two mutually perpendicular quantities, namely, the in-plane bias magnetic field and wave vector, respectively. The external magnetic field applied in-plane to the magnetic film, with sufficiently large magnitude to saturate each sample in the in-plane direction. In this scattering process, where total momentum is conserved along the film surface, Stokes (magnon creation) and anti-Stokes (magnon annihilation) peaks emerge from SWs propagating in the -x and +x directions, respectively. Consequently, counterpropagating SWs under oppositely oriented *H* along the z axis with identical momentum is detected simultaneously as the Stokes and anti-Stokes peaks in the spectra.

To accurately determine the static magnetic parameters of the samples, we measured the dependence of SW frequency on the bias magnetic field using BLS spectroscopy at $k \approx 0$ (uniform precessional mode). As shown in Figure 7.3(f), the SW frequency increases with the bias magnetic field. The variation of SW frequency with the bias magnetic field was fitted using the Kittel formula[65] given by equation (7.1):

$$f = \frac{\gamma}{2\pi}\sqrt{H(H + 4\pi M_{eff})} \quad \ldots (9.1)$$

Here, $\gamma = \frac{g\mu_B}{\hbar}$ is gyromagnetic ratio, H is the bias magnetic field, g is the Landé g factor, μ_B is the Bohr magneton, h is the Planck constant and M_{eff} is the effective magnetization. From the fit, the values of g and M_{eff} were obtained as fitting parameters. The value of M_{eff} was found to be close to the saturation magnetization (M_S) obtained from VSM measurements, as depicted in Figure 7.3 (g), indicating negligible interface anisotropy in our samples. This methodology for estimating M_{eff} is consistent with existing literature[12, 66].

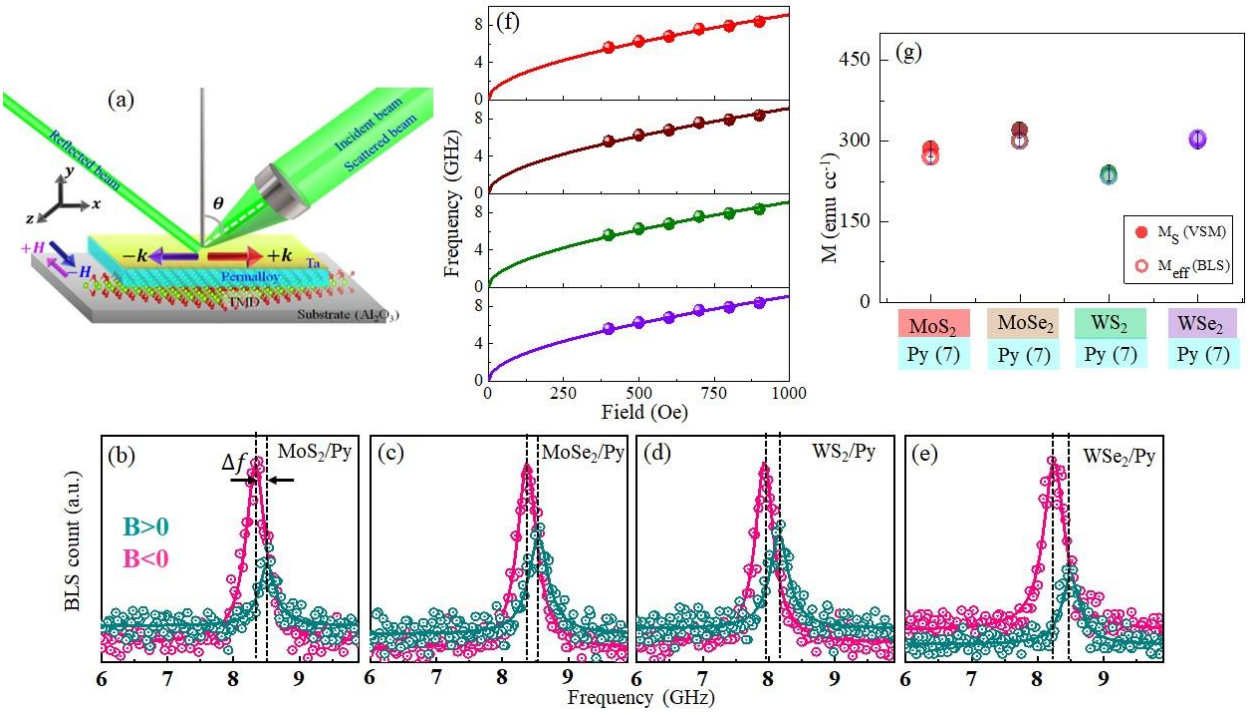

Figure 9.3. (a) Schematic of the BLS measurement with the sample stack in Damon-Eshbach geometry. (b)–(e) Representative BLS spectra measured at wave vector k = 20.45 rad/μm under an external magnetic field of 0.04 T for ML MoS_2/Py (7 nm), ML $MoSe_2$/Py (7 nm), ML WS_2/Py (7 nm) and ML WSe_2/Py (7 nm). The symbols represent the recorded BLS spectra, while the solid curves represent Lorentzian fits for two counterpropagating directions of SWs. Vertical lines show the frequency difference due to asymmetry in the dispersion. (f) Plot of frequency vs. magnetic field for TMD/Py stack at $k \approx 0$. Experimental data points are indicated by symbols, while the solid line represents the fit based on the Kittel formula, [given as equation (7.1)] (g) Variation of magnetization with the TMD layer, M_{eff} is calculated from BLS measurement (hollow circle) and M_S from VSM measurement

9.2.3. Extraction of Exchange Constants and SW Dispersion Study

Experimental BLS spectra for TMDs/Py samples are depicted in Figure 7.3 (b)-(e) at k = 20.45 rad/μm under an external magnetic field of 0.04 T. The BLS spectra are fitted with a single Lorentzian function, indicated by a solid line, to extract the SW frequency for each wave vector.

Magenta and green symbols represent the BLS spectra for an applied magnetic field B = 0.04 T in two opposite directions along the z-axis. The frequency difference (Δf) between the peak positions of counterpropagating SWs ($\pm k$; along $\pm$x) is indicative of the strength of the iDMI.

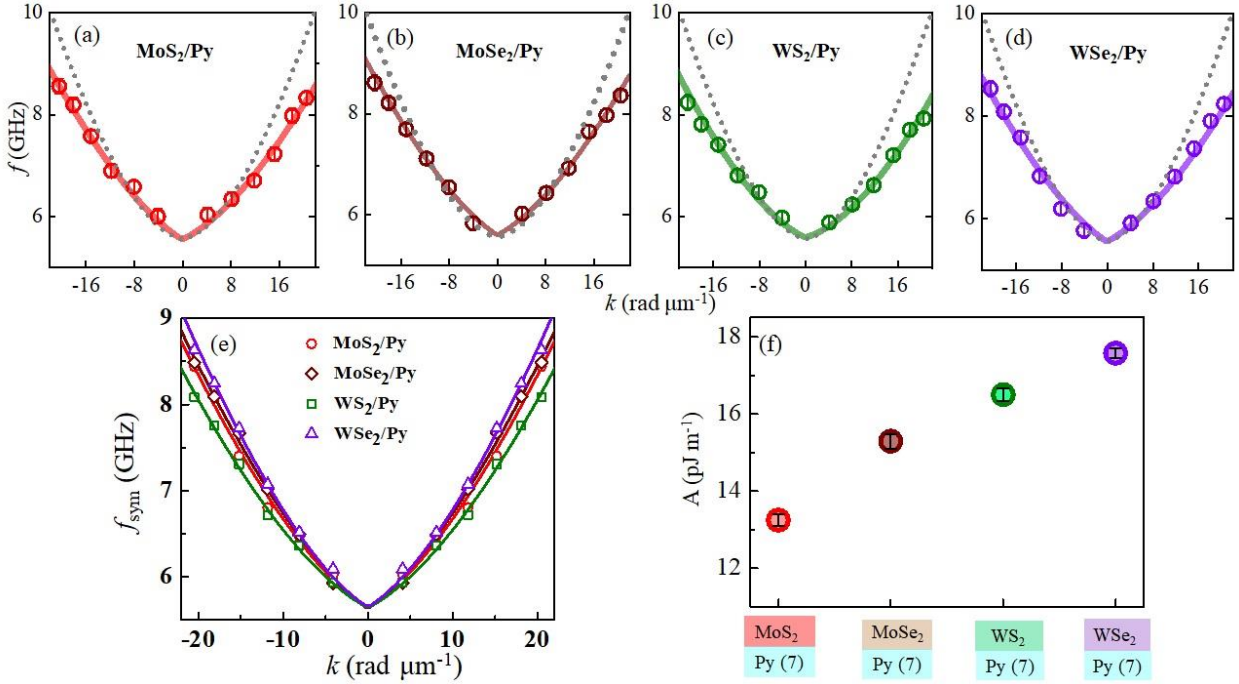

Figure 4. Experimental SW dispersion for (a) MoS_2/Py, (b) $MoSe_2$/Py, (c) WS_2/Py and (d) WSe_2/Py. Hollow spheres are the experimental data points with error bars and the solid line is fitted curve using Eq. 7.2. The dotted black line is the dispersion relation for the reference Py (7 nm) sample. (e) Symmetrized SW dispersion relation (dots) and the solid line fit in accordance with Eq. (1). (f) Experimental and theoretical exchange stiffness constant (A) for TMDs/Py (7 nm).

The full dispersion relation of the ML TMDs/Py at B = 0.04 T, shown by the hollow circles in Figure 7.4 (a)-(d), clearly exhibits a pronounced asymmetry with respect to wave-vector inversion, which is a consequence of the iDMI[67]. It is modelled using a modified SW dispersion relation[14] after incorporating the DMI effect in the DE geometry, represented by solid line fit.

$$\omega = \omega_0 + \omega_{DM} = \mu_0\gamma\sqrt{[H + Jk^2 + \xi(kL)M_S][H - H_U + Jk^2 + M_S - \xi(kL)M_S]} - 2\frac{\gamma}{M_S}Dk \quad \ldots(9.2)$$

Here, L is the thickness of the Py film, H_U ($= \frac{2K_U}{\mu_0 M_S}$, K_U is the uniaxial anisotropy constant) is the uniaxial anisotropy field and $\xi(kL) = 1 - \frac{1-e^{|-kL|}}{|kL|}$, accounts for the dipolar interactions, J ($= \frac{2A}{\mu_0 M_S}$), with the Heisenberg exchange stiffness constant A and D is the iDMI constant. In Eq.

(2), we used respective M_S values from VSM measurements and g = 2.00 ± 0.01 for all ML TMDs/Py (7) samples to determine D at different Py thicknesses.

The symmetrized dispersion relation, obtained by averaging the SW frequencies for positive and negative wave vectors, provides a more accurate means of extracting A and is given by[51],

$$f(k)_{Sym}=\frac{\omega(-k)+\omega(k)}{4\pi}=\frac{\mu_0\gamma}{2\pi}\sqrt{[H+Jk^2+\xi(kL)M_S][H-H_U+Jk^2+M_S-\xi(kL)M_S]} \quad \ldots(9.3)$$

Figure 7.4(e) displays representative symmetrized BLS dispersion data for the monolayer TMDs (MoS_2, $MoSe_2$, WS_2, WSe_2)/Py (7) samples, with the fitted results from the dispersion model [Eq. (7.3)] overlaid. The influence of the symmetric exchange is encapsulated in the SW stiffness, J. We have used g = 2.00±0.1 for all of the samples, M_S is obtained from the VSM measurements.

The fitted experimental data yielded the following best fit model parameters:

Parameter	MoS_2/Py (7 nm)	$MoSe_2$/Py (7 nm)	WS_2/Py (7 nm)	WSe_2/Py (7 nm)
H_U (kA m^{-1})	27.94± 1.6	27.37± 1.5	39.81± 1.7	30.78± 1.9
A (pJ m^{-1})	13.25± 0.35	15.29± 0.28	16.50± 0.30	17.57± 0.32

In Figure 7.4(f), we have plotted experimentally obtained values of A, which show a monotonic increment with the SOC strength.

The iDMI constant can also be calculated from the frequency difference (Δf) between SWs propagating in opposite directions ($+k$ and $-k$), as described by Eq. (7.3)[14]. An asymmetry in the frequencies of Stokes and anti-Stokes peaks is evident in all TMDs/Py samples. Interestingly, the reference sample showed almost no Δf, ruling out any iDMI contribution from the Py and Ta capping layer interface. Figure 7.5(a) displays a linear variation of Δf with k for all four TMD/Py (7 nm) samples, with the maximum slope for WS_2/Py (7 nm) and the minimum for $MoSe_2$/Py (7 nm).

$$\Delta f=\frac{\omega(-k)-\omega(+k)}{2\pi}=\frac{2\gamma}{\pi M_s}Dk \quad \ldots(9.4)$$

The extracted values of D for the ML TMDs/Py(7 nm) are plotted in Figure 7.5(b). A positive slope was observed in all samples, indicating $D > 0$ and favouring right-handed chirality[4].

Thus, the derived value of D is found to be consistent from two types of modelling the experimental data (Eq. 7.2 and 7.4). Figure 7.5(c) illustrates the linear dependence of D on the inverse of Py thickness, indicating a pure interfacial origin of iDMI in the ML TMD/Py heterostructures. The solid lines in Figure 7.5 (c) represent linear fits to the data using the following equation[4]:

$$D = \frac{D_S}{t_{Py}} \quad \ldots (9.5)$$

Here, D_S is the strength of the surface DMI parameter, which is independent of the FM thickness. The values of D_S are found to be (322.98± 1.55) fJm^{-1}, (347.20± 1.52) fJm^{-1}, (382.83± 1.50) fJm^{-1} and (429.31± 1.50) fJm^{-1} for ML MoS_2/Py, $MoSe_2$/Py, WS_2/Py and WSe_2/Py, respectively.

The D_S values of ML MoS_2/Py and WS_2/Py are comparable to those of the previously studied 2L MoS_2/Py system[18] and ML WS_2/Co_3FeB[19] system, respectively. Notably, the sign of iDMI in ML MoS_2/Py contrasts with that in 2L and 3-4L MoS_2/Py heterostructures. This disparity is attributed to the unique properties of ML MoS_2, absent in bilayer or few-layer MoS_2[33]. The observed values exceed the previously reported results for monolayer graphene system[16], Py/Pt multilayers system[68] and are comparable to the widely studied Pt-based systems[12, 69].

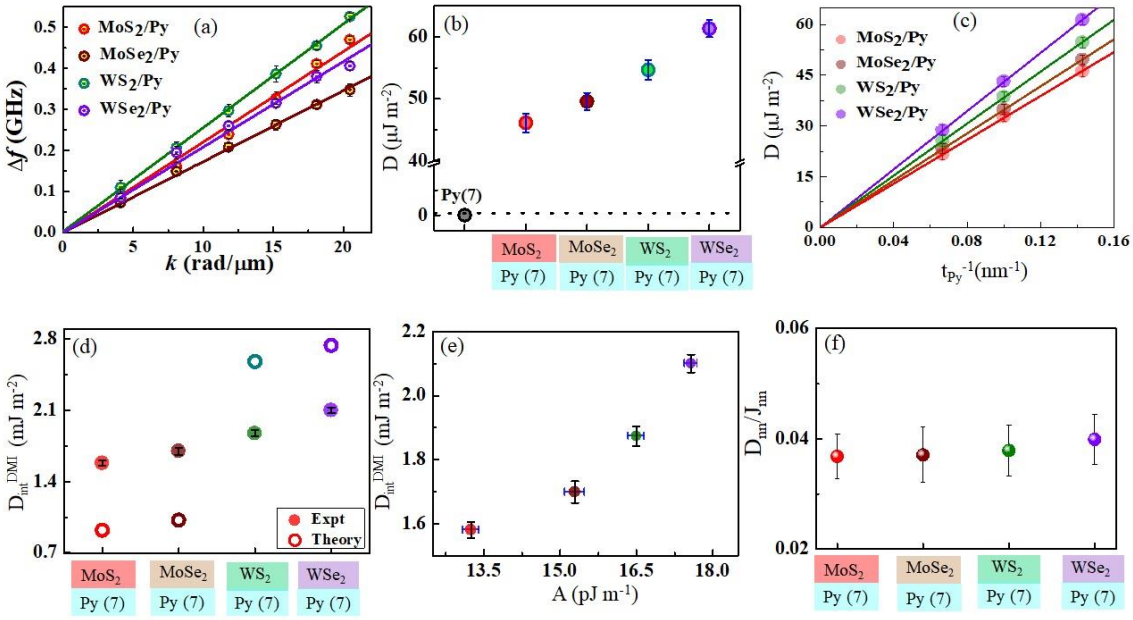

Figure 7.5. (a) Frequency difference Δf of counterpropagating SWs as a function of wave vector k for TMD/Py samples. (b) Variation of D for ML TMDs/Py (7 nm), for reference, the D value for Py (7 nm) is also mentioned. (c) Experimental and theoretical values of D_{int} for ML TMDs/Py (7 nm). (d) Correlation of D_{int} and A. (e) Ratio of the nearest-neighbour exchange integral J_{nn} and the magnitude of the nearest-neighbour DMI D^{nn} is plotted for ML TMDs/Py.

Apart from the macroscopic DMI constant (D), considering solely the first monolayer of Py at the TMD interface contributes to the antisymmetric exchange, the magnitude of the DMI at the interface, denoted as D_{int}, can be computed from[12]:

$$D_{int} = D\frac{\sqrt{3}t}{a} \quad \ldots (9.6)$$

Where, a = 0.354 nm is the lattice constant of the Py and t is the thickness of the ferromagnetic layer.

The ratio of the iDMI constant to the exchange constant can be linked to the fundamental parameters of symmetric and antisymmetric exchange as[12]: $\frac{D_{int}}{A} = \frac{3}{2\sqrt{2}}\frac{1}{a}\frac{D_{nn}}{J_{nn}}$ … (9.7)

where J_{nn} is the nearest-neighbour exchange integral and D_{nn} is the magnitude of the nearest-neighbour DMI integral.

We have plotted D_{int} vs A in Figure 7.5(e) and also extracted the ratio of the antisymmetric and symmetric exchange ($\frac{D_{nn}}{J_{nn}}$), which is independent of the FM thickness, for TMDs/Py system as depicted in Figure 7.5(f). The magnitude of *A*, *D* and $\frac{D_{nn}}{J_{nn}}$ is found to increase monotonically in the sequence $MoS_2 \rightarrow MoSe_2 \rightarrow WS_2 \rightarrow WSe_2$, suggesting a direct correlation of the measured parameters and SOC strength of the ML TMDs.

The linear relationship between symmetric and antisymmetric exchange was initially conjectured for bulk materials[7], anticipated in metallic spin-glass systems[38, 70], and validated in the Pt/Py[12] system. Our findings affirm that this relationship extends to the interface between a ferromagnetic layer and TMD material exhibiting significant SOC.

Despite the prevalent existence of Rashba SOC in TMDs, their effects have only recently been extensively studied, primarily focusing on spintronic applications[21, 71-73]. Experimental investigations have explored the correlation between iDMI and the Rashba shift, although direct estimation of A has been lacking there[17]. Our study provides a method to estimate the Rashba shift (k_R) at the TMD/FM interface by extracting both exchange constants[47]. On the other hand, ML TMDs interfacing with FMs demonstrate significant interfacial SOT[73, 74] and exhibit gate-tunable SOT capabilities[75] via electric field-modulated carrier concentration and interfacial Rashba effects. Our study can also demonstrates the direct extraction of the field-like and

damping-like components of SOT through the quantification of both D and A[47], utilizing the concept of chiral derivatives.

9.3. Conclusions

In summary, through systematic measurements of the thermal SW spectrum, we independently determined the iDMI constant D and the symmetric exchange constant A, in ML TMDs/Py heterostructures using BLS spectroscopy. The dependence of DMI on FM thickness indicates a predominant interfacial origin in the studied system. We observed a linear variation of symmetric and antisymmetric exchange with the strength of the SOC at the surface of TMDs. Our findings confirm that the linear proportionality between symmetric and antisymmetric exchange applies to 2D systems at the interface between a ferromagnetic layer and a TMD material, with D and A correlating with SOC strength at the TMD surface. This underscores SOC's crucial role in influencing D and A in these samples. Given that D and A are essential for stabilizing chiral spin textures, our results promise the potential for stabilizing and manipulating nanoscale skyrmions at the ML TMDs/FM interface, advancing the development of next-generation energy-efficient memory and logic devices. Additionally, this study paves the way for extracting Rashba shift and the field-like and damping-like components of SOT directly through experiments. The methods and results presented not only elucidate fundamental DMI properties but may also significantly impact the methodology for developing spin-orbitronic devices.

References

[1] A. Soumyanarayanan, N. Reyren, A. Fert, C. Panagopoulos, *Nature* **2016**, 539, 509.
[2] P. F. Carcia, A. D. Meinhaldt, A. Suna, *Applied Physics Letters* **1985**, 47, 178.
[3] J. E. Hirsch, *Physical Review Letters* **1999**, 83, 1834.
[4] M. Belmeguenai, J.-P. Adam, Y. Roussigné, S. Eimer, T. Devolder, J.-V. Kim, S. M. Cherif, A. Stashkevich, A. Thiaville, *Physical Review B* **2015**, 91, 180405.
[5] Y. Tserkovnyak, A. Brataas, G. E. W. Bauer, *Physical Review B* **2002**, 66, 224403.
[6] I. Dzyaloshinsky, *Journal of Physics and Chemistry of Solids* **1958**, 4, 241.
[7] T. Moriya, *Physical Review* **1960**, 120, 91.
[8] A. Thiaville, S. Rohart, É. Jué, V. Cros, A. Fert, *Europhysics Letters* **2012**, 100, 57002.
[9] S. Heinze, K. von Bergmann, M. Menzel, J. Brede, A. Kubetzka, R. Wiesendanger, G. Bihlmayer, S. Blügel, *Nature Physics* **2011**, 7, 713.
[10] S. Emori, U. Bauer, S.-M. Ahn, E. Martinez, G. S. D. Beach, *Nature Materials* **2013**, 12, 611.
[11] K.-S. Ryu, L. Thomas, S.-H. Yang, S. Parkin, *Nature Nanotechnology* **2013**, 8, 527.
[12] H. T. Nembach, J. M. Shaw, M. Weiler, E. Jué, T. J. Silva, *Nature Physics* **2015**, 11, 825.
[13] A. Barman, J. Sinha, Springer International Publishing, 2018.
[14] K. Di, V. L. Zhang, H. S. Lim, S. C. Ng, M. H. Kuok, J. Yu, J. Yoon, X. Qiu, H. Yang, *Physical Review Letters* **2015**, 114, 047201.

[15] H. Yang, G. Chen, A. A. C. Cotta, A. T. N'Diaye, S. A. Nikolaev, E. A. Soares, W. A. A. Macedo, K. Liu, A. K. Schmid, A. Fert, M. Chshiev, *Nature Materials* **2018**, 17, 605.
[16] A. K. Chaurasiya, A. Kumar, R. Gupta, S. Chaudhary, P. K. Muduli, A. Barman, *Physical Review B* **2019**, 99, 035402.
[17] A. K. Mondal, S. Majumder, S. Sahoo, S. N. Panda, S. Sinha, A. Barman, *ACS Applied Nano Materials* **2022**, 5, 5056.
[18] A. Kumar, A. K. Chaurasiya, N. Chowdhury, A. K. Mondal, R. Bansal, A. Barvat, S. P. Khanna, P. Pal, S. Chaudhary, A. Barman, P. K. Muduli, *Applied Physics Letters* **2020**, 116, 232405.
[19] S. Husain, S. Pal, X. Chen, P. Kumar, A. Kumar, A. K. Mondal, N. Behera, N. K. Gupta, S. Hait, R. Gupta, R. Brucas, B. Sanyal, A. Barman, S. Chaudhary, P. Svedlindh, *Physical Review B* **2022**, 105, 064422.
[20] S. Dutta, S. Husain, P. Kumar, N. K. Gupta, S. Chaudhary, P. Svedlindh, A. Barman, *Nanoscale* **2024**, 16, 4105.
[21] H. Bangar, A. Kumar, N. Chowdhury, R. Mudgal, P. Gupta, R. S. Yadav, S. Das, P. K. Muduli, *ACS Applied Materials & Interfaces* **2022**, 14, 41598.
[22] J. Liu, T. Hesjedal, *Advanced Materials* **2023**, 35, 2102427.
[23] S. Mukhopadhyay, P. K. Pal, S. Manna, C. Mitra, A. Barman, *NPG Asia Materials* **2023**, 15, 57.
[24] D. Xiao, G.-B. Liu, W. Feng, X. Xu, W. Yao, *Physical Review Letters* **2012**, 108, 196802.
[25] G.-B. Liu, W.-Y. Shan, Y. Yao, W. Yao, D. Xiao, *Physical Review B* **2013**, 88, 085433.
[26] X. Xu, W. Yao, D. Xiao, T. F. Heinz, *Nature Physics* **2014**, 10, 343.
[27] W. Yao, D. Xiao, Q. Niu, *Physical Review B* **2008**, 77, 235406.
[28] H. Yuan, M. S. Bahramy, K. Morimoto, S. Wu, K. Nomura, B.-J. Yang, H. Shimotani, R. Suzuki, M. Toh, C. Kloc, X. Xu, R. Arita, N. Nagaosa, Y. Iwasa, *Nature Physics* **2013**, 9, 563.
[29] A. Manchon, H. C. Koo, J. Nitta, S. M. Frolov, R. A. Duine, *Nature Materials* **2015**, 14, 871.
[30] H. Zeng, J. Dai, W. Yao, D. Xiao, X. Cui, *Nature Nanotechnology* **2012**, 7, 490.
[31] T. Cao, G. Wang, W. Han, H. Ye, C. Zhu, J. Shi, Q. Niu, P. Tan, E. Wang, B. Liu, J. Feng, *Nature Communications* **2012**, 3, 887.
[32] W. Choi, N. Choudhary, G. H. Han, J. Park, D. Akinwande, Y. H. Lee, *Materials Today* **2017**, 20, 116.
[33] S. Manzeli, D. Ovchinnikov, D. Pasquier, O. V. Yazyev, A. Kis, *Nature Reviews Materials* **2017**, 2, 17033.
[34] J. Ingla-Aynés, F. Herling, J. Fabian, L. E. Hueso, F. Casanova, *Physical Review Letters* **2021**, 127, 047202.
[35] D. W. Latzke, W. Zhang, A. Suslu, T.-R. Chang, H. Lin, H.-T. Jeng, S. Tongay, J. Wu, A. Bansil, A. Lanzara, *Physical Review B* **2015**, 91, 235202.
[36] G. Zheng, M. Wang, X. Zhu, C. Tan, J. Wang, S. Albarakati, N. Aloufi, M. Algarni, L. Farrar, M. Wu, Y. Yao, M. Tian, J. Zhou, L. Wang, *Nature Communications* **2021**, 12, 3639.
[37] T. Norden, C. Zhao, P. Zhang, R. Sabirianov, A. Petrou, H. Zeng, *Nature Communications* **2019**, 10, 4163.
[38] A. Fert, P. M. Levy, *Physical Review Letters* **1980**, 44, 1538.
[39] A. Fert, V. Cros, J. Sampaio, *Nature Nanotechnology* **2013**, 8, 152.
[40] M. Uchida, Y. Onose, Y. Matsui, Y. Tokura, *Science* **2006**, 311, 359.
[41] S. Mühlbauer, B. Binz, F. Jonietz, C. Pfleiderer, A. Rosch, A. Neubauer, R. Georgii, P. Böni, *Science* **2009**, 323, 915.
[42] M. Grelier, F. Godel, A. Vecchiola, S. Collin, K. Bouzehouane, A. Fert, V. Cros, N. Reyren, *Nature Communications* **2022**, 13, 6843.
[43] N. Kent, N. Reynolds, D. Raftrey, I. T. G. Campbell, S. Virasawmy, S. Dhuey, R. V. Chopdekar, A. Hierro-Rodriguez, A. Sorrentino, E. Pereiro, S. Ferrer, F. Hellman, P. Sutcliffe, P. Fischer, *Nature Communications* **2021**, 12, 1562.
[44] S.-Z. Lin, A. Saxena, C. D. Batista, *Physical Review B* **2015**, 91, 224407.
[45] G. Posnjak, S. Čopar, I. Muševič, *Scientific Reports* **2016**, 6, 26361.
[46] I. Lima Fernandes, S. Blügel, S. Lounis, *Nature Communications* **2022**, 13, 1576.
[47] K.-W. Kim, H.-W. Lee, K.-J. Lee, M. D. Stiles, *Physical Review Letters* **2013**, 111, 216601.
[48] S. Klingler, A. V. Chumak, T. Mewes, B. Khodadadi, C. Mewes, C. Dubs, O. Surzhenko, B. Hillebrands, A. Conca, *Journal of Physics D: Applied Physics* **2015**, 48, 015001.
[49] K. Shahbazi, J.-V. Kim, H. T. Nembach, J. M. Shaw, A. Bischof, M. D. Rossell, V. Jeudy, T. A. Moore, C. H. Marrows, *Physical Review B* **2019**, 99, 094409.
[50] I. A. Yastremsky, O. M. Volkov, M. Kopte, T. Kosub, S. Stienen, K. Lenz, J. Lindner, J. Fassbender, B. A. Ivanov, D. Makarov, *Physical Review Applied* **2019**, 12, 064038.

[51] T. Böttcher, K. Lee, F. Heussner, S. Jaiswal, G. Jakob, M. Kläui, B. Hillebrands, T. Brächer, P. Pirro, *IEEE Transactions on Magnetics* **2021**, 57, 1.
[52] T. Böttcher, T. S. Suraj, X. Chen, B. Sinha, H. R. Tan, H. K. Tan, R. Laskowski, B. Hillebrands, M. Kostylev, K. H. Khoo, A. Soumyanarayanan, P. Pirro, *Physical Review B* **2023**, 107, 094405.
[53] A. K. Chaurasiya, C. Banerjee, S. Pan, S. Sahoo, S. Choudhury, J. Sinha, A. Barman, *Scientific Reports* **2016**, 6, 32592.
[54] J. Torrejon, J. Kim, J. Sinha, S. Mitani, M. Hayashi, M. Yamanouchi, H. Ohno, *Nature Communications* **2014**, 5, 4655.
[55] D.-S. Han, N.-H. Kim, J.-S. Kim, Y. Yin, J.-W. Koo, J. Cho, S. Lee, M. Kläui, H. J. M. Swagten, B. Koopmans, C.-Y. You, *Nano Letters* **2016**, 16, 4438.
[56] M. Kuepferling, A. Casiraghi, G. Soares, G. Durin, F. Garcia-Sanchez, L. Chen, C. H. Back, C. H. Marrows, S. Tacchi, G. Carlotti, *Reviews of Modern Physics* **2023**, 95, 015003.
[57] G. Gubbiotti, *Three-Dimensional Magnonics Layered, Micro- and Nanostructures* **2019**, Chapter 5

[58] H. Jia, B. Zimmermann, G. Michalicek, G. Bihlmayer, S. Blügel, *Physical Review Materials* **2020**, 4, 024405.
[59] F. Ajejas, Y. Sassi, W. Legrand, S. Collin, J. Peña Garcia, A. Thiaville, S. Pizzini, N. Reyren, V. Cros, A. Fert, *Physical Review Materials* **2022**, 6, L071401.
[60] R. Bansal, A. Kumar, N. Chowdhury, N. Sisodia, A. Barvat, A. Dogra, P. Pal, P. K. Muduli, *Journal of Magnetism and Magnetic Materials* **2019**, 476, 337.
[61] Y. Shi, P. Yang, S. Jiang, Z. Zhang, Y. Huan, C. Xie, M. Hong, J. Shi, Y. Zhang, *Nanotechnology* **2019**, 30, 034002.
[62] A. Berkdemir, H. R. Gutiérrez, A. R. Botello-Méndez, N. Perea-López, A. L. Elías, C.-I. Chia, B. Wang, V. H. Crespi, F. López-Urías, J.-C. Charlier, H. Terrones, M. Terrones, *Scientific Reports* **2013**, 3, 1755.
[63] P. Tonndorf, R. Schmidt, P. Böttger, X. Zhang, J. Börner, A. Liebig, M. Albrecht, C. Kloc, O. Gordan, D. R. T. Zahn, S. Michaelis de Vasconcellos, R. Bratschitsch, *Opt. Express* **2013**, 21, 4908.
[64] M. Mahjouri-Samani, L. Liang, A. Oyedele, Y.-S. Kim, M. Tian, N. Cross, K. Wang, M.-W. Lin, A. Boulesbaa, C. M. Rouleau, A. A. Puretzky, K. Xiao, M. Yoon, G. Eres, G. Duscher, B. G. Sumpter, D. B. Geohegan, *Nano Letters* **2016**, 16, 5213.
[65] C. Kittel, *Physical Review* **1948**, 73, 155.
[66] W. Zhang, W. Han, X. Jiang, S.-H. Yang, S. S. P. Parkin, *Nature Physics* **2015**, 11, 496.
[67] B. A. Kalinikos, A. N. J. J. o. P. C. S. S. P. Slavin, **1986**, 19, 7013.
[68] K. Ahmadi, L. Jamilpanah, S. A. Seyed Ebrahimi, A. Olyaee, M. M. Tehranchi, S. M. Mohseni, *Journal of Physics D: Applied Physics* **2020**, 53, 465001.
[69] A. A. Stashkevich, M. Belmeguenai, Y. Roussigné, S. M. Cherif, M. Kostylev, M. Gabor, D. Lacour, C. Tiusan, M. Hehn, *Physical Review B* **2015**, 91, 214409.
[70] A. R. Fert, *Materials Science Forum* **1990**, 59-60, 439.
[71] Q.-F. Yao, J. Cai, W.-Y. Tong, S.-J. Gong, J.-Q. Wang, X. Wan, C.-G. Duan, J. H. Chu, *Physical Review B* **2017**, 95, 165401.
[72] J. Klinovaja, D. Loss, *Physical Review B* **2013**, 88, 075404.
[73] Q. Shao, G. Yu, Y.-W. Lan, Y. Shi, M.-Y. Li, C. Zheng, X. Zhu, L.-J. Li, P. K. Amiri, K. L. Wang, *Nano Letters* **2016**, 16, 7514.
[74] Y. Zhao, X. Fang, Z. Wang, M. Cheng, Y. Tan, D. Wei, C. Jiang, J. Yao, *Chinese Physics B* **2023**, 32, 056701.
[75] D. MacNeill, G. M. Stiehl, M. H. D. Guimaraes, R. A. Buhrman, J. Park, D. C. Ralph, *Nature Physics* **2017**, 13, 300.

Chapter 10

10. Summary and Future Perspective

The future outlook of spintronics and magnonics, as explored in this thesis, highlights several promising pathways for advanced material science and next-generation device development. The investigations into spin dynamics, hybrid quasi-particle interactions, and spin-orbit torque (SOT) modulation offer significant contributions to the understanding of ultrafast spin behavior and pave the way for innovative applications. One notable direction is the design of reconfigurable magnonic devices, such as 1D magnonic crystals, where the proposed omni-directional emitter and SW waveguide demonstrate how spin-wave propagation can be efficiently controlled. These concepts are vital for future information processing systems and energy-efficient communication devices.

The use of low-damping materials like YIG and Heusler alloys is expected to enhance the performance of magnonic systems, while the development of hybrid quantum devices based on ferromagnetic nanostructures introduces the possibility of coherent and long-distance information transfer. SOT-driven magnonics, with potential applications in spin torque nano oscillators, represent another exciting field for developing low-damping, high-efficiency spintronic components.

An important aspect of future research is the exploration of interfacial Dzyaloshinskii-Moriya interaction (iDMI), especially in heterostructures involving heavy metals (Pt, Pd, W) and ferromagnets (CoFeB, NiFe), as well as 2D materials like MoS2 or graphene. These interfaces can stabilize exotic spin textures like skyrmions, which are of great interest for their non-reciprocal spin-wave properties and potential use in high-density storage devices.

The study of ultrafast magnetization dynamics in confined ferromagnetic films and nanostructures is particularly crucial for advancing the understanding of sub-picosecond spin processes. The exploration of novel mechanisms like optical inter-site spin-transfer (OISTR) and spin-transfer between domains will be key to unlocking ultrafast demagnetization behavior. Further research into spin-wave propagation through magnetic monopoles in artificial spin ice (ASI) structures and defects in magnonic crystals will likely lead to the discovery of new magnetic phenomena and practical applications in reconfigurable spin-wave-based devices.

Moreover, hybrid systems combining magnons with other quasi-particles like photons, phonons, and superconducting qubits open a new dimension in nanotechnology, where on-chip quantum devices could operate at gigahertz frequencies. These interactions could be tuned by adjusting external factors such as magnetic field orientation, nanomagnet geometry, and excitation power, offering sophisticated control in future research.

In conclusion, this thesis not only deepens our fundamental understanding of spintronic and magnonic phenomena but also provides a clear direction for future advancements. The potential to manipulate and engineer spin textures, along with the study of multi-quasi-particle systems, sets the stage for transformative technologies in quantum computing, information storage, and energy-efficient communications. The proposed device structures and theoretical models are likely to inspire future research that will further push the boundaries of condensed matter physics and nanotechnology.